Coordinatore
Fernando Fraternali

Tutor
Ciro Caliendo

Isidoro Russo

Methodological approach for the analysis of safety in road tunnels with reference to the thermal effects on the structure

Approccio metodologico per l'analisi della sicurezza nelle gallerie stradali con riferimento agli effetti termici sulla struttura

XXXIV Cycle (2019 – 2021)

UNIVERSITÀ
DEGLI STUDI
DI SALERNO

Dipartimento di
Ingegneria Civile

Rischio e Sostenibilità
nei Sistemi dell'Ingegneria Civile,
Edile ed Ambientale

Methodological approach for the analysis of safety in road tunnels with reference to the thermal effects on the structure

Isidoro Russo

Ministero dell'Istruzione,
dell'Università e della Ricerca

UNIVERSITY OF SALERNO

DEPARTMENT OF CIVIL ENGINEERING

PhD course in
Risk and Sustainability
in Civil, Architectural and Environmental Systems

Curriculum - Advanced technologies, infrastructure and land protection for sustainable development

XXXIV Cycle (2020 - 2021)

PhD thesis in

Methodological approach for the analysis of safety in road tunnels with reference to the thermal effects on the structure

Isidoro Russo

Tutor
Prof. Eng. Ciro Caliendo

PhD Course Coordinator
Prof. Eng. Fernando Fraternali

Ministero dell'Istruzione,
dell'Università e della Ricerca

UNIVERSITA' DEGLI STUDI DI SALERNO

DIPARTIMENTO DI INGEGNERIA CIVILE

Corso di dottorato di ricerca in
Rischio e sostenibilità
nei sistemi dell'ingegneria civile, edile e ambientale

Curriculum - Tecnologie avanzate, infrastrutture e protezione del territorio per lo sviluppo sostenibile

XXXIV Ciclo (a.a. 2020 - 2021)

Tesi di dottorato in

Approccio metodologico per l'analisi della sicurezza nelle gallerie stradali con riferimento agli effetti termici sulla struttura

Isidoro Russo

Tutor
Prof. Ing. Ciro Caliendo

Coordinatore del dottorato
Prof. Ing. Fernando Fraternali

Publications list

Caliendo, C., De Guglielmo, M.L., Russo, I., 2019. Analysis of crash frequency in motorway tunnels based on a correlated random-parameters approach. Tunnelling and Underground Space Technology 85, 243-251, doi: https://doi.org/10.1016/j.tust.2018.12.012.

Astarita, V., Caliendo, C., Giofrè, V.P., Russo, I., 2020. Surrogate safety measures from traffic simulation: Validation of safety indicators with intersection traffic crash data. Sustainability 12, 4974, doi:10.3390/su12176974.

Caliendo, C., Guida, M., Postiglione, F., Russo, I., 2021. A Bayesian bivariate hierarchical model with correlated parameters for the analysis of road crashes in Italian tunnels. Statistical Methods and Applications, doi:10.1007/s10260-021-00567-5.

Caliendo, C., Genovese, G., Russo, I., 2021. Risk analysis of road tunnels: A computational fluid dynamic model for assessing the effects of natural ventilation. Applied Sciences 11, 32, doi:10.3390/app11010032.

Caliendo, C., Russo, I., Genovese, G., 2021. Risk analysis of one-way road tunnel tube used for bi-directional traffic under fire scenarios. Applied Sciences, 11, 3198, doi:10.3390/app11073198.

Caliendo, C., Genovese, G., Russo, I., 2021. A Numerical Study for Assessing the Risk Reduction Using an Emergency Vehicle Equipped with a Micronized Water System for Contrasting the Fire Growth Phase in Road Tunnels. Applied Sciences 11, 5248, https://doi.org/10.3390/app11115248.

Caliendo, C.; Russo, I. I maggiori pericoli per gli utenti in caso di incendio in galleria. Strade & Autostrade, issue n° 145 January/February 2021: lockdown e Recovery Plan, pandemia e risorse da gestire con grande attenzione.

Contents

Chapter 1 Introduction 1

Chapter 3 Spalling: 3D FDS modeling 59

Chapter 4 Spalling prediction models 119

List of figures

List of tables

Abstract

The major risks for users in the event of a tunnel fire derive from the high temperatures generated by the burning vehicle, the smoke that progressively fills the tunnel reducing the visibility for people evacuation, the production of carbon monoxide and toxic substances that, associated with the consumption of oxygen, can cause intoxication and, consequently, loss of consciousness and anoxia. However, in addition to the consequences on human health, the negative effects on the tunnel structure due to high temperatures should also be considered, as well as the direct costs of repairing the damaged structures and the indirect costs associated with the temporary closure of the tunnel and the use of alternative routes.

Directive 2004/54/EC, adopted in Italy in 2006, requires, in addition to a quantitative risk analysis aimed at identifying the risk level for users in the event of a tunnel fire, the assessment of the fire resistance of the tunnel structure in cases where its local collapse might cause catastrophic consequences, such as, for example, to important adjacent structures or immersed tunnels.

Most existing tunnels are made of unreinforced or reinforced concrete, while new tunnels are more especially of reinforced concrete. When concrete structures are subjected to high and rapidly rising temperatures, more or less violent detachments of material can occur. This phenomenon, known as *spalling*, can lead, in the case of reinforced concrete, to the breaking-off of the concrete cover, so that a more or less extensive area of concrete might remain with the steel rebars directly exposed to high temperatures. In these circumstances, since steel has a lower fire resistance than concrete, the steel reinforcements might no longer be able to fulfill their function of absorbing tensile stresses, thus contributing to a structural collapse, even if localized. This, in addition to reducing the safety level for tunnel users not yet evacuated and obstructing rescue teams, might cause the collapse of buildings located above the tunnel vault or water infiltrations.

In the light of the above considerations, in order to reach the optimal fire resistance design of tunnels, it is very important to be able to quantitatively predict spalling. In this respect, the main scope of the present thesis was to develop predictive models, namely an analytical method, capable of evaluating fire-induced damage as a function of both the tunnel geometry and the fire scenario. For this aim, three-dimensional Computational Fluid Dynamics (CFD) modeling was coupled with the statistical approach. In this work, among the different codes available, the Fire Dynamics Simulator (FDS) was used as a CFD simulation tool, while the LIMDEP statistical package was applied as a statistical simulation tool.

The first step in order to set up the analytical method aimed at predicting spalling was to develop, given the lacuna, a new 3D CFD model able to estimate fire-induced damage. Once this model was validated by comparing its results with those provided by a competitive model present in the international literature, the relevant conclusions were drawn with reference to the case study investigated.

Based on the above-mentioned developed 3D CFD model, the second step to reach the fixed scope was to identify the variables that had the greatest influence on fire-induced damage. For this aim, certain assumptions were made, and several preliminary simulations were carried out. In this respect, the longitudinal ventilation within the tunnel, the heat release rate, the tunnel cross-section area, and the longitudinal slope of the tunnel were found to be the variables with the greatest impact on spalling; as a result, the latter were assumed to be the independent variables of the proposed predictive models. Specifically, these predictive models were univariate Negative Binomial (NB) models with fixed parameters. The dependent variables were the maximum spalling depth, the spalling start time, and the maximum length of the tunnel affected by spalling.

On this basis, certain predictive models were set up. The results showed that the developed analytical method was capable of providing a good to excellent prediction of maximum spalling depth, spalling start time, and maximum length of the tunnel affected by spalling.

Therefore, the author is confident that the proposed predictive models represent an important advancement of knowledge, given the lacuna, in the field of tunnel fire safety engineering. In fact, the results obtainable from these predictive models would be useful not only to the international scientific community but also to both road engineers and Tunnel Management Agencies (TMAs) in order to estimate how fire-induced damage varies with longitudinal ventilation, maximum heat release rate, tunnel cross-section area, and longitudinal slope.

Finally, in order to mitigate fire-induced damage, certain coatings such as cement-based mortars, panels, and an intumescent paint were used. In this respect, the results showed that all investigated coatings were able to prevent spalling, thus reducing the risk of structural collapse. Specifically, based on the criterion of the ratio between thermal performance and application thickness, the best insulation-material used in this study was the intumescent paint.

Chapter 1

Introduction

1.1. Background and state of the art

1.1.1. Overview

Road tunnels, as part of a transport infrastructure, play an essential role in supporting the mobility of goods and people, allowing passage through mountains, urban areas, and under waterways. For providing the social and economic benefits for which a tunnel is designed and built, it should be kept open to traffic as much as possible. However, the functionality of a road tunnel might be compromised by a traffic accident and/or fire occurring within it. Although traffic accidents or fires in tunnels are rarer than on open roads (*Amundsen and Engebretsen, 2009; Lu et al., 2016*), their effects might be more severe in terms of both fatalities and structure damage (*Caliendo and De Guglielmo, 2012*). In this respect, it is also to be said that tunnel fires are less frequent than tunnel traffic accidents, but their consequences can be catastrophic (*Beard and Carvel, 2005*). In fact, in tunnel fires caused by vehicular crashes or vehicle breakdown, more especially those involving flammable cargo, temperatures could rise rapidly due to the enclosed nature of these structures.

Most existing tunnels are made of unreinforced or reinforced concrete, while new tunnels are more especially of reinforced concrete. When concrete structures are subjected to high and rapidly rising temperatures, violent or non-violent breaking-off of material from concrete surfaces may occur. This phenomenon, known as *spalling*, can lead, in the case of reinforced concrete, to the detachment of the concrete cover, so that a more or less extensive area of concrete might remain with the steel rebars directly exposed to high temperatures. In these circumstances, since steel has a lower fire resistance than concrete, the steel reinforcements might no longer be able to fulfill their function of absorbing tensile stresses, thus contributing to a structural collapse, even if localized. It is also to be stressed that, in addition to the high costs of repairing the damaged structures and the indirect costs associated with the temporary closure of the roads containing these tunnels and the use of alternative routes, spalling leads to a reduction in the safety level for both rescue teams and users who are not yet evacuated, as well as the possible collapse of buildings located above the tunnel vault and/or water infiltrations.

In the light of the above considerations, following the severe damages recorded after certain tunnel fires occurring in Europe in the last decades (Mont Blanc tunnel between France and Italy in 1999 with 39 depths, Tauern tunnel in Austria in 1999 with 12 depths, and Saint Gotthard tunnel between Switzerland and

Italy in 2001 with 11 depths), the competent authorities, the scientific community, and the public opinion paid much more attention to the study of both the causes of concrete spalling and the factors influencing it, as well as how this phenomenon can be prevented. In this respect, *Directive 2004/54/EC*, adopted by the *Italian Ministry of Infrastructures and Transports* in 2006, requires the assessment of the fire resistance of the tunnel structure in cases where its local collapse might cause catastrophic consequences, such as, for example, to important adjacent structures or immersed tunnels.

Fig. 1.1, Fig. 1.2, and Fig. 1.3 show the catastrophic tunnel fires that occurred within the Mont Blanc tunnel, Tauern tunnel, and Saint Gotthard tunnel.

Fig. 1.1. Mont Blanc tunnel fire in 1999 with 39 depths.

Fig. 1.2. Tauern tunnel fire in 1999 with 12 depths.

Fig. 1.3. Saint Gotthard tunnel fire in 2001 with 11 depths.

1.1.1.1. Spalling

As mentioned above, spalling is the violent or non-violent detachment of material from concrete surfaces subjected to high and rapidly rising temperatures (*Khoury, 2000*).

Fig. 1.4 shows a concrete element affected by spalling.

Fig. 1.4. Concrete element affected by spalling (*Mastronardi, 2013*).

1.1.1.1.1. Mechanisms of spalling

Three theories have so far been proposed in order to explain the spalling mechanism, namely:

- Pore-pressure spalling;
- Thermal-stress spalling;
- Thermo-chemical spalling.

The *pore-pressure spalling* theory is associated with the thermal-hygral process within heated concrete. In particular, the transport of water vapor, generated during exposure to fire, within the micro-pores of concrete and its accumulation at a certain depth, causes a gradual increase in interstitial pressure. When the tensile stress due to pore pressure exceeds the tensile strength of concrete, spalling occurs (*Ichikawa and England, 2004; Dwaikat and Kodur, 2009; Ozawa and Morimoto, 2014*).

With reference to the *thermal-stress spalling* theory, instead, there are two different points of view. In fact, some researchers believe that spalling is caused by compressive stresses induced by colder concrete impeding the dilatation of heated concrete (*Msaad, 2006*), while others insist that spalling is due to the thermal gradient resulting from thermal stress (*Fu and Li, 2011; Zhao et al., 2014*). It is worth noting that another theory that combines the pore-pressure and thermal-stress spalling mechanisms is also proposed (*Connolly, 1995; Mindeguia et al., 2015*).

The third theory, known as *thermo-chemical spalling*, deems that spalling is due to chemical alteration during a fire of the raw materials of which concrete is made (*Liu et al., 2018*).

1.1.1.1.2. Types of spalling

Spalling can take different forms, namely:

- Aggregate spalling;
- Explosive spalling;
- Surface spalling;
- Corner/sloughing-off spalling.

The aggregate, explosive, and surface spalling usually occur within the first 20-30 min from the fire start and are more especially affected by the heating rate, while the corner/sloughing-off spalling takes place after 30-60 min from the fire start and depends mainly on the maximum temperature (*Khoury, 2000*). In this respect, the latter is non-violent, while both the explosive and surface spalling are violent. It is also to be stressed that the surface spalling is a sub-set of the explosive spalling, which is the most severe form of spalling. Specifically, the explosive spalling is characterized by a burst-out of concrete pieces accompanied by a sudden release of energy and a loud noise.

1.1.1.1.3. Factors influencing spalling

A comprehensive account of the factors that affect spalling is outside the scope of this thesis; however, the main factors are (*Khoury, 2000; Hertz, 2003; Clement, 2010; Maraveas and Vrakas, 2014; Hawileh and Kodur, 2018*):

- Heating rate;
- Heating profile;
- Fire duration;
- Concrete permeability;
- Moisture content of concrete;
- Aggregate size;
- Aggregate type;
- Reinforcement type.

1.1.1.1.4. Concretes susceptible to spalling

Spalling can affect all types of concrete when exposed to high and rapidly rising temperatures. However, it is believed that High and Ultra-High Strength Concretes (HSCs and UHSCs, respectively), more especially those with a moisture content greater than 2-3% by weight of concrete (*Khoury, 2000*), are more prone to spalling due to their low permeability compared to Normal Strength Concretes (NSCs). In fact, the low permeability leads to a very high-water vapor pressure within the concrete pores, and since it cannot leakage owing to the high density of HSC and UHSC, the pore-pressure spalling mechanism might occur.

1.1.1.1.5. Critical temperature

Spalling can occur at different temperatures. The temperature above which spalling might take place is called *critical*.

Although it is difficult to clearly define the critical temperature, some authors believe that fire-induced damage might occur in the temperature range of 250-450 °C (*Khoury, 2000; Hertz, 2003*). Moreover, *Khoury (2000)* found a pronounced increase in the creep of Portland cement-based concrete at about 600 °C, indicating it as the critical temperature at which the material would not be structurally useful in the hot state. In order to prevent deterioration of concrete properties, the International Tunneling Association (*ITA, 2004*) suggested that the maximum temperature to be applied to concrete is 380 °C. Instead, *Eurocode 2 (2004)* indicated that the load-bearing capacity and elastic modulus of concrete are approximately halved for temperatures of 500-600 °C. According to *Fletcher et al. (2007)*, a significant reduction in the mechanical properties of concrete takes place when the calcium hydroxide in the cement begins to dehydrate (400 °C). *Clement (2010)* and *Bezgin (2015)* believed that maintaining structural concrete below 300 °C prevents the occurrence of all negative structural problems. While *Sakkas et al. (2012)* deemed that the concrete strength should be considered significantly reduced at temperatures greater than 300 °C. Finally, *Liu et al. (2018)* claimed that the critical temperature associated with the pore-pressure and thermal-stress mechanisms would be between 220-320 °C and 430-660 °C, respectively; while the thermo-chemical spalling generally occurs for temperatures of at least 700 °C.

Therefore, it is to be stressed that there is no shared value of the critical temperature, which can be in the wide temperature range of 250-700 °C. On this basis, it is evident that the influence of the critical temperature on fire-induced damage needs to be better investigated, which is one of the intents of this thesis.

In addition to concrete spalling, damage to steel rebars due to high temperatures should also be considered. In this respect, *Dolzhenkov (1971)* stated that low-carbon steels show both an increase in strength and a significant decrease in ductility in the temperature range of 250-300 °C (known as the *blue brittleness effect*). According to *ITA (2004)*, *Clement (2010)*, and *Bezgin (2015)*, the maximum temperature to be applied to steel is 250 °C; while *Eurocode 2 (2004)* showed that both the strength and elastic modulus of steel reinforcement are roughly halved to about 500-600 °C. *Topçu and Karakurt (2008)* and *Felicetti et al. (2009)* found that steel rebars lose a substantial part of their mechanical strength when heated to temperatures between 550 °C and 600 °C.

1.1.1.2. Fire curves

Numerous international studies have been carried out in recent years in order to identify the different types of fire that could occur in tunnels. These studies took place both in laboratories and in real disused tunnels. The data obtained from these tests were used to define a series of time-temperature curves.

Fig. 1.5 shows the comparison between certain standardized time-temperature curves used for load-bearing design in building and underground constructions.

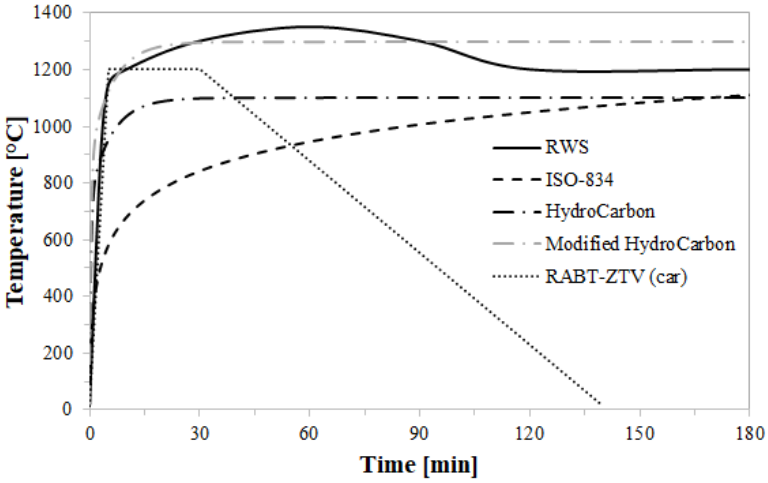

Fig. 1.5. Comparison between standardized time-temperature curves: ISO-834, HydroCarbon (HC), modified HC (HC_{mod}), Rijkswaterstaat (RWS), and RABT/ZTV.

The ISO-834 cellulosic curve has been applied in many countries also for tunnels, even though it is not representative of all types of materials such as chemicals, petrol, etc. In order to overcome this limit of the ISO-834 curve, the HydroCarbon (HC) curve was developed. Specifically, the HC curve, which is the one proposed by *Eurocode 1 (2002)*, is characterized by the fact of reaching the peak temperature of 1100 °C much faster (i.e., in a few minutes) than the ISO-834 curve. However, the HC curve is only suitable for describing small petroleum fires. As a result, some countries have proposed other time-temperature curves in order to simulate more severe hydrocarbon fires in tunnels. Examples of such curves include the Rijkswaterstaat Tunnel Curve (RWS Curve) in the Netherlands (peak temperature of 1350 °C), the modified HC (HC_{mod}) curve in France (peak temperature of 1300 °C), and RABT-ZTV (car) Tunnel Curve in Germany (peak temperature of 1200 °C).

On this basis, the RWS and HC_{mod} curves are representative of the most severe fires that can occur in tunnels. In this regard, since *PIARC (2007)* believes that the RWS and HC_{mod} curves correspond to very similar levels of fire resistance, it recommends the use of one of these curves.

1.1.1.3. Methods for analysis

In order to achieve the optimal fire resistance design of tunnels, it is very important to be able to quantitatively predict spalling. In this regard, different approaches can be adopted:

- Large-scale experiments, which are time-consuming and costly to perform; however, they provide the most useful data (Fig. 1.6);
- Reduced-scale experiments that are often not able to reproduce the exact features of large-scale fire tests such as external loads, materials, and structural shape (Fig. 1.7);
- Computer simulations.

Fig. 1.6. Large-scale experiment.

Fig. 1.7. Reduced-scale experiment.

1.1.1.3.1. Computer simulations

Nowadays, computer simulations are more and more used for their cost-effectiveness compared to other approaches, as well as for their ability to reproduce reality (e.g., tunnel geometry, traffic characteristics, and fire location) with more details than reduced-scale experiments. In this respect, Computational Fluid Dynamics (CFD) codes are among the most suitable and applied tools for performing numerical analyses in the field of fire safety engineering.

The effects that a fire might cause on structures are generally evaluated using either 1D and 2D models based on the Finite Element Method (FEM) technique (some references are reported in Section 1.1.2) or an approach that combines CFD and FEM methodologies (*Welch et al., 2009; Kim et al., 2013; Malendowski and Glema, 2017; Prieler et al., 2020*). In this respect, Fig. 1.8 shows the methodology usually used for the coupled CFD and FEM approach (*Welch et al., 2009*). From Fig. 1.8 one can see that the fire development (i.e., the time history of temperature, species concentrations, and heat fluxes) is reproduced through CFD codes. Subsequently, the data provided by the CFD tool are used as boundary conditions in the FEM code, where both the thermal (i.e., the temperature within solids and variable material data) and mechanical (i.e., deformation and component failure) responses of the structure are evaluated. This means that while CFD codes are preferred for solving fluid-flow (gas phase) problems, FEM tools are traditionally used for structural (solid phase) problems.

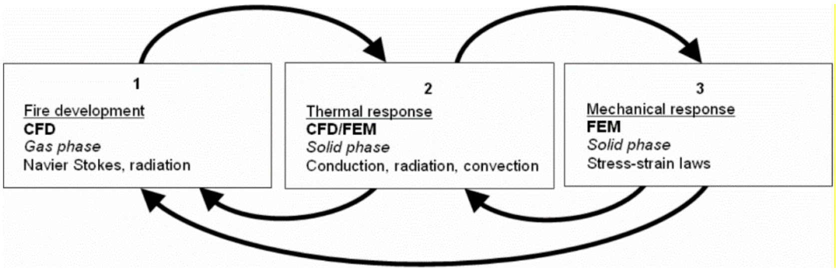

Fig. 1.8. Methodology of the coupled CFD and FEM approach (*Welch et al., 2009*).

As mentioned above, the coupled CFD-FEM approach requires that data obtained from CFD codes be transferred to FEM tools. However, this data transfer is a complex process not without error (*Welch et al., 2009*). In this respect, in order to avoid data transfer issues, FEM tools are often applied alone, namely without the prior use of CFD codes to simulate fire development. This can be done when fire-induced damage is evaluated against standard fire scenarios (e.g., RABT and RWS fire curves), for which the temperature-time curve is known. However, since fire curves are not able to describe all possible fire scenarios that can occur in road tunnels, the use of FEM codes applied to fire curves appears to be only a partial solution to the cited problem related to data transfer, which might be completely solved by attempting to use CFD methodology, better if combined with 3D modeling, not only to reproduce the fire development but also to evaluate the subsequent spalling damage. On this basis, another scope of the present thesis is to develop a 3D CFD model capable of simulating spalling due to a fire occurring in a road tunnel. For this aim, Fire Dynamics Simulator (FDS) version 6.7.3 was used as a CFD simulation tool in this work.

Fig. 1.9 shows an example of a model developed using the FDS code.

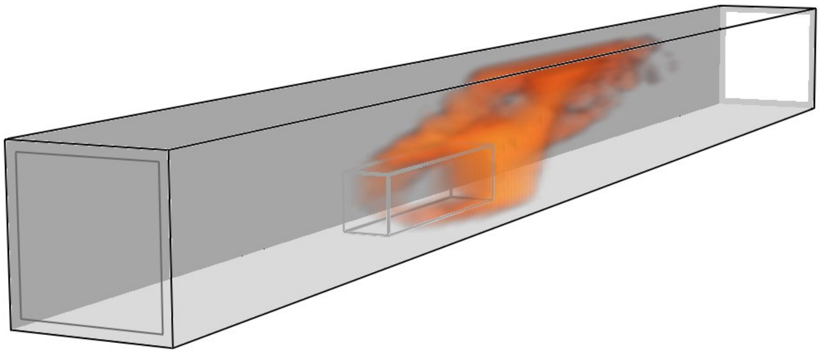

Fig. 1.9. Example of a model developed using the FDS code.

1.1.1.4. Fire protection systems

Spalling might be minimized or eliminated using active or passive fire protection systems. The former include:

- Fire alarm systems;
- Fire detection systems;
- Automatic fire suppression systems such as sprinkler, gaseous clean agent, and foam suppression system;
- Portable fire extinguishers;
- Smoke and fumes control systems.

Instead, Passive Fire Protection (PFP) systems are generally divided into two categories:

- Coatings (e.g., panels, cement-based mortars, and intumescent paints);
- *Concrete design* (e.g., fiber reinforced concrete).

Coatings are commonly applied in both new and existing tunnels, while *concrete design* is usually used for new structures.

Nowadays, among the different types of coatings available on the market, intumescent paints are more and more used. In this respect, it is to be said that intumescent materials are typically applied to protect steel structures from fire; however, in the last years, they have also been increasingly used for concrete structures. In contrast to other types of coatings, intumescent paints can be applied in very thin films (i.e., on the order of a few millimeters), which, when heated, can expand up to one hundred times their initial thickness, forming a carbonaceous char layer that protects construction materials from high temperatures. In general, coatings should guarantee compliance with two conditions (*ITA, 2004*):

- The temperature at the interface between concrete and coating ≤ 380 °C;
- The temperature of the steel reinforcement ≤ 250 °C.

With reference to *concrete design*, instead, in order to mitigate fire-induced damage in HSCs, some researchers have suggested adding 1-3 kg of polypropylene fibers to the concrete mix (*Ali et al., 2004; Clement, 2010*). In fact, polypropylene fibers, melting at about 160 °C, produce micro and macro channels within the concrete volume (*Kalifa et al., 2001*), which facilitate the dispersion of high vapor pressure by preventing the pore-pressure spalling mechanism. In this respect, another theory states that micro-cracking around polypropylene fibers contributes to vapor reduction (*Clement, 2010*). Moreover, it is also to be said that the spalling resistance of concrete might be increased by improving its tensile strength by adding steel fibers to the concrete mix (*Kodur, 1999*). On this basis, the use of both polypropylene and steel fibers in the concrete mix has also been recommended in order to mitigate spalling (*Kodur, 2000; Ali and Nadjai, 2008*). However, it is to be stressed that although fibers are an effective anti-spalling solution, they do not protect structural concrete from other harmful effects due to high temperatures (*Clement, 2010*).

In the light of the above considerations, the present thesis has focused on passive fire protection systems, of which coatings are so far the most widely applied for fire protection of tunnels worldwide. The fire resistance benefits due to the use of coatings are usually assessed through experimental tests. Therefore, another intent of this paper is to exploit the potential of 3D CFD modeling for predicting and analyzing the thermal performance of coatings via computer, as well as for comparing the results found for each coating using the criterion of the ratio between thermal performance and application thickness.

1.1.2. Literature review

Numerous researchers have focused on studying fire-induced damage to concrete structures, but only a few of them have actually attempted to take into account the structural loss caused by spalling; and among these authors, some have only considered changes in concrete properties with temperature (*Caner et al., 2005; Kodur and Dwaikat, 2008*). In addition, it is to be said that spalling prediction based on a heat transfer analysis leads to an underestimation of fire-induced damage because this analysis does not take into consideration structural loss (*Boström and Larsen, 2006*). In other terms, a conventional heat transfer analysis is only appropriate when spalling does not occur.

Although *Khoury et al. (2002)* were unable to simulate structural loss, they used a damage index between 0 and 1 in order to estimate probable spalling. The main limitation of this study, which was also recognized by the authors themselves, is that a spalling criterion was not taken into account in the numerical model. In this work, however, the principles that form the basis for numerical analysis of the thermal, hydraulic, and mechanical behavior of NSC, HSC, and UHSC structures subjected to heating were presented. Finally, they cited several theories proposed for simulating spalling, even though these have not yet been fully verified.

Savov et al. (2005) used layered finite beam elements for discretizing the tunnel lining; in this way, spalling was taken into account by deactivating layers based on a predetermined spalling scenario. In this respect, the authors defined four different spalling scenarios, each of which was characterized by a fixed final spalling depth of 0, 10 cm, 20 cm, or 30 cm. Specifically, spalling was assumed to start after 5 min and end after 30 min of fire exposure, considering a linear increase in spalling depth during this period. The authors also took into account the variations of concrete properties with temperature. However, the thermal load in the lining was determined without considering the coupling of heat and mass transfer.

Considering different spalling scenarios characterized by a fixed final spalling depth of 0, 10 cm, 20 cm, or 30 cm, *Zeiml et al. (2008)* proposed a fully coupled thermo-hydro-chemical model for investigating the structural performance of a tunnel cross-section subjected to fire. In their 1D finite element model, the authors took into account the changes in concrete properties with temperature.

Choi et al. (2013) proposed a 2D model capable of simulating fire-induced damage by eliminating the elements that exceed a pre-specified critical temperature (600 °C) in a finite element analysis, in which both heat transfer coefficients and thermal properties of concrete were considered to be time-dependent. In particular, the temperature distribution and structural loss of the concrete lining over time were evaluated against the RABT and RWS fire scenarios. In this respect, for example, considering an unreinforced concrete and a critical temperature of 600 °C, the authors found that spalling affected the concrete for a depth of about 10 cm under a RABT fire scenario. In general, they found that the results obtained from the numerical simulations were close to those provided by the fire tests.

Zhang et al. (2014) developed a coupled Thermo-Hydro-Chemo-poro-Mechanical (THCM) model for evaluating the risk of concrete spalling due to a fire. In particular, the authors assessed the effects of the intrinsic permeability, porosity, saturation, and strength of concrete on the spalling risk.

With reference to a twin-tube subsea immersed tunnel, *Guo et al. (2016)* proposed a 2D thermal-mechanical coupled finite element model able to assess the thermal stress damage due to a fire characterized by a peak temperature of 1200 °C. In particular, the thermal stress damage of reinforced concrete, whose thermal and mechanical properties were assumed to vary over time, was evaluated based on a residual stress ratio suggested by the authors themselves. In this respect, they found that the maximum spalling depth after about 108 min of fire exposure was 16 cm.

Based on a well-established coupled thermo-hydro-chemo-mechanical (THCM) model, *Zhang et al. (2017)* proposed a method for estimating the spalling risk in a tunnel subjected to RABT fire as a function of both the concrete type and the moisture content. Specifically, the authors used the so-called ‘‘required initial tensile strength” (i.e., the minimum tensile strength under which spalling would occur) for quantifying the spalling risk level (i.e., low, moderate, high, or very high) of concrete.

Qiao et al. (2019) proposed a theoretical method for studying the thermo-mechanical behaviors of tunnel lining exposed to a long-lasting fire. In this respect, a 2D unsteady-state thermo-mechanical model was used for analyzing the time-dependent stresses and temperature distributions in the concrete lining during a modified RABT fire (i.e., the cooling phase was replaced by a constant temperature phase of 1200 °C). The authors provided an abacus through which, as a function of the time of exposure to fire and the ratio between the damage depth and the concrete element thickness, it is possible to estimate spalling damage according to both a temperature-based criterion and a residual stress-based criterion. In this respect, for example, considering a 0.5 m thick concrete element and the temperature-based criterion (i.e., spalling occurs at 600 °C), they found a spalling depth of about 10 cm after 120 min from the fire start. It is also to be said that the proposed theoretical method considered the variations of concrete properties with temperature.

Summing up, the aforementioned chronological literature review showed that many studies have proposed 1D and 2D models using the FEM technique for estimating spalling consequent to the application of standard tunnel fire scenarios (e.g., RABT and RWS fire curves). At the same time, the above-cited papers confirmed that CFD methodology, as well as 3D modeling, has hitherto been very little used for investigating fire-induced damage in tunnels. First of all, however, it is more especially evident that there are no predictive models, namely analytical methods, able to estimate spalling as a function of both the tunnel geometry and the fire scenario.

Given this lacuna and the mentioned potential of CFD codes, in the present thesis, first of all, a new 3D CFD model was developed in order to assess fire-induced damage in a road tunnel. Subsequently, on the basis of this model, an analytical method capable of predicting spalling as a function of both the tunnel geometry and the fire scenario was developed. These represent the main scopes of the present study.

1.2. Aim of the work

In the light of the above background and state of the art, there are at least four main reasons for justifying the present thesis.

The first is motivated by the need to develop a new 3D CFD model able to reproduce the development of a tunnel fire and assess the consequent spalling.

The second is to better investigate the influence of the critical temperature (i.e., the temperature at which spalling might occur) on the severity of fire-induced damage.

The third, which is the main scope of this thesis, is to develop, based on the above-mentioned 3D CFD model, certain predictive models, namely an analytical method, capable of estimating spalling as a function of both the geometric characteristics of the tunnel and the fire scenario. The results obtainable from the proposed predictive models would be useful to both road engineers and Tunnel Management Agencies (TMAs) to estimate how fire-induced damage varies with, for example, longitudinal ventilation, maximum Heat Release Rate (HRR_{max}), tunnel cross-section area, and longitudinal slope.

The fourth is to use 3D CFD modeling for examining and comparing the thermo-insulation performance of certain coatings applied in order to prevent spalling damage.

1.3. Outline of the thesis

The present thesis consists of seven chapters.

Chapter 1 contains an overview of the issues caused by spalling, as well as a description of the factors that most influence the occurrence of this phenomenon and how it can be prevented. A more detailed section includes the state of the art, on the basis of which the scopes of the present research are highlighted and discussed.

Chapter 2 provides an overview of Computational Fluid Dynamics (CFD) methodology applied to fire safety issues in enclosed spaces such as tunnels. A more detailed section describes the Fire Dynamics Simulator (FDS) software, which is the CFD code used in this thesis. Some examples of the preliminary simulations carried out in order to validate the FDS tool are also discussed. Sensitivity analyses against experimental data found in the literature were useful to gain adequate confidence with the FDS code, as well as to understand the capabilities and limitations of the model.

Chapter 3 contains a description of both the tunnel and the fire scenario investigated. The 3D CFD model developed in order to assess fire-induced damage in a road tunnel is presented and the results obtained from it are validated and discussed. Then the relevant conclusions are drawn with reference to the case study analyzed.

In **Chapter 4**, on the basis of the proposed 3D CFD model, certain predictive models, namely an analytical method, capable of estimating fire-induced damage as a function of both the tunnel geometry (i.e., width, height, and longitudinal slope) and the fire scenario (i.e., HRR and longitudinal ventilation) are presented. The results obtained from the developed analytical method are discussed, and the relevant conclusions are drawn with reference to the practical use of these predictive models by both road engineers and Tunnel Management Agencies (TMAs).

Chapter 5 describes the coatings used in order to mitigate fire-induced damage. The potential of each of these coatings to prevent spalling is discussed. Then the relevant conclusions are drawn by comparing the results found for the different coatings based on the criterion of the ratio between thermal performance and application thickness.

Chapter 6 brings together the results found in the previous Chapters in order to draw conclusions and addresses for future research.

Chapter 7 includes Appendix A containing some results found in Chapter 4.

1.4. References

[1] Ali, F., Nadjai, A., 2008. Fire Resistance of Concrete Columns Containing Polypropylene and Steel Fibers. ACI Special Publication 255, 199-216.

[2] Ali, F., Nadjai, A., Silcock, G., Abu-Tair, A., 2004. Outcomes of a major research on fire resistance of concrete columns. Fire Safety Journal 39, 433-445.

[3] Amundsen, F.H., Engebretsen, A., 2009. Studies on Norwegian Road Tunnels II. An Analysis on Traffic Accidents in Road Tunnels 2001–2006; Raport no: TS4-2009; Statens Vegvesen, Vegdirektoratet, Roads and Traffic Department, Traffic Safety Section, Oslo, Norway, 2009.

[4] Beard, A., Carvel, R., 2005. The Handbook of Tunnel Fire Safety; Thomas Telford Ltd.: London, UK.

[5] Bezgin, N.Ö., 2015. An experimental evaluation to determine the required thickness of passive fire protection layer for high strength concrete tunnel segments. Construction and Building Materials 95, 279-286.

[6] Boström, L., Larsen, C.K., 2006. Concrete for tunnel linings exposed to severe fire exposure. Fire Technology 42, 351-362.

[7] Caliendo, C., De Guglielmo, M.L., 2012. Accident rates in road tunnels and social costs evaluation. Procedia - Social and Behavioral Sciences 53, 166–177.

[8] Caner, A., Zlatanic, S., Munfah, N., 2005. Structural fire performance of concrete and shotcrete tunnel liners. Journal of Structural Engineering 131 (12), 1920-1925.

[9] Choi, S.W., Lee, J., Chang, S.H., 2013. A holistic numerical approach to simulating the thermal and mechanical behavior of a tunnel lining subject to fire. Tunnelling and Underground Space Technology 35, 122-134.

[10] Clement, F., 2010. Fire protection options for concrete tunnel linings. Fourth International Symposium on Tunnel Safety and Security, Frankfurt am Main, Germany.

[11] Connolly, R.J., 1995. The spalling of concrete in fires. PhD Thesis. Aston University.

[12] Dolzhenkov, E.I., 1971. The nature of the blue brittleness of steel. Metal Science and Heat Treatment 13 (3), 220-224.

[13] Dwaikat, M.B., Kodur, V.K.R., 2009. Hydrothermal model for predicting fire-induced spalling in concrete structural systems. Fire Safety Journal 44 (3), 425-434.

[14] Eurocode 1, 2002. Actions on structures, Part 1-1: General Actions - Densities, self-weight, imposed loads for buildings. Commission of European Communities, Brussels.

[15] Eurocode 2, 2004. Design of Concrete Structures, Part 1-2: General Rules - Structural Fire Design. Commission of European Communities, Brussels.

[16] European Parliament and Council. Directive 2004/54/EC. In Official Journal of the European Union. L.167; European Parliament and Council: Bruxelles, Belgium, 30 April 2004.

[17] Felicetti, R., Gambarova, P.G., Meda, A., 2009. Residual behaviour of steel rebars and R/C sections after a fire. Construction and Building Materials 23, 3546-3555.

[18] Fletcher, I., Welch, S., Torero, J., Carvel, R., Usmani, A., 2007. Behaviour of concrete structures in fires. Journal of Thermal Science 11, 37-52.

[19] Fu, Y., Li, L., 2011. Study on mechanism of thermal spalling in concrete exposed to elevated temperatures. Materials and Structures 44 (1), 361-376.

[20] Guo, J., Jiang, S.P., Zhang, Z.Y., 2016. Fire thermal stress and its damage to subsea immersed tunnel. Procedia Engineering 166, 296-306.

[21] Hawileh, R.A., Kodur, V.K.R., 2018. Performance of reinforced concrete slabs under hydrocarbon fire exposure. Tunnelling and Underground Space Technology 77, 177-187.

[22] Hertz, K., 2003. Limits of spalling of fire-exposed concrete. Fire Safety Journal 38, 103-116.

[23] Ichikawa, Y., England, G., 2004. Prediction of moisture migration and pore pressure build-up in concrete at high temperatures. Nuclear Engineering and Design 228 (1), 245-259.

[24] ITA-International Tunneling Association, 2004. Guidelines for Structural Fire Resistance for Road Tunnels. Working Group No. 6 Maintenance and Repair.

[25] Italian Ministry of Infrastructures and Transports. Adoption of the Directive 2004/54/EC on the Safety of Tunnels Belonging to the Trans.-European Road Network; G.U., No. 235; Italian Ministry of Infrastructures and Transports: Rome, Italy, 9 October 2006.

[26] Kalifa, P., Chéné, G., Gallé, C., 2001. High-temperature behavior of HPC with polypropylene fibers from spalling to microstructure. Cement and Concrete Research 31, 1487-1499.

[27] Khoury, G.A., 2000. Effect of fire on concrete and concrete structures. Progress in Structural Engineering and Materials 2 (4), 429-447.

[28] Khoury, G.A., Majorana, C.E., Pesavento, F., Schrefler, B.A., 2002. Modeling of heated concrete. Magazine of Concrete Research 54 (2), 77-101.

[29] Kim, S.H., Choi, J.B., Park, J.S., Choi, Y.H., Lee, J.H., 2013. A coupled CFD-FEM analysis on the safety injection piping subjected to thermal stratification. Nuclear Engineering and Technology 45, 237–248.

[30] Kodur, V.K.R., 1999. Fiber reinforced concrete for enhancing structural fire resistance of columns. American Concrete Institute, 215-234, (SP 182-12).

[31] Kodur, V.K.R., Dwaikat, M., 2008. A numerical model for predicting the fire resistance of reinforced concrete beams. Cement and Concrete Composites 30, 431-443.

[32] Liu, J.-C., Tan, K.H., Yao, Y., 2018. A new perspective on nature of fire-induced spalling in concrete. Construction and Building Materials, 184, 581-590.

[33] Lu, J.J., Xing, Y., Wang, C., Cai, X., 2016. Risk factors affecting the severity of traffic accidents at Shanghai river-crossing tunnel. Traffic Injury Prevention 17, 176–180.

[34] Malendowski, M., Glema, A., 2017. Development and Implementation of Coupling Method for CFD-FEM Analyses of Steel Structures in Natural Fire. Procedia Engineering 172, 692–700.

[35] Maraveas, C., Vrakas, A. A., 2014. Design of Concrete Tunnel Linings for Fire Safety. Structural Engineering International, 24 (3), 319-329.

[36] Mastronardi, I., 2013. Il fenomeno dello spalling nel calcestruzzo esposto alle alte temperature. Available online: https://www.inconcreto.net/3000-il-fenomeno-dello-spalling-nel-calcestruzzo-esposto-alle-alte-temperature (accessed on 9 October 2021).

[37] Mindeguia, J.C., Carré, H., Pimienta, P., La Borderie, C., 2015. Experimental discussion on the mechanisms behind the fire spalling of concrete. Fire and Materials 39 (7), 619-635.

[38] Msaad, Y., Bonnet, G., 2006. Analyses of heated concrete spalling due to restrained thermal dilation: application to the ‘‘chunnel” fire. Journal of Engineering Mechanics 132 (10), 1124-1132.

[39] Prieler, R., Gerhardter, H., Landfahrer, M., Gaber, C., Schluckner, C., Eichhorn-Gruber, M., Schwabegger, G., Hochenauer, C., 2020. Development of a numerically efficient approach based on coupled CFD/FEM analysis for virtual fire resistance tests-Part B: Deformation process of a steel structure. Fire and Materials 44, 704-723.

[40] Ozawa, M., Morimoto, H., 2014. Effects of various fibres on high-temperature spalling in high-performance concrete. Construction and Building Materials 71, 83-92.

[41] PIARC, 2007. Systems and Equipment for Fire and Smoke Control in Road Tunnels. PIARC Technical Committee C5 Road Tunnel. <http://www.piarc.org>.

[42] Qiao, R., Shao, Z., Liu, F., Wei, W., 2019. Damage evolution and safety assessment of tunnel lining subjected to long-duration fire. Tunnelling and Underground Space Technology 83, 354-363.

[43] Sakkas, K., Nomikos, P., Sofianos, A., Panias, D., 2012. Inorganic polymeric materials for passive fire protection of underground constructions. Fire and Materials 37, 140-150.

[44] Savov, K., Lacker, R., Mang, H.A., 2005. Stability assessment of shallow tunnels subjected to fire load. Fire Safety Journal 40, 745-763.

[45] Topçu, İ.B., Karakurt, C., 2008. Properties of Reinforced Concrete Steel Rebars Exposed to High Temperatures. Research Letters in Materials Science, 1-4.

[46] Welch, S., Miles, S., Kumar, S., Lemaire, T., Chan, A., 2009. FIRESTRUC - Integrating advanced three-dimensional modelling methodologies for predicting thermo-mechanical behaviour of steel and composite structures subjected to natural fires. Fire Safety Science 9, 1315-1326.

[47] Zeiml, M., Lackner, R., Pesavento, F., Schrefler, B., 2008. Thermo-hydro-chemical couplings considered in safety

assessment of shallow tunnels subjected to fire load. Fire Safety Journal 43, 83-95.

[48] Zhang, Y., Zeiml, M., Maier, M., Yuan, Y., Lackner, R., 2017. Fast assessing spalling risk of tunnel linings under RABT fire: From a coupled thermo-hydro-chemo-mechanical model towards an estimation method. Engineering Structures 142, 1-19.

[49] Zhang, Y., Zeiml, M., Pichler, C., Lackner, R., 2014. Model-based risk assessment of concrete spalling in tunnel linings under fire loading. Engineering Structures 77, 207-215.

[50] Zhao, J., Zheng, J.-J., Peng, G.-F., van Breugel, K., 2014. A meso-level investigation into the explosive spalling mechanism of high-performance concrete under fire exposure. Cement and Concrete Research 65, 64-75.

Chapter 2

CFD modeling

2.1. Introduction

Computational Fluid Dynamics (CFD) is one of the most suitable simulation tools for predicting and analyzing fluid flows via computer. CFD involves a vast range of technologies (e.g., computer science, chemistry, physics, mathematics, engineering), brought together to allow the modeling of fluid flows in certain situations.

The CFD technique took off with the arrival of the digital computer in the 1960s. The first CFD applications were in the field of aerospace; however, as computer performance has increased and understanding of fluid dynamics processes has improved, CFD methods have also established themselves in other contexts, including fire safety engineering.

In the field of fire safety engineering, CFD codes have also been widely applied with respect to road tunnels. In this regard, CFD tools can be used to reproduce the development of fires inside tunnels and assess their consequences on both structures and people within them; or to evaluate the efficiency of the ventilation system (natural or forced) and other safety measures implemented (e.g., fire detection and alarm systems, fire protection systems) as a function of, for example, the fire source (e.g., power, duration, position) and the tunnel geometry (e.g., cross-sectional dimensions, horizontal and vertical alignments).

2.1.1. CFD methodology

The applications of practical interest in the field of fire safety engineering can involve more or less complex geometries and fluid flows problems. In these circumstances, it is not possible to solve analytically the governing equations describing the conservation of mass, momentum, and energy. In fact, the exact equations of fluid flow cannot be solved directly except in highly simplified cases.

CFD codes numerically solve a simplified form of the Navier-Stokes equations, providing approximate solutions. The approximations usually concern the reduction of partial differential equations into finite difference equations, as well as the transfer of heat and momentum close to the domain boundaries. The realism and accuracy of the model predictions depend on the validity of these essential approximations.

The main factors affecting the reliability of the numerical solution method are the boundary and initial conditions, as well as the sub-models used for describing the phenomena of turbulence, combustion, and thermal radiation.

The accuracy of the simulation results depends more especially on the fineness of the cells in which the region of interest is discretized, the efficiency of the numerical algorithms employed to solve the governing equations, and the time step for which these equations are solved.

2.2. The FDS code

Fire Dynamics Simulator (FDS) version 6.7.3 was employed as a simulation tool in this work. It is an open-source CFD model of fire-driven fluid flow (*McGrattan et al., 2019a*). The code can be used for predicting and analyzing the consequences on both structures and people resulting from fires occurring in open or enclosed spaces such as tunnels.

The input data for an FDS application are contained in a text file and, with reference to the simulation of a tunnel fire, concern: tunnel geometry, location and dimensions of the burning vehicle (the thermal power of a fire is expressed in terms of Heat Release Rate (HRR)), ventilation system, safety measures, traffic composition (i.e., location and dimensions of vehicles in the queue), boundary and initial conditions, material properties, physical sub-models, etc.

FDS is capable of providing time-dependent three-dimensional results for each cell in which the model space is discretized. The results (e.g., gas and wall surface temperatures, velocity and direction of airflow, smoke and toxic gases concentration, convective and radiative heat transfer, etc.) are reported in text files and can be displayed with a graphical post-processor known as *Smokeview*. The latter is a tool associated with the FDS code that allows static or dynamic visualization of fluid flow data using 2D or 3D contours; the direction and magnitude of the flow are shown using flow vectors (*Forney, 2019*). FDS and Smokeview were developed by the collaboration between the National Institute of Standards and Technology (NIST) and the VTT Technical Research Centre of Finland.

2.2.1. Physical sub-models

The reliability of the simulation results also depends on the physical sub-models used for describing turbulence, combustion, and thermal radiation phenomena. These sub-models are solved in conjunction with the Navier-Stokes equations for the transport of mass, momentum, and energy.

FDS offers a vast range of sub-models to allow reliable modeling of the physical phenomena occurring during a fire (*McGrattan et al., 2019b*).

2.2.1.1. Turbulence model

Turbulence is the key mechanism responsible for the transport of mass, momentum, and energy in most fluid flows. It governs the mixing process of fuel and oxygen, determining the rate of the combustion reaction. Turbulence consists of rotational eddies that also influence the movement and dilution of smoke by mixing. Turbulent motions include a vast range of time and length scales, making turbulence modeling very challenging. In the case of tunnel fires, these scales depend more especially on the characteristics of the fire and the size of the enclosed space.

Turbulence might be modeled using several methods, but none of them can be considered valid for every fluid dynamic application. The main approaches for turbulence modeling in FDS are Direction Numerical Simulation (DNS), Large Eddy Simulation (LES), and Very Large Eddy Simulation (VLES).

DNS is a simulation in which the exact equations of fluid flow are solved directly without any turbulence model. This approach requires that the whole range of time and length scales of turbulence must be resolved. As a result, the computation time for completing a DNS simulation is usually very high. It increases with both the number of time steps and the number of grid cells.

The LES method resolves the large scales of turbulence but models smaller ones. This means that the results provided by an LES simulation are less accurate than those obtained from a DNS simulation. However, the former approach saves time compared to the latter because the small scales of turbulence are those that require the highest computational cost.

The VLES approach represents a good compromise between the accuracy and the computational time of a simulation. It belongs to the large-scale simulation method. VLES is particularly used for those applications in which LES simulation remains computationally expensive. These circumstances generally occur in the case of high to very-high Reynolds number flow conditions. FDS employs the VLES approach as the default method.

The LES and VLES simulations require a model for turbulent viscosity, which is the most important transport coefficient in FDS. The code offers a wide variety of methods for modeling turbulent viscosity, including the Constant coefficient Smagorinsky model, the Dynamic Smagorinsky model, the Vreman's eddy viscosity model, and Deardorff's model. Based on a comparison of results obtained from a vast range of large-scale experiments, FDS uses Deardorff's model as the default model.

Wall functions are often applied to model the turbulent boundary layer adjacent to solid objects such as walls. They save computing time by preventing the need to solve in detail the turbulent boundary layer near walls, which would require a large number of grid cells. These functions include parameters referring to the roughness of the walls. FDS provides two different approaches for modeling near-wall turbulence: damping function and WALE model.

2.2.1.2. Combustion model

The rate of the combustion reaction of fuel and oxygen depends on the local concentrations of the reactants, the local temperature, and other parameters related to the mechanism of the reaction, which is often unknown or too difficult to model. In light of this, a number of methods, based on certain simplified assumptions about the above-mentioned mechanism, have been developed in order to model the combustion phenomena.

FDS offers two alternative approaches for combustion modeling. On the one hand, it is possible to assume that the reaction between fuel and oxygen is governed only by mixing and is infinitely fast. This first method, known as *mixing-controlled*, is used as the default model in the code. On the other hand, the rate of the combustion reaction is considered to be *finite*. However, this second approach is computationally expensive because it requires a large number of grid cells, which is not practical for large-scale experiments.

2.2.1.3. Thermal radiation model

Thermal radiation plays a key role in the mechanism of heat transfer in a fluid, more especially when temperatures exceed 600 K (*Gobeau et al., 2002*). For a large fire, in fact, it can represent up to 30-40% of the heat released (*Mégret and Vauquelin, 2000*).

Radiative heat transfer occurs between emitters and receivers (e.g., solid surfaces). In this regard, the main sources of radiation are soot, CO_2, and H_2O. The former emits energy at all wavelengths, contrary to CO_2 and H_2O that emit radiation in discrete bands.

FDS includes radiative heat transfer in the model through the solution of the Radiation Transport Equation (RTE) for a grey gas, as well as employing a wide band model in certain limited circumstances. The code uses a technique similar to the Finite Volume Method (FVM) for solving the above-mentioned equation.

FDS offers the possibility of improving the spatial and temporal accuracy of the RTE equation, but not without increasing the computational cost. The spatial resolution can be enhanced by increasing the number of radiation angles from the default value of 100. Instead, the temporal accuracy of the RTE equation can be improved by decreasing the number of time steps for which this equation is fully updated; the default value is 15. Spatial resolution is much more important than the temporal resolution.

2.2.2. Validation

As reported above, the FDS code has been validated for a vast range of fire scenarios (*McGrattan et al., 2019c*), as well as used to estimate fire-induced threats (e.g., gas and wall surface temperatures, velocity and direction of airflow, smoke and toxic gases concentration, convective and radiative heat transfer), essential for assessing both the risk level for tunnel users and damage to the structure. However, preliminary simulations are usually carried out to improve confidence with the code, as well as to understand the limits and potential of the proposed models in order to prevent misleading results.

The accuracy of the results and the computational time of a simulation depend more especially on the grid fineness and the physical models used. The sensitivity of the FDS code to these factors can be assessed by comparing its results with experimental tunnel fire data available in the literature. This comparison is generally made by simulating small-scale experiments in order to avoid excessive computational time. It is to be stressed that the results of these preliminary analyses will be important for setting up the model developed to predict fire-induced damage.

2.2.2.1. Reduced-scale experiment

The basic sketch and coordinate system of the reduced-scale tunnel (*Xue et al., 2001*) are shown in Fig. 2.1. This tunnel was 6 m long with a rectangular cross-section of 0.9 m wide and 0.3

m high. The fire source was located at 1.5 m from the tunnel inlet section (X = 0) in the middle (Z = 0) of the floor level (Y = 0). The burner was 0.18 m long (x-axis) and 0.15 m wide (z-axis). The fuel consisted of Liquefied Petroleum Gas (LPG).

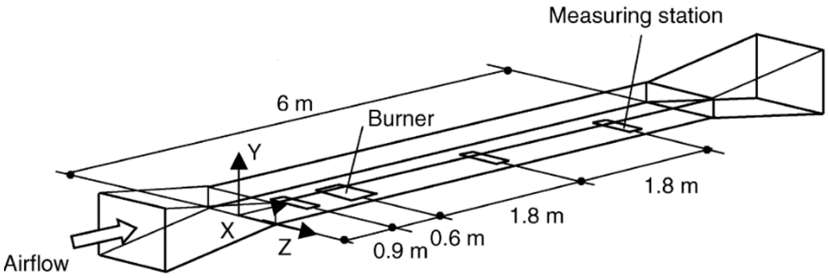

Fig. 2.1. Reduced-scale experiment: a sketch of the tunnel fire.

The majority of the reduce-scale tunnel was made of perspex (i.e., an insulating material) with a thickness of 8 mm, while aluminum and silica glass were used for the floor and ceiling areas near the fire source. The longitudinal ventilation was due to an axial fan located at the inlet section of the tunnel. The ambient temperature was 300 K.

The test was carried out considering two steady-state heat release rates (i.e., 3.15 kW and 4.75 kW) and four different ventilation flow velocities (i.e., 0.13 m/s, 0.31 m/s, 0.52 m/s, and 0.61 m/s). The experimental data were expressed as temperature profiles along the vertical axis at the center of the tunnel (Z = 0) in three cross-sections located both upstream (X = 0.9 m) and downstream (X = 3.3 m and X = 5.1 m) of the fire source. However, test results were only reported for some of the above-mentioned scenarios. In this regard, the most detailed experimental data were available for a steady-state HRR of 3.15 kW and a ventilation velocity of 0.13 m/s. Therefore, the reduced-scale tunnel was reproduced with respect to these conditions of HRR and ventilation.

2.2.1.1.1. Common settings

The longitudinal ventilation of 0.13 m/s was assumed to be uniformly distributed over the inlet section of the tunnel (X = 0). Instead, the HRR of 3.15 kW was applied to the entire burning surface (0.15 x 0.18 m^2), which means that the Heat Release Rate per Unit Area (HRRPUA) was 116.67 kW/m^2.

The near-wall turbulence was modeled using the WALE model. The mixing-controlled approach was employed for combustion modeling.

The sensitivity of the FDS code was evaluated with respect to:

- Mesh resolution;
- Turbulence model;
- Turbulent viscosity model;
- Thermal radiation model;
- Pressure iterations.

2.2.1.1.2. Mesh resolution

The first simulations were carried out to assess the influence of the grid size on the results. The VLES approach (default) for turbulence and Deardorff's model (default) for turbulent viscosity were selected in these analyses. The default values of 100 and 15 were set for the spatial and temporal resolution of the RTE equation, respectively. The maximum number of pressure iterations for each half of the time step was assumed to be equal to the default value of 10.

It is to be said that the FDS code performs all calculations within a rectilinear domain consisting of a certain number of parallelepiped cells, better if cubic. The mesh resolution depends on the number of cells in which the region of interest is discretized. In this regard, three different grid cells were used:

- Fine grid: 829,440 cubic cells of 1.25 cm side;
- Intermediate grid: 103,680 cubic cells of 2.5 cm side;
- Coarse grid: 30,720 cubic cells of 3.75 cm side.

From Fig. 2.2 one can see that the coarse grid was capable of reproducing the cold lower layer with good accuracy; but at the same time, it showed that the predicted temperature profiles along the tunnel height grew too fast compared to the experimental data. Instead, both the fine and intermediate grids, which provided similar results, were able to accurately reproduce the test data, more especially in the tunnel sections downstream of the fire source (Fig. 2.2b and Fig. 2.2c).

It is to be stressed that the fine grid, with a simulation time of about 12 days, was computationally expensive compared to the intermediate and coarse grids, which required a calculation time of approximately 10.8 hours and 6 hours, respectively.

On this basis, the findings showed that the intermediate grid represents an acceptable compromise between the accuracy of the results and the computational time. Therefore, this grid size was used for the other simulations.

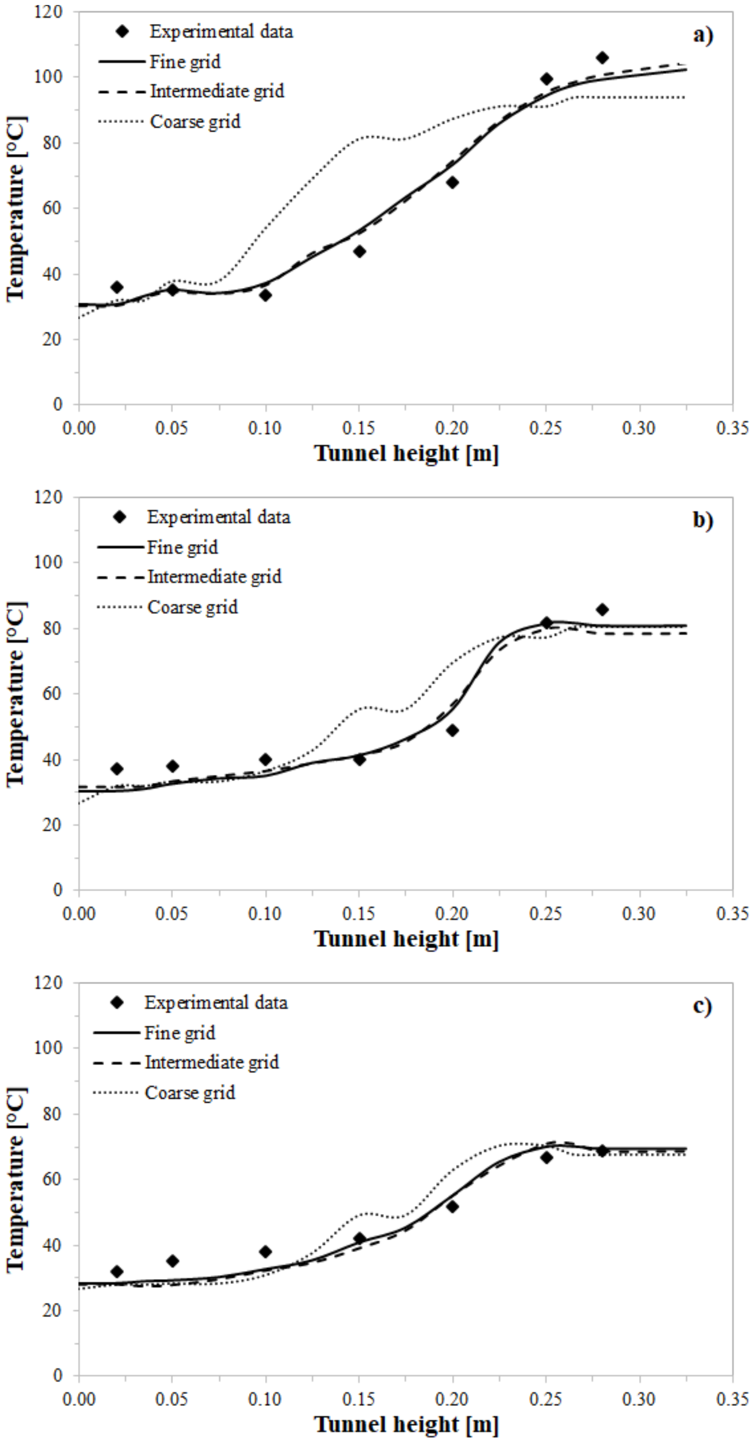

Fig. 2.2. Grid sensitivity analysis. Experimental and predicted temperature profiles along the tunnel height at the centerline: a) X = 0.9 m; b) X = 3.3 m; c) X = 5.1 m.

2.2.1.1.3. Turbulence model

In these runs, the Deardorff's model for turbulent viscosity, values of 100 for the spatial resolution and 15 for the temporal resolution of the RTE equation, a value of 10 as the maximum number of pressure iterations, and the previous intermediate grid were selected. Several simulations were carried out in order to study the influence of the turbulence model on the results. In this regard, the investigated cases concerned the following approaches for turbulence modeling:

- Direction Numerical Simulation (DNS);
- Large Eddy Simulation (LES);
- Very Large Eddy Simulation (VLES).

In particular, the FDS uses the VLES method by default.

The predicted temperature profiles for the DNS method were quite good in the sections downstream of the fire source and significantly underestimated upstream, except for the lower cold layer (Fig. 2.3). From Fig. 2.3 it is also possible to observe that the curves related to the VLES and LES approaches were nearly coincident and capable of accurately reproducing the experimental data both upstream and downstream of the burning surface. It is to be stressed that the DNS method, with a simulation time of about 31 hours, was computationally expensive compared to the LES and more especially VLES approaches, which required a calculation time of approximately 22.2 hours and 10.8 hours, respectively.

Therefore, the findings showed that the VLES approach represents an acceptable compromise between the accuracy of the results and the calculation time.

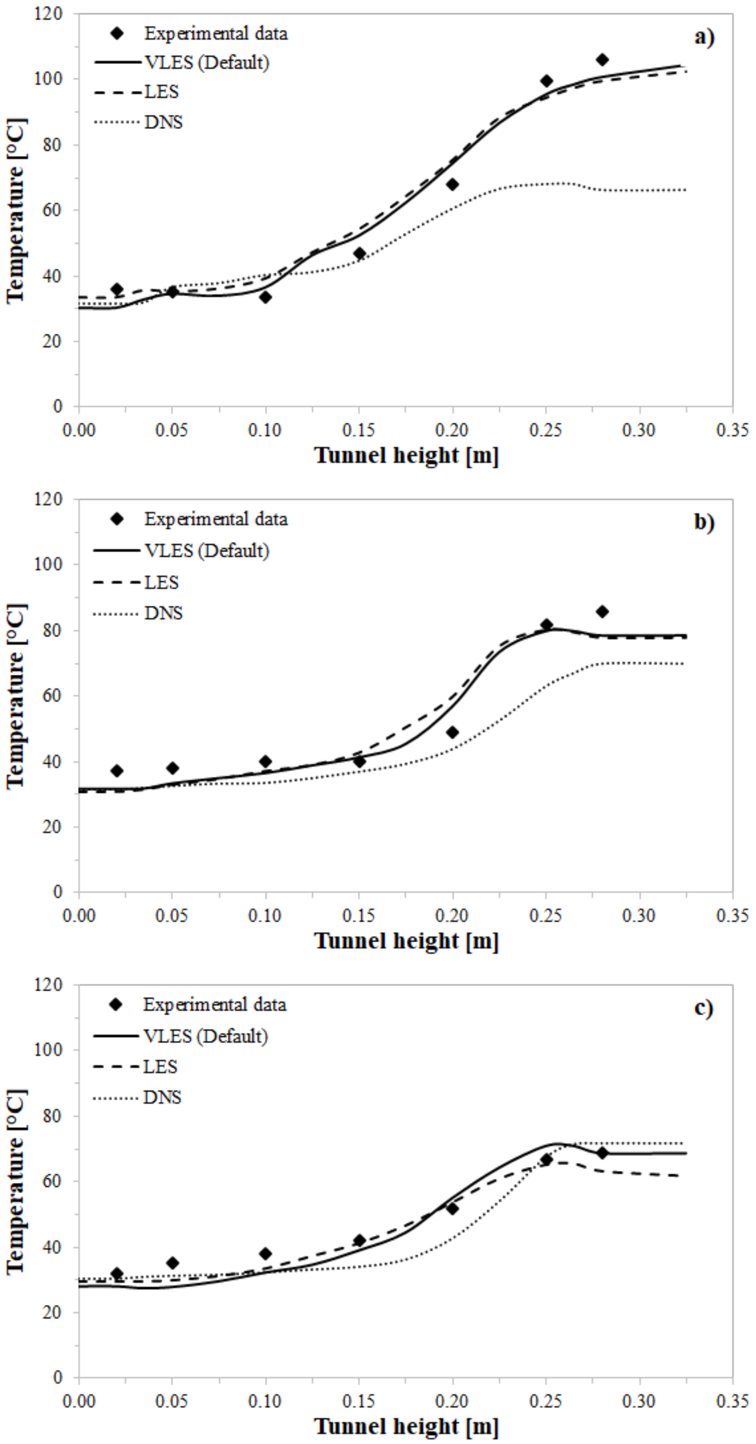

Fig. 2.3. Analysis of turbulence modeling. Experimental and predicted temperature profiles along the tunnel height at the centerline: a) X = 0.9 m; b) X = 3.3 m; c) X = 5.1 m.

2.2.1.1.4. Turbulent viscosity model

Several simulations were performed for studying the influence of the turbulent viscosity model on the capability of the FDS code to reproduce the test data. In this respect, the VLES method for turbulence, values of 100 for the spatial resolution and 15 for the temporal resolution of the RTE equation, a value of 10 as the maximum number of pressure iterations, and the previous intermediate grid were set.

The examined cases involved the following turbulent viscosity models:

- Constant coefficient Smagorinsky model;
- Dynamic Smagorinsky model;
- Vreman's eddy viscosity model;
- Deardorff's model.

Specifically, the FDS uses the latter by default.

From Fig. 2.4 one can see that all the investigated approaches provided similar results and were able to accurately reproduce the experimental data both upstream and downstream of the fire source. However, it is to be said that the simulation time was about 10.8 hours for the Deardorff's model, 21.1 hours for the Dynamic Smagorinsky model, 24 hours for the Constant coefficient Smagorinsky model, and 30.8 hours for the Vreman's eddy viscosity model.

Therefore, the results, expressed in terms of both predicted temperature profiles and computational time, suggested the use of the Deardorff's model for the other runs.

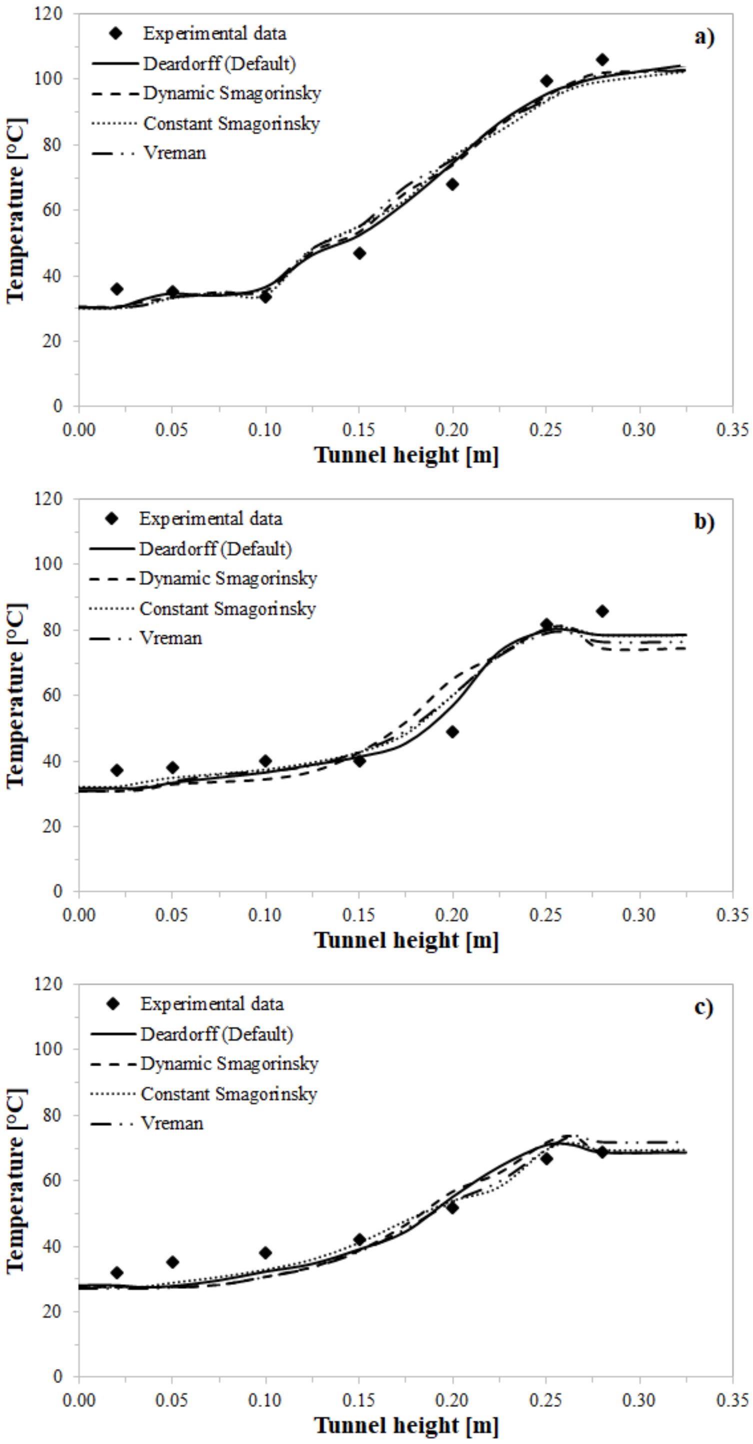

Fig. 2.4. Analysis of turbulent viscosity modeling. Experimental and predicted temperature profiles along the tunnel height at the centerline: a) X = 0.9 m; b) X = 3.3 m; c) X = 5.1 m.

2.2.1.1.5. Thermal radiation model: spatial resolution of the RTE equation

These simulations were carried out in order to evaluate the influence of the spatial resolution of the RTE equation on the results. For this aim, the VLES method for turbulence, the Deardorff's model for turbulent viscosity, a value of 15 for the temporal resolution of the RTE equation, a value of 10 as the maximum number of pressure iterations, and the previous optimized grid size were selected.

The spatial resolution of the RTE equation can be improved by setting a number of radiation angles greater than the default value of 100. In this respect, the investigated cases concerned the following number of radiation angles:

- 100;
- 1000;
- 2000.

Fig. 2.5 showed that the number of 100 radiation angles already provided accurate results, making a further increase unnecessary, also in relation to the calculation time. In fact, the simulation time increased as the number of radiation angles increased, passing from about 10.8 hours for 100 radiation angles to approximately 42 hours and 50 hours for 1000 and 2000 radiation angles, respectively.

Therefore, the results showed that the number of 100 radiation angles represents an acceptable compromise between the accuracy of the temperature profiles predicted along the tunnel height at the centerline and the computational time.

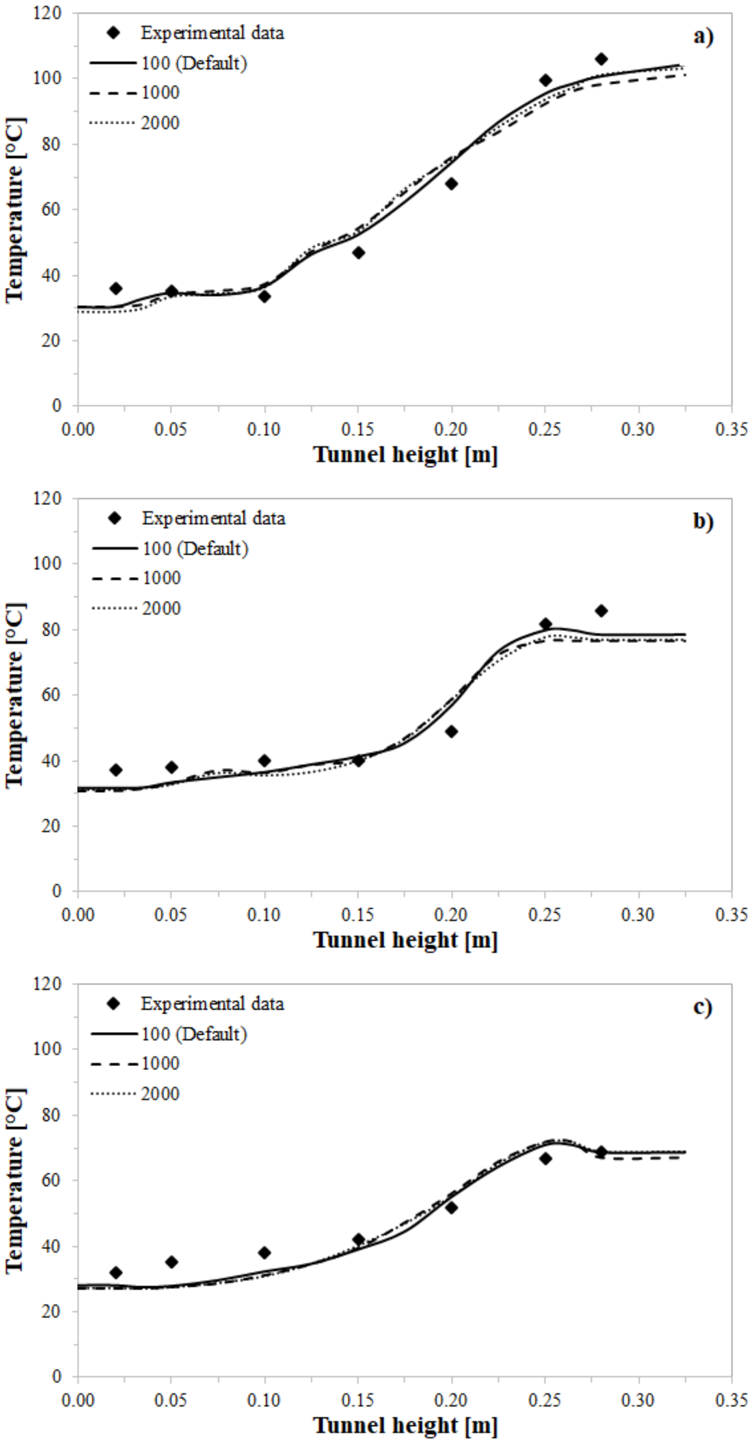

Fig. 2.5. Analysis of the spatial resolution of the RTE equation. Experimental and predicted temperature profiles along the tunnel height at the centerline: a) X = 0.9 m; b) X = 3.3 m; c) X = 5.1 m.

2.2.1.1.6. Thermal radiation model: the temporal resolution of the RTE equation

The influence of the temporal resolution of the RTE equation on the results was assessed by setting the VLES method for turbulence, Deardorff's model for the turbulent viscosity, a value of 100 for the spatial resolution of the RTE equation, a value of 10 as the maximum number of pressure iterations and the previous intermediate grid.

The FDS tool permits to improve the temporal resolution of the RTE equation by decreasing the number of time steps for which this equation is completely updated; the default value is 15. In this regard, the investigated cases involved the following number of time steps:

- 15;
- 6;
- 1.

From Fig. 2.6 it is possible to observe that the predicted temperature profiles were similar to each other and to the experimental data, regardless of the number of time steps set. However, it is to be stressed that the computational time increased as the number of time steps decreased, going from about 10.8 hours for 15 time steps to approximately 25 hours and 43 hours for 6 time steps and 1 time steps, respectively.

Therefore, the findings showed that the number of 15 time steps was sufficient, thus representing an acceptable compromise between the accuracy of the results and the computational time.

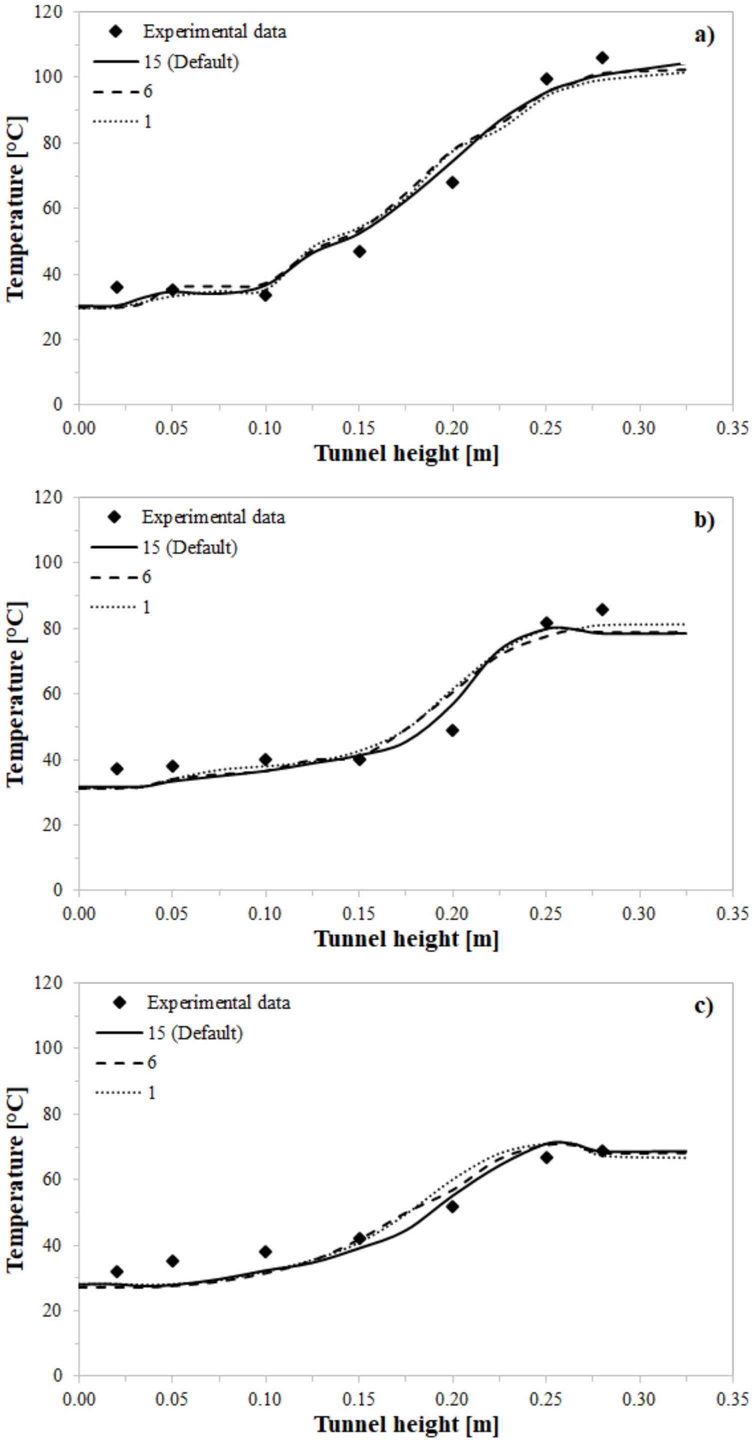

Fig. 2.6. Analysis of the temporal resolution of the RTE equation. Experimental and predicted temperature profiles along the tunnel height at the centerline: a) X = 0.9 m; b) X = 3.3 m; c) X = 5.1 m.

2.2.1.1.7. Pressure iterations

Several simulations were launched in order to evaluate the influence of the maximum number of pressure iterations for each half of the time step on the results. The VLES approach for turbulence, the Deardorff's model for turbulent viscosity, values of 100 for the spatial resolution and 15 for the temporal resolution of the RTE equation, and the previous intermediate grid were selected.

For this aim, the investigated cases concerned the following maximum number of pressure iterations:

- 10;
- 100;
- 200.

Specifically, the FDS code uses 10 as the default value of the maximum number of pressure iterations.

Fig. 2.7 showed that a value of 10 as the maximum number of pressure iterations provided results in good agreement with experimental data, making a further increase in the maximum number of pressure iterations unnecessary. In this regard, it is also to be said that the calculation time increased as the maximum number of pressure iterations increased, passing from about 10.8 hours for a maximum of 10 pressure iterations to approximately 20.5 hours and 25 hours for a maximum of 100 and 200 pressure iterations, respectively.

Therefore, the simulation findings suggested the use of a value of 10 as the maximum number of pressure iterations in order to save computational time without compromising the accuracy of the results.

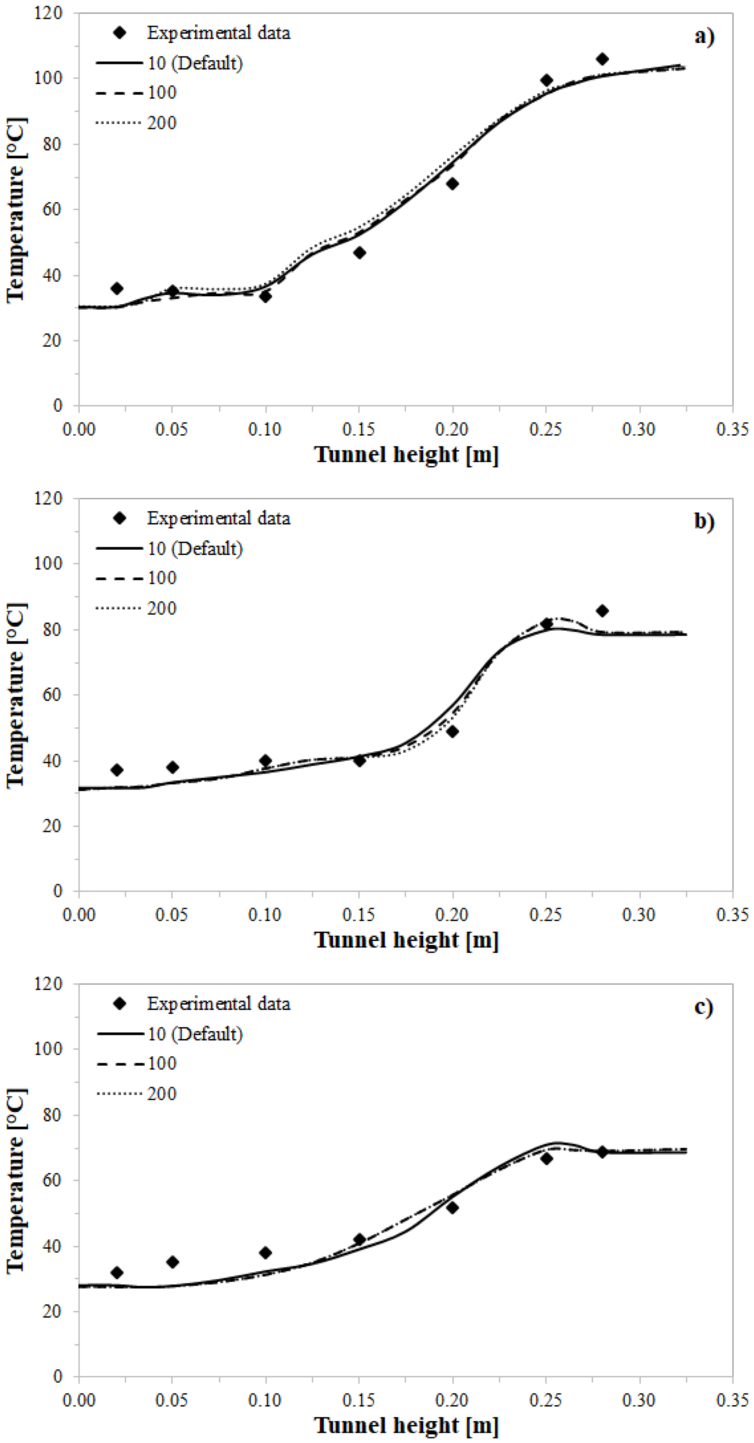

Fig. 2.7. Analysis of the maximum number of pressure iterations. Experimental and predicted temperature profiles along the tunnel height at the centerline: a) X = 0.9 m; b) X = 3.3 m; c) X = 5.1 m.

2.3. Conclusions

These preliminary simulations were carried out in order to evaluate the sensitivity of the FDS tool to certain factors and, hence, to assess the predictive capability of the code to reproduce fire-induced thermal and flow fields in the investigated reduce-scale tunnel.

Taken as a whole and on average, better results, expressed in terms of both predicted temperature profiles and computational time, could be obtained by setting: the VLES approach for turbulence, the Deardorff's model for turbulent viscosity, values of 100 for the spatial resolution and 15 for the temporal resolution of the RTE equation, a value of 10 as the maximum number of pressure iterations, and the intermediate grid size. The optimized model provided temperature profiles consistent with the experimental data, as shown and summarized in Fig. 2.8.

The simulation results in terms of global mass and heat balances were reported in Fig. 2.9 and Fig. 2.10, respectively. From Fig. 2.9 one can see that the mass was conserved, passing from 1.89 kg at the start of the simulation time (t = 0 min) to 1.74 kg at the end of the run (t = 200 min, steady-state). The heat was also conserved. In fact, the quantities Q_ENTH (enthalpy flow) and Q_TOTAL (total heat flow) were found to be very close to each other, indicating that the sources of energy loss and gain were correctly added and subtracted from the energy equation (Fig. 2.10).

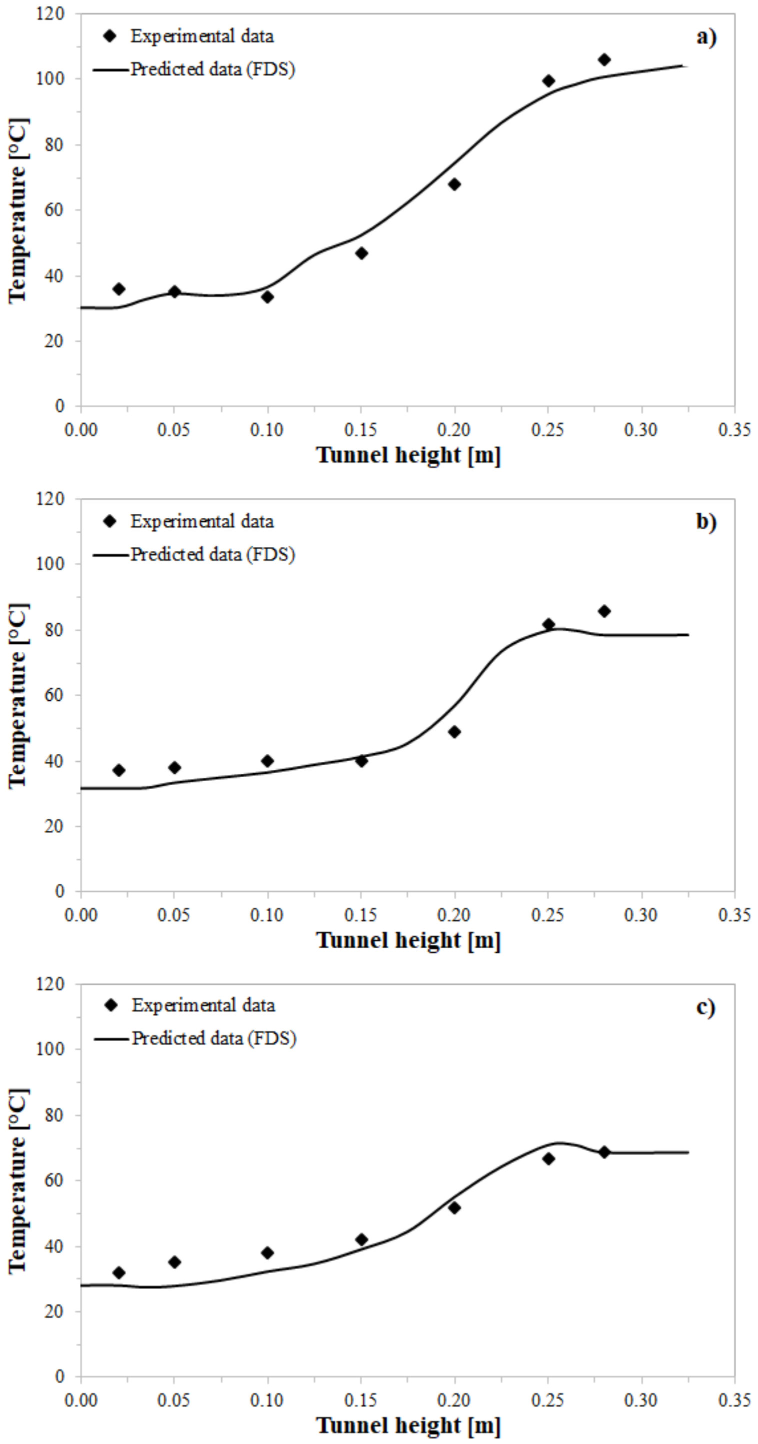

Fig. 2.8. Optimized model for the investigated reduce-scale tunnel. Experimental and predicted temperature profiles along the tunnel height at the centerline: a) X = 0.9 m; b) X = 3.3 m; c) X = 5.1 m.

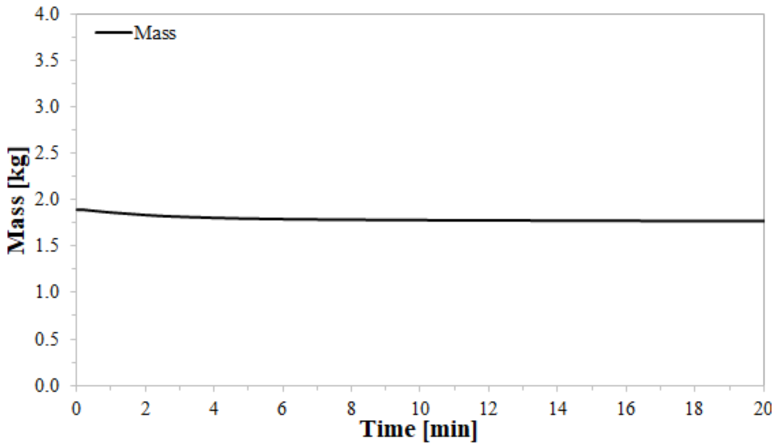

Fig. 2.9. Optimized model for the investigated reduce-scale tunnel. Global mass balance.

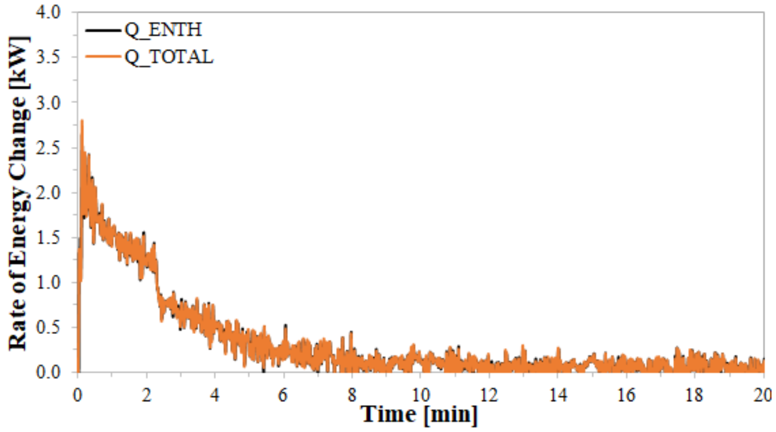

Fig. 2.10. Optimized model for the investigated reduce-scale tunnel. Global heat balance.

From Fig. 2.10 it is also possible to observe that, as expected, the net energy gain/loss went to zero when the compartment reached a quasi-steady state (for more detail see *McGrattan et al., 2019a*).

The global mass and heat balances were good indicators of how well the optimized model solution converged.

It is to be stressed that the results provided by this optimized model will be important for setting up the model developed to predict fire-induced damage.

2.4. References

[51] Forney, G.P., 2019. Smokeview: User's Guide. NIST, Special Publication 1017-1. Available online: https://pages.nist.gov/fds-smv/manuals.html (accessed on 13 March 2021).

[52] Gobeau, N., Ledin, H.S., Lea, C.J., 2002. Guidance for HSE Inspectors: Smoke movement in complex enclosed spaces - Assessment of Computational Fluid Dynamics. HSL/2002/29. Available online: http://www.fire-eng.co.za/Smoke%20study.pdf (accessed on 21 March 2021).

[53] McGrattan, K., Hostikka, S., Floyd, J., McDermott, R., Vanella, M., 2019a. Fire Dynamics Simulator: User's Guide. NIST, Special Publication 1019. Available online: https://pages.nist.gov/fds-smv/manuals.html (accessed on 13 March 2021).

[54] McGrattan, K., Hostikka, S., Floyd, J., McDermott, R., Vanella, M., 2019b. Fire Dynamics Simulator: Technical Reference Guide. Volume 1: Mathematical Model. NIST, Special Publication 1018-1. Available online: https://pages.nist.gov/fds-smv/manuals.html (accessed on 13 March 2021).

[55] McGrattan, K., Hostikka, S., Floyd, J., McDermott, R., Vanella, M., 2019c. Fire Dynamics Simulator: Technical Reference Guide. Volume 3: Validation. NIST, Special Publication 1018-3. Available online: https://pages.nist.gov/fds-smv/manuals.html (accessed on 13 March 2021).

[56] Mégret, O., Vauquelin, O., 2000. A model to evaluate tunnel fire characteristics. Fire Safety Journal 34, 393-401.

[57] Xue, H., Ho, J., Cheng, Y., 2001. Comparison of different combustion models in enclosure fire simulation. Fire Safety Journal 36 (1), 37-54.

Chapter 3

Spalling: 3D FDS modeling

3.1. Introduction

On the basis of previous results and the confidence gained in the application of the FDS tool to tunnel fires, in this Chapter an original 3D CFD model capable of reproducing the development of a tunnel fire and estimating the resulting spalling is presented. The reliability of the proposed model in predicting fire-induced damage is demonstrated by comparing its results with those obtained from a competing model available in the international literature.

Using the developed 3D CFD model, several simulations are carried out in order to better highlight the role played by the critical temperature (i.e., the temperature at which spalling might occur), which can be in the wide temperature range of 250-700 °C, on the severity of fire-induced damage over time. In addition, the results provided by the proposed 3D CFD model are also compared with those obtained from a conventional heat transfer analysis in which spalling is not taken into account.

3.2. Tunnel description

3.2.1. Tunnel geometry

The investigated tunnel is a two-lane unidirectional road tunnel with a length of 1 km. It has a rectangular cross-section of 63 m^2 with a width of 10.5 m (both lanes have a width of 3.75 m) and a height of 6 m. The tunnel is straight and flat with no emergency lanes. In addition, on each side of the tunnel, there is a sidewalk and a shoulder, which divides the driving lane from the sidewalk, having a width of 1 m and 0.5 m, respectively.

Fig. 3.1 shows the cross-section of the investigated tunnel.

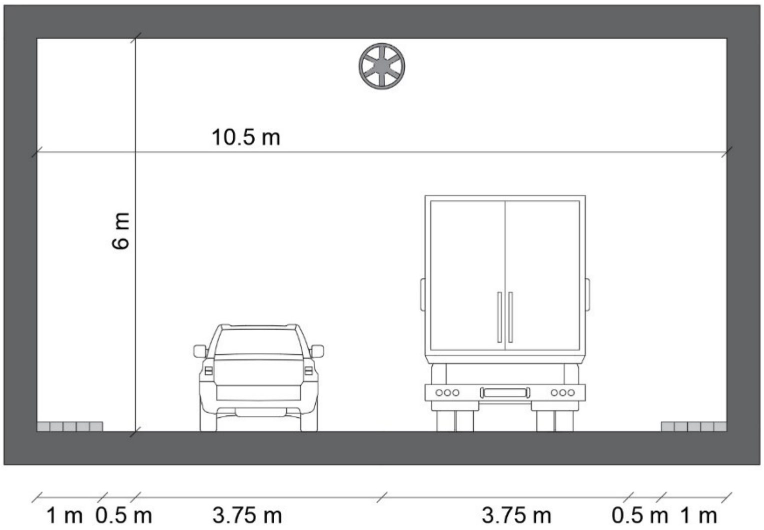

Fig. 3.1. Cross-section of the investigated tunnel.

3.2.2. Ventilation system

The investigated tunnel is equipped with a mechanical ventilation system consisting of five axial jet fans located along the ceiling centerline. Each jet fan has a diameter of 0.7 m and a length of 2 m. It has a capacity (maximum velocity) of 30 m/s and is capable of providing an airflow rate of up to about 11.5

m^3/s. The jet fans are located along the tunnel at intervals of 150 m with the first one situated at a distance of 125 m from the entrance portal.

In ordinary traffic conditions, the ventilation within the tunnel is natural and is due to the piston effect of moving vehicles. In these circumstances, the airflow along the tunnel has an average velocity of about 0.5 m/s. In the event of a fire emergency, instead, the activation of all jet fans after 2 min from the fire start guarantees an average airflow velocity within the tunnel of around 5 m/s in order to prevent backlayering phenomena. In fact, in one-way tunnels where vehicles are likely to be located upstream of the fire, the mechanical ventilation system should be able to prevent backlayering (*NFPA 502, 2011*). In this respect, by performing several preliminary simulations, it was found that values less than 5 m/s of the average airflow velocity within the tunnel under emergency conditions did not prevent backlayering. This value of 5 m/s is slightly higher than that indicated by *PIARC (1999)* of 3 m/s for a HRR not exceeding 100 MW and a slope lower than 4%.

3.2.3. Material properties

3.2.3.1. Bituminous conglomerate

The road pavement of the investigated tunnel has a thickness of 0.25 m and is made of bituminous conglomerate.

In the present work, the bituminous conglomerate is characterized by the following properties (*The Engineering ToolBox*), which are assumed to be temperature-independent:

- Thermal conductivity (λ) is 0.75 W/(mK);
- Specific heat (c) is 0.92 kJ/(kgK);
- Emissivity (ε) is 0.93;
- Density (ρ) is 2360 kg/m^3.

It is to be stressed that although the properties of the bituminous conglomerate were set in the model, the possible combustion of the road pavement during the fire was not considered in this thesis. In this respect, a possible extension of the present study might be to assess whether the combustion of the road pavement affects, and hence to what extent, the spalling damage of concrete structures.

3.2.3.2. Concrete

The walls and ceiling of the investigated tunnel consist of a 0.5 m thick layer of High Strength Concrete (HSC) with a moisture content of 3% by weight of concrete. The thermal properties (i.e., thermal conductivity and specific heat) of the HSC are assumed to be temperature-dependent.

Eurocode 2 (2004) provided two experimental relationships representing the upper and lower limit values of the thermal conductivity of concrete as a function of its temperature (θ), which is assumed to be in the range of 20-1200 °C.

The upper limit of the thermal conductivity of concrete might be determined by the following equation:

$$(3.1)\ \lambda = 2 - 0.2451(\theta/100) + 0.0107(\theta/100)^2,$$

with λ expressed in W/(mK).

Instead, the lower limit of the thermal conductivity of concrete might be determined using this other equation:

(3.2) $\lambda = 1.36 - 0.136(\theta/100) + 0.0057(\theta/100)^2$,

where λ is always in W/(mK).

The upper and lower limits of the thermal conductivity of concrete as a function of its temperature are shown in Fig. 3.2.

The above-mentioned relationships may be applied to both high strength concretes and normal strength concretes. However, since the thermal conductivity of HSCs might be higher than that of NSCs (*Eurocode 2, 2004*), the upper limit of the thermal conductivity of concrete is used in the present work.

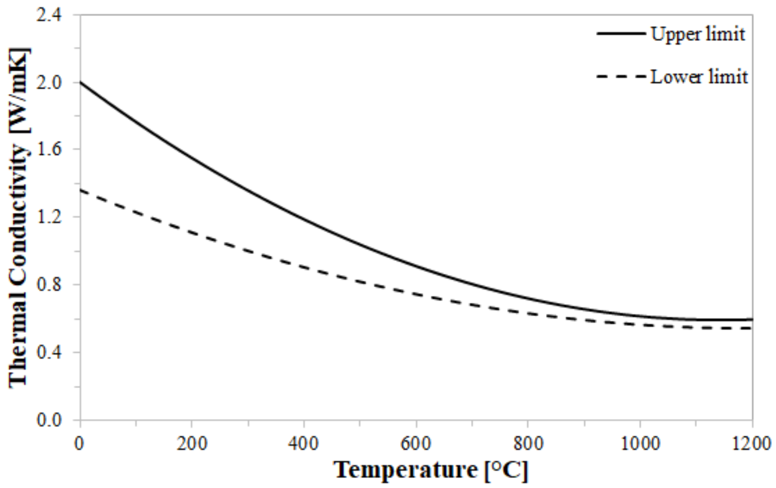

Fig. 3.2. Thermal conductivity of concrete as a function of its temperature.

Eurocode 2 (2004) also proposed an experimental relationship that describes, based on the moisture content of concrete, the dependence of the specific heat of concrete on its temperature.

The specific heat of concrete for a moisture content of 3% by weight of concrete might be determined by the following equations:

$$(3.3)\quad c = 900 \qquad \text{for } 20\,°\mathrm{C} \le \theta \le 100\,°\mathrm{C}$$

$$c = 2020 \qquad \text{for } 100\,°\mathrm{C} \le \theta \le 115\,°\mathrm{C}$$

$$c = 1000 + 1020\frac{200-\theta}{85} \qquad \text{for } 115\,°\mathrm{C} \le \theta \le 200\,°\mathrm{C}$$

$$c = 1000 + \frac{\theta-200}{2} \qquad \text{for } 200\,°\mathrm{C} \le \theta \le 400\,°\mathrm{C}$$

$$c = 1100 \qquad \text{for } 400\,°\mathrm{C} \le \theta \le 1200\,°\mathrm{C},$$

with c expressed in J/(kgK).

Fig. 3.3 shows the specific heat of concrete as a function of its temperature for a moisture content of 3% by weight of concrete.

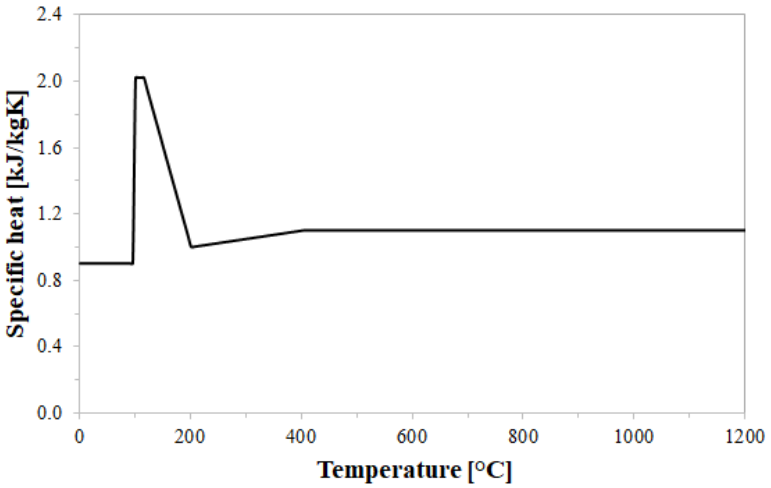

Fig. 3.3. Specific heat of concrete as a function of its temperature for a moisture content of 3% by weight of concrete.

The emissivity of concrete is assumed to be temperature-independent and equal to 0.9.

Since the variation of concrete density with its temperature can be neglected (*Eurocode 2, 2004*), the density of concrete is assumed to be constant and equal to 2585 kg/m^3 (*Schrefleret et al., 2002*).

3.3. Fire scenario

The fire source consists of a HGV with a length of 12 m, a width of 2.5 m, and a height of 3.2 m. It is schematized as a parallelepiped positioned at 0.4 m from the road pavement. The burning vehicle is assumed to be located close to the right sidewalk in the middle of the tunnel length in order to simulate the worst-case fire scenario (*Caliendo et al., 2012, 2013, 2018, 2021a, 2021b, 2021c*).

On this basis, the ceiling and more especially the right wall of the investigated tunnel are the concrete elements most susceptible to spalling due to their reduced distance from the fire source. In fact, if the horizontal distance between the left wall and the lateral surface of the HGV is 7 m, the vertical distance from the ceiling to the upper surface of the fire source is 2.4 m, while the horizontal distance between the right wall and the lateral surface of the burning vehicle is 1 m. In light of these, the fire-induced damage will subsequently be evaluated with reference to the ceiling and the right wall.

The burning vehicle is capable of developing a fire characterized by a maximum HRR (HRR_{max}) of 100 MW, which corresponds to a peak Heat Release Rate per Unit Area ($HRRPUA_{max}$) of 654.45 kW/m^2. Specifically, the HRR (or HRRPUA) is assumed to grow according to a linear law until it reaches its peak (100 MW) after 5 min from the fire start, then follows a phase with constant fully developed HRR.

Fig. 3.4 shows the HRR curve over time.

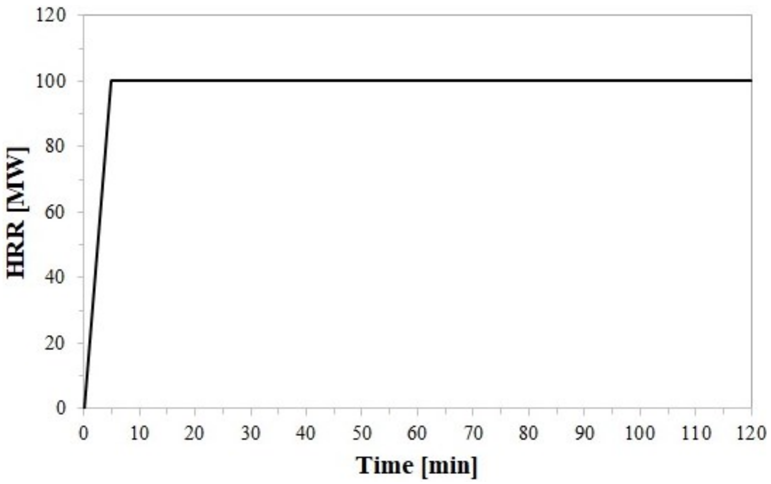

Fig. 3.4. HRR curve over time.

ITA (2004) and *PIARC (2007)* require that the main structure of a tunnel be able to resist the exposure of one between the RWS and HC_{mod} fire curves for at least 120 min. In this Chapter, therefore, all fire simulations are carried out for 120 min. In other terms, the fire duration is assumed to be 120 min.

The fuel, consisting of 80% wood pallets and 20% plastic, is described by the following chemical formula $CH_2O_{0.62}$ (*Wang et al., 2016*). The yields of soot and CO are 0.025 g/g and 0.15 g/g, respectively (*FIT, 2005*). The heat of combustion, instead, is 25 MJ/kg (*SFPE, 1995*).

Caliendo et al. (2013) found that the presence of traffic within the tunnel during a fire led to an increase in maximum temperatures compared to the fire scenario with an isolated burning vehicle (i.e., no traffic). In the present thesis, therefore, it is assumed that the investigated tunnel is full of cars stopped upstream of the fire source when the fire start. The vehicles in the queue are modeled as rectangular blocks placed at 0.2 m from the road pavement. Specifically, each car is 6 m long, 1.8 m wide, and 1.5 m high. The first queued vehicle is located at 10 m upstream of the fire source, while the distance between the stopped cars is 2 m. The total number of cars in the queue upstream of the burning vehicle is 120 (i.e., 60 vehicles per lane).

Fig. 3.5 shows the schematic layout of queued vehicles upstream of the fire source.

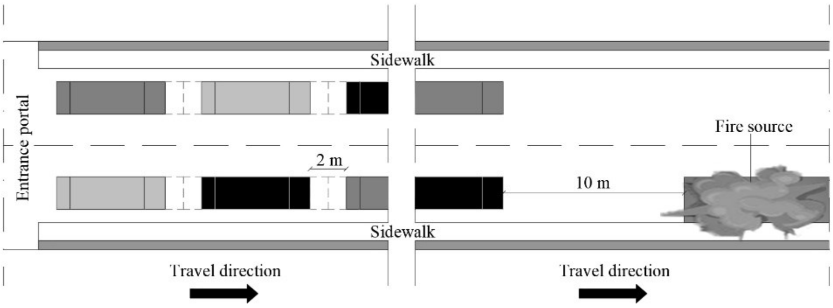

Fig. 3.5. Schematic layout of queued vehicles upstream of the fire source.

3.4. Grid sensitivity analysis

Generally speaking, the accuracy and reliability of fire-induced damage prediction depend mainly on the mesh resolution. However, the simulation time may increase drastically when the tunnel volume is discretized into cells that are too fine, more especially if the investigated tunnel is too long. Therefore, since the use of a very fine mesh is required for an accurate assessment of fire-induced damage, spalling is usually evaluated by considering only a portion of the entire tunnel, as well as using two different cell sizes for the internal volume of the tunnel and for the thickness of the concrete elements.

On this basis, two successive grid sensitivity analyses are carried out. The first is used in order to define the optimal mesh resolution for the internal space of the tunnel, as well as to determine the length of the tunnel portion most susceptible to spalling. The second served to identify the optimal mesh resolution for the concrete elements.

3.4.1. Mesh resolution for the internal space of the tunnel

As mentioned above, both the accuracy and calculation time of a simulation depend mainly on the mesh resolution. On this basis, a grid sensitivity analysis is performed for defining the optimal mesh resolution for the internal space of the tunnel.

The FDS code suggests the following non-dimensional expression in order to define the optimal mesh resolution (*McGrattan et al., 2019a*):

(3.4) D^*/δ_x,

where δ_x is the nominal size grid [m], while D^* is the characteristic length scale [m] expressed as follows:

(3.5) $D^* = \left(\frac{Q}{\rho_\infty c_p T_\infty \sqrt{g}}\right)^{\frac{2}{5}}$,

where Q is the HRR (i.e., 100,000 kW), ρ_∞ is the density of air (i.e., 1.204 kg/m^3), c_p is the specific heat of air (i.e., 1.005 J/(kgK)), T_∞ is the ambient temperature (i.e., 293 K), and g is the gravity acceleration (i.e., 9.81 m/s^2).

According to the FDS user's guide (*McGrattan et al., 2019a*), D^*/δ_x should be in the range of 4-16 in order to achieve an appropriate mesh resolution. In this regard, D^* is equal to 6.1

m for the investigated fire scenario. This means that the cell size should be between 0.38 m and 1.52 m. It is to be stressed that the FDS tool carries out all calculations within a rectilinear domain consisting of a given number of parallelepiped cells, preferably cubic. On this basis, this grid sensitivity analysis is carried out by considering three different cubic cell sizes:

- 0.25 m (4,928,000 cubic cells);
- 0.5 m (616,000 cubic cells);
- 1 m (77,000 cubic cells).

Fig. 3.6 shows the temperature predictions as a function of the cell size.

The temperatures shown in Fig. 3.6 are measured in two different cross-sections located at 16 m upstream and 10 m downstream of the fire center. Specifically, the former corresponds to the cross-section where the first vehicle in the queue (i.e., the car closest to the HGV) is assumed to stop; with respect to this cross-section, temperatures are detected at points placed at a distance (h) of 0.1 m, 4 m, and 5.9 m from the road pavement along the vertical axis for the center of the fire source. Instead, the other cross-section is located immediately downstream of the burning vehicle (i.e., 4 m from the front surface of the HGV) in order to capture the highest temperatures, which are expected downstream of the fire source due to the longitudinal ventilation that pushes the hot gases towards the tunnel exit portal. With reference to the latter cross-section, temperatures are measured at points located at a distance (h) of 4 m and 5.9 m from the road pavement along the vertical axis for the fire center, as well as at 4 m from the road pavement close to the right wall surface.

In general, the location of the cited points is chosen in order to highlight the effect of the grid size over the entire range of expected temperatures.

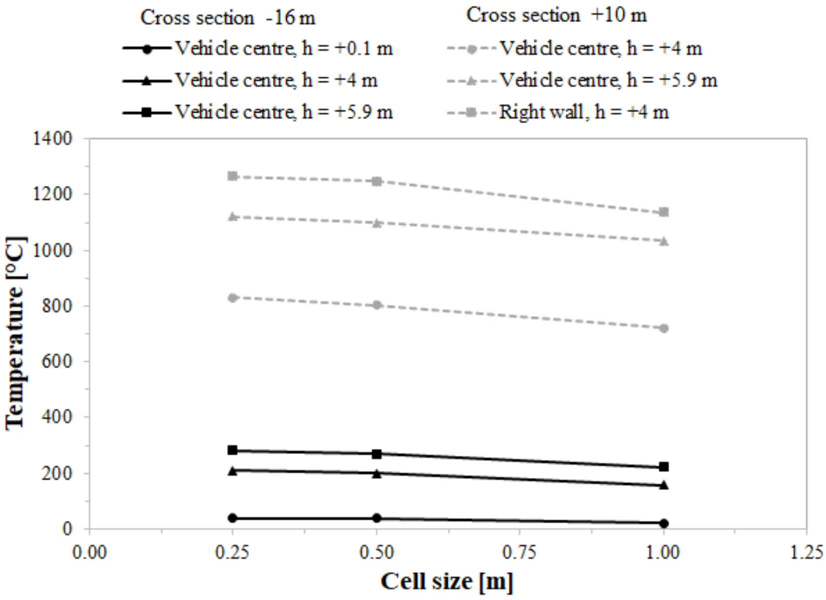

Fig. 3.6. Mesh resolution for the internal space of the tunnel. Temperature predictions as a function of the cell size.

From Fig. 3.6 one can see that cell sizes smaller than 0.5 m did not provide substantial differences in temperature predictions (differences not exceeding 5%), although the computation time increased significantly with mesh fineness. In other terms, cubic cells of 0.5 m side represent an acceptable compromise between the accuracy of the results and the simulation time.

In the light of the above considerations, the internal space of the tunnel is discretized into cubic cells of 0.5 m side.

Fig. 3.7 shows the optimal mesh resolution for the internal space of the tunnel.

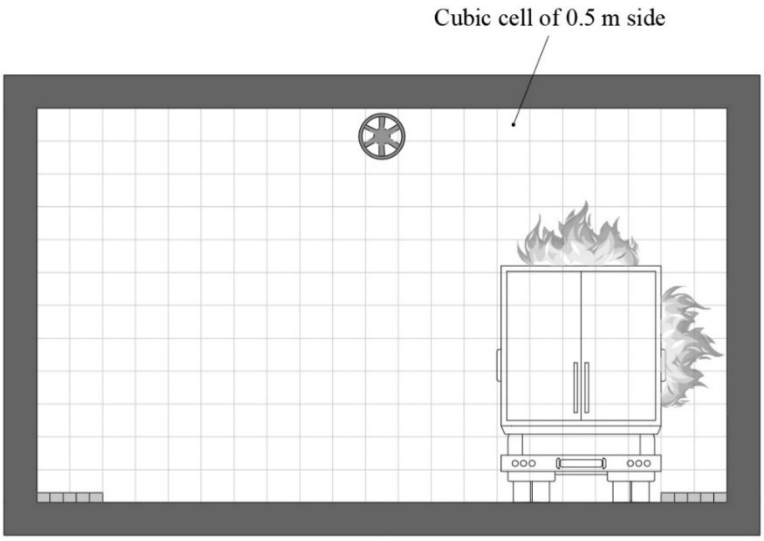

Fig. 3.7. Optimal mesh resolution for the internal space of the tunnel.

It is also to be said that these simulations were stopped when the predicted temperatures have reached a quasi-steady state.

3.4.2. Identification of the tunnel portion most susceptible to spalling

As mentioned above, spalling is usually assessed by considering only a portion of the entire tunnel, more especially if it is too long. In this way, in fact, the increment in computational cost due to the use of a very fine mesh within the thickness of the concrete elements, which are necessary to accurately assess fire-induced damage, is balanced by the reduction of the calculation domain.

Since hot gases tend to rise and be pushed towards the tunnel exit portal by longitudinal ventilation, the temperatures measured beneath the ceiling are on average higher than those along the right wall. As a result, the tunnel portion most susceptible to spalling is identified using the maximum surface temperature profile predicted along the ceiling. In this regard, it is to be stressed that fire-induced damage usually occurs for concrete surface temperatures above 250 °C.

Fig. 3.8 shows the maximum concrete surface temperature profile predicted along the ceiling of the investigated tunnel. Specifically, this temperature profile passes through the point at which the maximum concrete surface temperature beneath the ceiling was measured. The mentioned point is located at a distance (w) of 1.25 m from the right wall and at 9.25 m downstream of the fire center.

From Fig. 3.8 one can see that the tunnel portion affected by concrete surface temperatures above 250 °C has a length of about 65 m, of which 15 m upstream and 50 m downstream of the fire center.

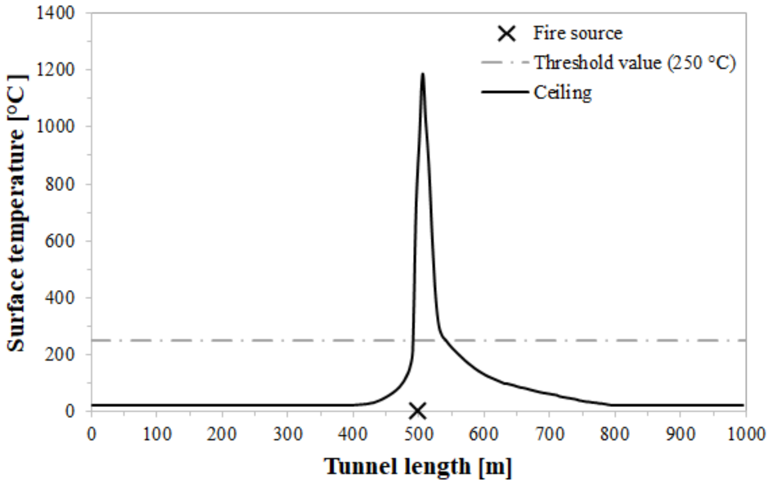

Fig. 3.8. Maximum concrete surface temperature profile predicted along the ceiling of the investigated tunnel.

It is to be said that the tunnel portion most susceptible to spalling is downstream of the burning vehicle due to the longitudinal ventilation that pushes the hot gases towards the tunnel exit portal.

Therefore, a 65 m long portion, including 15 m upstream and 50 m downstream of the fire center, of the entire tunnel (1 km long) is taken into account in order to assess spalling due to the HGV fire.

3.4.3. Mesh resolution for concrete elements

The accuracy and reliability of spalling prediction depend more especially on the grid size used in the depth of the concrete elements.

On this basis, a second grid sensitivity analysis is carried out in order to define the optimal mesh resolution within the thickness of the concrete elements. In this respect, it is worth remembering that the internal space of the investigated tunnel portion (65 m long) was divided into cubic cells of 0.5 m side.

As mentioned above, in order to accurately estimate spalling damage, it is necessary to use a very fine mesh in the depth of the concrete elements. However, simulation times become prohibitive (i.e., on the order of months) when using cubic cells that are too small. Therefore, the above-cited grid sensitivity analysis is performed by considering not a cubic grid but four different parallelepiped cell sizes (length x width x depth):

- 0.5 x 0.5 x 0.025 m^3 (130,780 parallelepiped cells);
- 0.5 x 0.5 x 0.05 m^3 (83,980 parallelepiped cells);

- 0.5 x 0.5 x 0.1 m^3 (60,580 parallelepiped cells);
- 0.5 x 0.5 x 0.125 m^3 (55,900 parallelepiped cells).

On this basis, both the width and the length of the parallelepiped cell are set to 0.5 m, while its height can assume four different values.

In addition, it is to be stressed that the concrete elements most susceptible to spalling are the ceiling and the right wall due to their reduced distance from the burning vehicle. Therefore, the thickness of both the left wall and the road pavement is also divided into cubic cells of 0.5 m side in order to save computational costs. In other terms, the following grid sensitivity analysis is aimed at identifying the optimal mesh resolution within the thickness of only the ceiling and the right wall of the investigated tunnel portion.

Fig. 3.9 shows the temperature predictions as a function of the height of the parallelepiped cell.

Temperatures shown in Fig. 3.9 are measured within the thickness of both the ceiling and the right wall at points located at a depth of 0.01 m, 0.05 m, and 0.1 m from the point where the highest concrete surface temperature is predicted on each of these structural elements. In this respect, the maximum concrete surface temperature beneath the ceiling (h = 6 m) is measured at a point located at a distance (w) of 1.25 m from the right wall and at 9.25 m downstream of the fire center. Instead, the maximum concrete surface temperature along the right wall (w = 0) is predicted at a point placed at a distance (h) of 0.25 m from the road pavement and at 4.75 m downstream of the fire center.

In general, the location of the cited points is chosen in order to highlight the effect of the grid size over the entire range of expected temperatures.

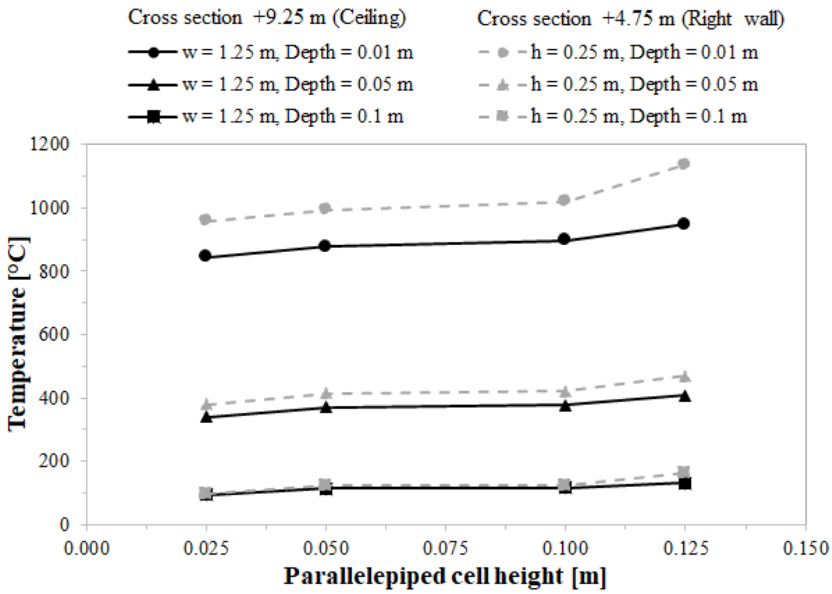

Fig. 3.9. Mesh resolution for concrete elements. Temperature predictions as a function of the parallelepiped cell height.

From Fig. 3.9 one can see that parallelepiped cell heights smaller than 0.1 m did not provide substantial differences in temperature predictions (differences not exceeding 5%), although the computation time increased significantly with mesh fineness (i.e., about 5 days, 3 days, 2 days, and 1 day for parallelepiped cell heights of 0.025 m, 0.05 m, 0.1, and 0.125 m, respectively). This means that the cell height of 0.1 m represents an acceptable compromise between the accuracy of the results and the simulation time.

In the light of the above considerations, the thickness of both the ceiling and the right wall is discretized into parallelepiped cells of (length x width x depth) 0.5 x 0.5 x 0.1

m^3, while the internal space of the investigated tunnel portion, the left wall, and the road pavement are divided into cubic cells of 0.5 m side in order to save calculation costs. As a result, the proposed 3D CFD model consists of 60,580 cells.

Fig. 3.10 shows the optimal mesh resolution for a generic cross-section of the investigated tunnel portion.

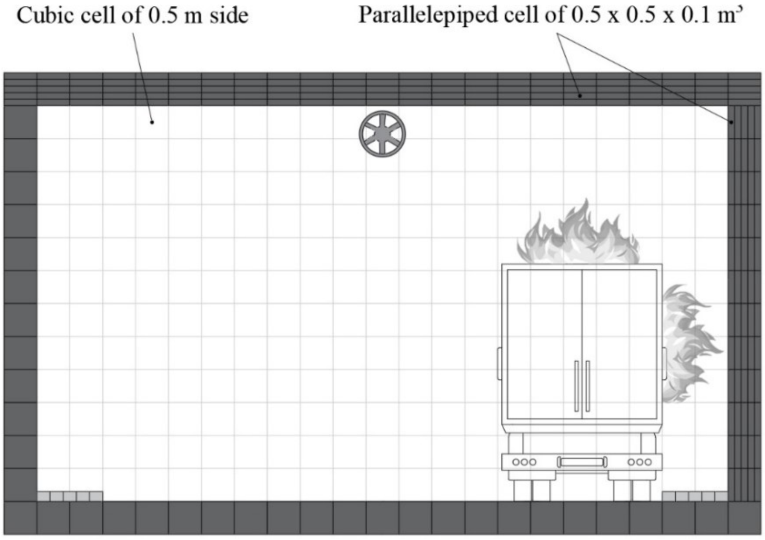

Fig. 3.10. Optimal mesh resolution for a generic cross-section.

It is also to be stressed that these simulations are performed for 120 min.

3.5. Developed 3D CFD model for simulating fire-induced spalling

Nowadays, as mentioned above, fire-induced damage is generally evaluated by means of 1D and 2D models based on the Finite Element Method (FEM) technique. However, FEM codes present certain limitations that might be overcome by using Computational Fluid Dynamics (CFD) tools.

Despite the enormous potential of CFD modeling to reproduce a vast range of fire scenarios, including those occurring in road tunnels, it has so far been little applied to evaluate spalling. In the light of the above considerations, one of the main reasons for justifying the present thesis is to develop a new 3D CFD model capable of simulating fire-induced damage in a road tunnel.

3.5.1. Assumptions

In the FDS code, spalling might be modeled as a reaction that consumes energy but does not generate any product because the concrete is supposed to have either fallen off the surface in chunks or pulverized powder (*McGrattan et al., 2019a*).

In the present thesis, therefore, it is assumed that spalling occurs as a consequence of the decomposition of calcium carbonate, which is an endothermic reaction that leads to the degradation of concrete.

The main parameters for the implementation of the proposed 3D FDS model are:

- Heat of reaction;
- Heating rate;
- Reference temperature (T_{ref}).

It is to be stressed that the roughness of the concrete surfaces was neglected.

Fig. 3.11 shows a view of the developed 3D FDS model with the schematic representation of concrete detachment from the ceiling.

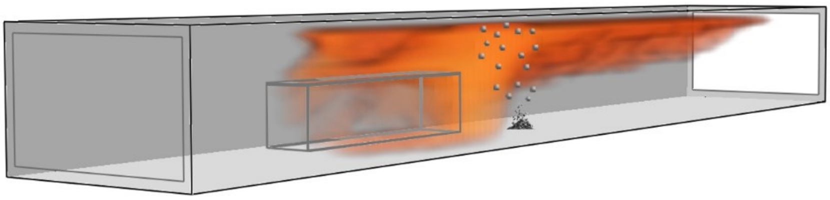

Fig. 3.11. View of the developed 3D FDS model with the schematic representation of concrete detachment from the ceiling.

3.5.1.1. Heat of reaction

The heat of reaction represents the enthalpy difference between the products and the reactants. In other terms, the amount of energy consumed, per unit mass of reactant that is transformed into the reaction products, is defined through the heat of reaction.

The heat of reaction corresponding to the decomposition of calcium carbonate is assumed to be equal to 1778.45 kJ/kg (*Sanders and Gallagher, 2002*; *Rodriguez-Navarro et al., 2009*; *André and Abanades, 2017*). It is to be stressed that a positive value of this parameter denotes an endothermic reaction (i.e., a reaction that subtracts energy from the system).

3.5.1.2. Heating rate

The heating rate is the rate at which the temperature of the concrete is increased. It can have effects not only on the occurrence of spalling but also on the spalling mode of the concrete.

In this thesis, the heating rate of the concrete is assumed to be constant and equal to 5 °C/min (*Phan and Carino, 2002*; *Trník et al., 2015*), which is also the default value in the FDS code.

3.5.1.3. Reference temperature

For each reaction that each material component undergoes, the kinetic parameters A_{pre} and E of the reaction rate must be specified. Specifically, A_{pre} [1/s] is the pre-exponential factor, while E [J/mol] is the activation energy. However, the kinetic parameters have meaning only when both are obtained from a common set of experiments such as ThermoGravimetric Analysis (TGA). Since A_{pre} and E parameters are not available for most real materials, the FDS code is able to automatically calculate their actual values by setting other parameters, of which the most important is the reference temperature. It is to be said that A_{pre} and E parameters do not need to be specified once the reference temperature is set (*McGrattan et al., 2019a*).

The reference temperature is defined as that value of the temperature at which the mass fraction of the material reduces to its maximum rate.

In the present thesis, the reference temperature is assumed to be equivalent to the critical temperature (i.e., the temperature above which spalling might occur). This means that spalling should take place when the concrete surfaces reach a temperature close to the reference one. On this basis and since fire-induced damage is assessed according to a temperature-based criterion, the use of the reference temperature appears to be more suitable and immediate for modeling spalling damage than that of the A_{pre} and E parameters, for which it would have been difficult to derive values as a function of the critical temperature.

Since there is no shared value of the critical temperature, which can be in the wide temperature range of 250-700 °C, a parametric analysis is also carried out in order to better assess the influence of the reference temperature (or critical temperature) on the severity of spalling damage. For this purpose, the reference temperature (T_{ref}) is set to:

- 380 °C;
- 500 °C;
- 600 °C;
- 700 °C.

With reference to the minimum value assumed for T_{ref}, in particular, it is usually accepted that spalling occurs for temperatures of at least 380 °C (*ITA, 2004*).

3.5.1.4. Initial and boundary conditions

In ordinary traffic conditions, a pressure difference of 5 Pa between tunnel portals is set as an initial condition in order to simulate an average natural ventilation of about 0.5 m/s due to the piston effect of moving vehicles (*Caliendo et al., 2021a*). In the event of a fire emergency, instead, the activation of all jet fans after 2 min from the fire start provides an average airflow velocity along the tunnel of about 5 m/s. Each jet fan is modeled as a parallelepiped solid with a length of 2 m, a width of 0.62 m, and a height of 0.62 m (i.e., the area of 0.62 x 0.62 m^2 of its boundary surfaces is equivalent to that of a circle with a diameter of 0.7 m), having the outlet surface supplying an airflow of 30 m/s.

The fire source is schematized as a parallelepiped solid, of which all surfaces burn. In contrast, the vehicles in the queue are modeled as non-flammable parallelepiped solids.

A non-slip condition is applied to the walls, which are considered non-adiabatic. The surfaces of the tunnel portals are assumed to be open to the outside. The initial ambient temperature is assumed to be 20 °C.

All the above-mentioned initial and boundary conditions are also applied with respect to the 65 m long portion of the entire tunnel used to evaluate spalling, except for the ventilation conditions. In this respect, a longitudinal ventilation with an average airflow velocity of 0.5 m/s within the first 2 min from the fire start and 5 m/s for the remaining simulation time is set as a boundary condition. Given their location, there are neither jet fans nor queued vehicles in the 65 m long tunnel portion used for assessing fire-induced damage.

It is to be stressed that, in order to verify that this 65 m long tunnel portion is actually representative of the entire tunnel (1 km long), the maximum concrete surface temperature profiles predicted for both the entire tunnel and its portion are compared. In this respect, Fig. 3.12 shows the maximum concrete surface temperature profiles predicted beneath the ceiling for both the entire tunnel (1 km long) and its portion (65 m long).

From Fig. 3.12 one can see that the predicted maximum concrete surface temperature profiles are quite similar to each other, with differences slightly more evident for temperatures below 380 ºC (i.e., the minimum value selected for the reference temperature). In light of this, the author is confident that the initial and boundary conditions applied to the tunnel portion make it well representative of the entire tunnel.

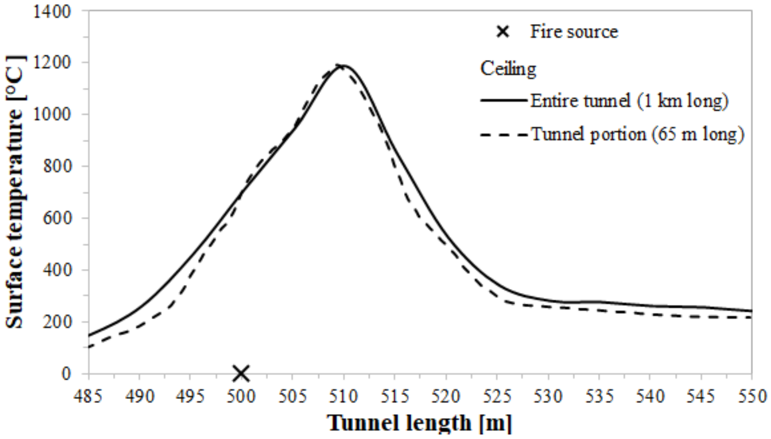

Fig. 3.12. Maximum concrete surface temperature profiles predicted beneath the ceiling for both the entire tunnel (1 km long) and its portion (65 m long).

3.6. Analysis and discussion of results

The fire-induced damage is evaluated with respect to a 65 m long portion of the entire tunnel investigated. This portion includes 15 m upstream and 50 m downstream of the center of the burning vehicle, which consists of a HGV located close to the right sidewalk. On this basis, the concrete elements most susceptible to spalling are the ceiling and the right wall, which, given the position of the fire source, are closer to the burning vehicle than the left wall.

In addition, it is to be said that the severity of spalling damage increases as the time of exposure to high temperatures increases. This means that the most serious fire-induced damage is expected at the end of the simulation time (i.e., after 120 min from the fire start).

Therefore, the following results will concern the evaluation of spalling affecting both the ceiling and the right wall of the investigated tunnel portion, and will refer to a time t = 120 min from the fire start.

In the light of the above considerations, the first step was to validate the developed 3D CFD model; subsequently, on the basis of the validated model, the main results provided by it were presented and discussed.

3.6.1. Validation

As mentioned above, the reference temperature is the temperature at which the mass fraction of the concrete reduces to its maximum rate. This means that spalling might also start at a concrete surface temperature slightly lower than the reference temperature. In this thesis, however, the reference temperature was assumed to be the temperature at which spalling occurs. As a result, the first step is to verify that the above-mentioned assumption is satisfied. In this respect, although the results showed that fire-induced damage started when the concrete surface temperature was slightly below the reference temperature (T_{ref}), the spalling depth was found to be lower than 0.005 m, and hence negligible, for $T < T_{ref}$. Therefore, the above-mentioned assumption can be considered fulfilled. In the light of the above considerations, it is also to be stressed that in the present thesis spalling is assumed to occur only where (and when) fire-induced damage affects the concrete for a depth of at least 0.005 m.

Once the above-mentioned assumption was verified, the proposed model was validated in order to test its capability of reproducing fire-induced damage. For this aim, the results, expressed in terms of maximum spalling depth, obtained from the developed 3D CFD model were compared with those provided by a competing model present in the international literature.

Qiao et al. (2019), by means of a 2D unsteady-state thermo-mechanical model, evaluated the spalling affecting the concrete lining of a tunnel subjected to long-duration fire using both a temperature-based criterion and a residual stress-based criterion. With reference to the temperature-based criterion, in particular, the authors assumed that spalling occurs when the concrete lining temperature reaches the critical temperature of 600 °C. On this basis, they found that the ratio between the damage depth and the lining thickness at the peak temperature of 1200 °C was about 20% after 120 min from the fire start, which means that if the thickness of the concrete element is 0.5 m as in the investigated case, the spalling depth will be about 0.1 m.

Instead, the results obtained from the developed 3D CFD model, which will be discussed in detail in the next Sections, showed that the maximum concrete surface temperature predicted beneath the ceiling was about 1200 °C after 120 min from the fire start. On this basis and considering T_{ref} = 600 °C, the maximum spalling depth was found to be about 0.096 m.

In the light of the above considerations, the results obtained from the developed 3D CFD model have a good level of conformity (an error of no more than 5%) with those provided by the model proposed by *Qiao et al. (2019)*. Specifically, the differences between the results obtained from the two above-mentioned models might be more especially attributable to the application of different modeling (3D vs 2D), as well as the use of different values for thermal conductivity, specific heat, and density of the concrete elements. Therefore, the author is confident that the developed 3D CFD model offers a realistic representation of fire-induced damage in a road tunnel.

3.6.2. Results obtained from the developed 3D CFD model

3.6.2.1. Cross-section profiles

The maximum spalling depths beneath the ceiling and along the right wall are measured at points A and B, respectively.

Point A is located at a distance (w) of 1.25 m from the right wall and at 9.25 m downstream of the fire center; while point B is placed at a distance (h) of 0.25 m from the road pavement and at 4.75 m downstream of the center of the burning vehicle.

Fig. 3.13 shows the locations of points A and B where the maximum spalling depths are predicted beneath the ceiling and along the right wall, respectively.

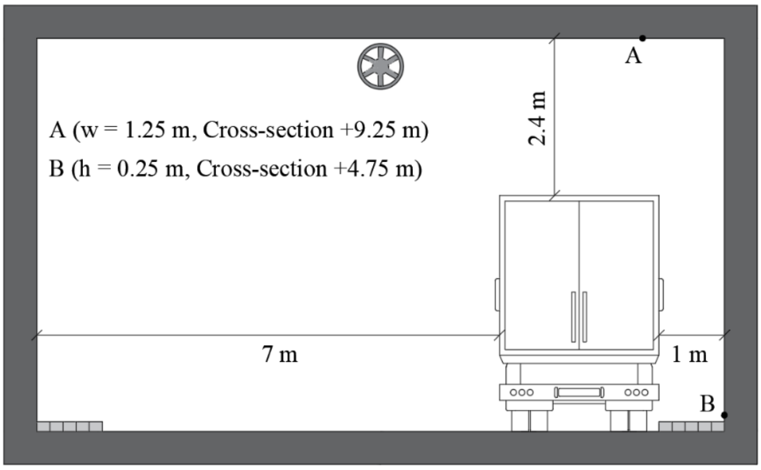

Fig. 3.13. Locations of points A and B where the maximum spalling depths are predicted beneath the ceiling and along the right wall, respectively.

3.6.2.1.1. Ceiling

The results are referred to the cross-section located at 9.25 m downstream of the fire center where the peak spalling depth beneath the ceiling was measured.

Fig. 3.14 shows the spalling depth profiles predicted beneath the ceiling as a function of the reference temperature.

From Fig. 3.14 one can see that the predicted spalling depths varied significantly with the reference temperature, reaching the highest values for T_{ref} = 380 °C and the lowest values for T_{ref} = 700 °C. The most severe fire-induced damage is observed in the region close to the burning vehicle (i.e., $0 < w < 4$ m), with a peak at point A of 0.168 m, 0.123 m, 0.096 m, and 0.079 m for reference temperatures of 380 °C, 500 °C, 600 °C, and 700 °C, respectively. Therefore, the maximum spalling depth increased by about 53% passing from T_{ref} = 700 °C to T_{ref} = 380 °C.

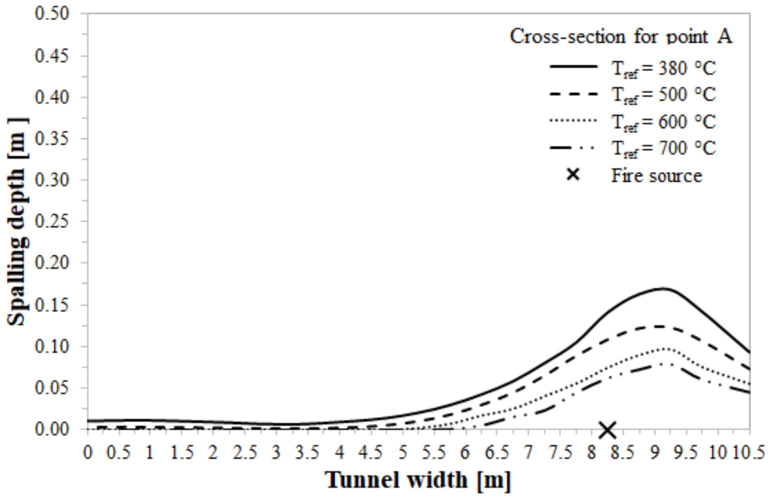

Fig. 3.14. Cross-section for point A. Spalling depth profiles predicted beneath the ceiling as a function of the reference temperature; t = 120 min.

From Fig. 3.14 it is also possible to observe that spalling affected the ceiling throughout its width (i.e., $0 < w < 10.5$ m) for the reference temperature of 380 °C, while it is more or less localized in the area occupied by the burning vehicle (i.e., $0 < w < 5.25$ m) when the reference temperature is set equal to 500 °C, 600 °C, and 700 °C.

The severity of spalling damage depends more especially on the temperatures and heating rate to which concrete surfaces are subjected. On this basis, the above-mentioned spalling depth profiles might be analyzed using the corresponding concrete surface temperature profile.

Fig. 3.15 shows the concrete surface temperature profile predicted beneath the ceiling in the absence of spalling. In this respect, it is to be said that assuming the reference temperature as the temperature at which fire-induced damage occurs, the maximum temperature attainable by the concrete before detaching and falling on the road pavement is equal to the reference temperature. This means that certain information such as the maximum concrete surface temperature corresponding to the investigated fire scenario and the location of the point where it is reached, useful for analyzing the spalling depth profiles, can only be obtained by using a model in which spalling is not taken into account, namely by performing a conventional heat transfer analysis.

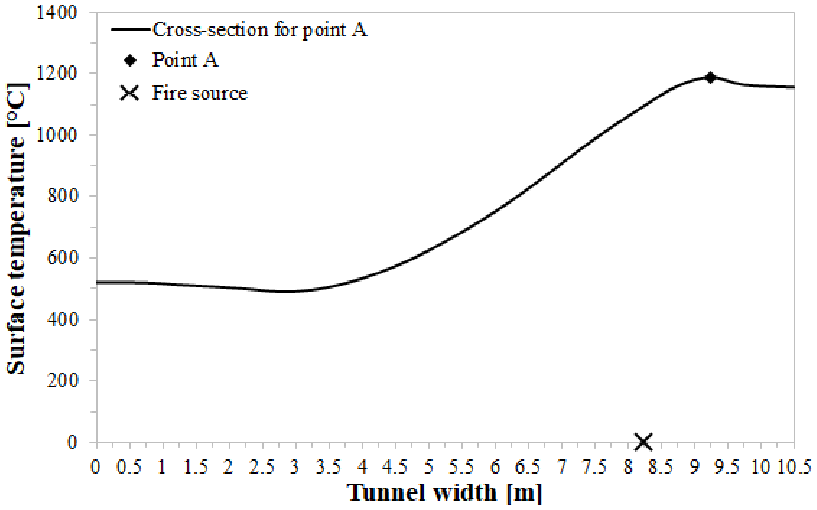

Fig. 3.15. Cross-section for point A. Concrete surface temperature profile predicted beneath the ceiling in the absence of spalling; t = 120 min.

From Fig. 3.15 one can see that the concrete surface temperature profile predicted beneath the ceiling in the absence of spalling is consistent with the spalling depth profiles reported in Fig. 3.14. Specifically, the maximum concrete surface temperature of about 1200 °C is reached at point A where the maximum spalling depth was also measured. In addition, Fig. 3.15 shows that the temperatures beneath the ceiling are always higher than 380 °C, with values above 500-600 °C in the region close to the fire source (i.e., $0 < w < 5.25$ m).

Fig. 3.16 shows the concrete surface temperature profiles predicted beneath the ceiling at the time when $T = T_{ref}$ as a function of the reference temperature.

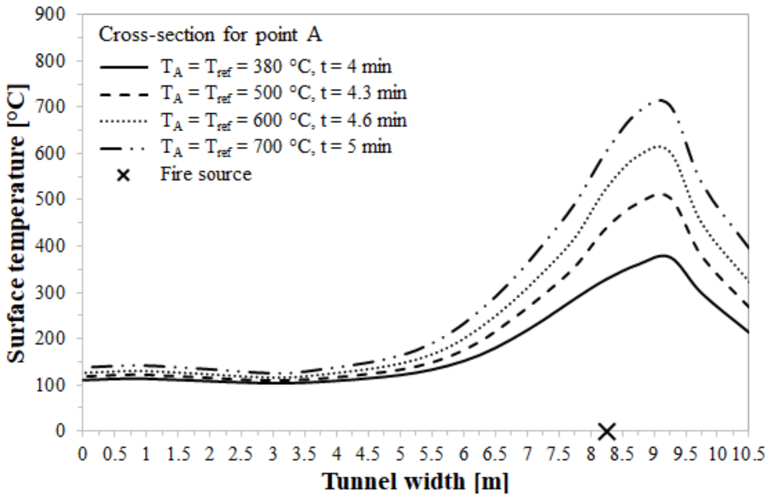

Fig. 3.16. Cross-section for point A. Concrete surface temperature profiles predicted beneath the ceiling at the time when $T = T_{ref}$ as a function of the reference temperature.

From Fig. 3.16 it is possible to observe that the temperatures beneath the ceiling surface increased faster in the area occupied by the burning vehicle (i.e., $0 < w < 5.25$ m), with a peak at point A. This means that fire-induced damage started at point A where the temperature (T_A) reached the reference one quicker than at other points located beneath the ceiling. At this point, in particular, the time required to reach a spalling depth of 0.005 m (the *spalling start time* for brevity) is approximately 9.1 min, 9.4 min, 9.9 min, and 11.1 min from the fire start for reference temperatures of 380 °C, 500 °C, 600 °C, and 700 °C, respectively. On this basis, the spalling start time increased by about 18% passing from T_{ref} = 380 °C to T_{ref} = 700 °C. In this respect, it is worth remembering that in the present thesis spalling is assumed to occur only where (and when) fire-induced damage affects the concrete for a depth of at least 0.005 m.

Therefore, the fact that the peak concrete surface temperature is measured at point A, as well as that the temperature predicted at this point reached the reference one (i.e., the temperature at which spalling occurs in the proposed 3D CFD model) faster than at other points, might be the reasons why the maximum spalling depth beneath the ceiling occurred at point A. In addition, the fact that the most severe fire-induced damage predicted beneath the ceiling is more or less localized in the region close to the fire source might be due to the highest concrete surface temperatures observed in this area, which is also characterized by a quicker increase in the cited temperatures.

3.6.2.1.2. Right wall

The results are related to the cross-section located at 4.75 m downstream of the center of the burning vehicle where the maximum spalling depth along the right wall was measured.

Fig. 3.17 shows the spalling depth profiles predicted along the right wall as a function of the reference temperature.

From Fig. 3.17 it is possible to observe that also along the right wall the predicted spalling depth changed considerably with the reference temperature, reaching the highest values for T_{ref} = 380 °C and the lowest values for T_{ref} = 700 °C. The most severe fire-induced damage is measured at the foot of the right wall (i.e., 0 < h < 1 m), with a peak at point B of 0.312 m, 0.29 m, 0.269 m, and 0.239 m for reference temperatures of 380 °C, 500 °C, 600 °C, and 700 °C, respectively. On this basis, the maximum spalling depth increased by about 23% passing from the highest reference temperature (T_{ref} = 700 °C) to the lowest one (T_{ref} = 380 °C).

From Fig. 3.17 one can also see that spalling always affected the right wall throughout its height (i.e., 0 < h < 6 m), regardless of the reference temperature value.

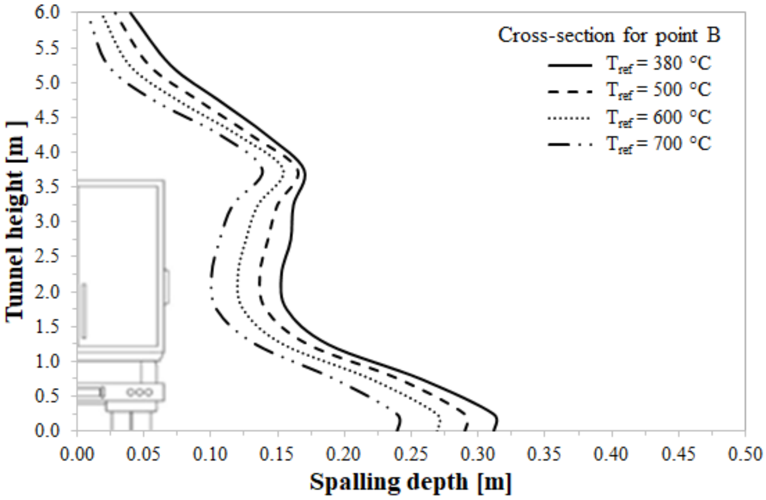

Fig. 3.17. Cross-section for point B. Spalling depth profiles predicted along the right wall as a function of the reference temperature; t = 120 min.

Fig. 3.18 shows the concrete surface temperature profile predicted along the right wall in the absence of spalling.

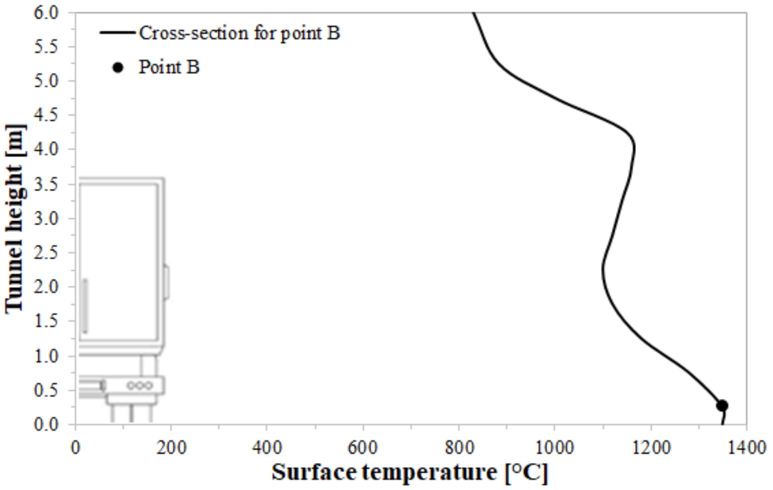

Fig. 3.18. Cross-section for point B. Concrete surface temperature profile predicted along the right wall in the absence of spalling; t = 120 min.

From Fig. 3.18 it is possible to observe that the concrete surface temperature profile predicted along the right wall in the absence of spalling is consistent with the spalling depth profiles reported in Fig. 3.17. In particular, the peak concrete surface temperature of about 1350 °C is reached at point B where the most severe fire-induced damage also occurred. Moreover, Fig. 3.18 shows that the temperatures along the right wall are always above 700 °C (i.e., $0 < h < 6$ m).

Fig. 3.19 reports the concrete surface temperature profiles predicted along the right wall at the time when $T = T_{ref}$ as a function of the reference temperature.

From Fig. 3.19 one can see that the temperatures along the right wall surface increased faster at the foot of the wall (i.e., $0 < h < 1$ m), with a peak at point B. This means that spalling started at point B where the temperature (T_B) reached the reference one quicker than at other points located along the right wall. At this point, in particular, the spalling start time is about 5.3 min, 6.2

min, 6.6 min, and 7.6 min from the fire start for reference temperatures of 380 °C, 500 °C, 600 °C, and 700 °C, respectively. As a result, the time required to reach a spalling depth of 0.005 m increased by approximately 30% passing from T_{ref} = 380 °C to T_{ref} = 700 °C.

Therefore, the fact that the peak concrete surface temperature is measured at point B, as well as that the temperature predicted at this point reached the reference one faster than at other points, might explain why the maximum spalling depth along the right wall occurred at point B. Moreover, the fact that the most severe fire-induced damage predicted along the right wall is localized at the foot of the wall might be due to the highest concrete surface temperatures observed in this region, which is also characterized by a quicker increase in the cited temperatures.

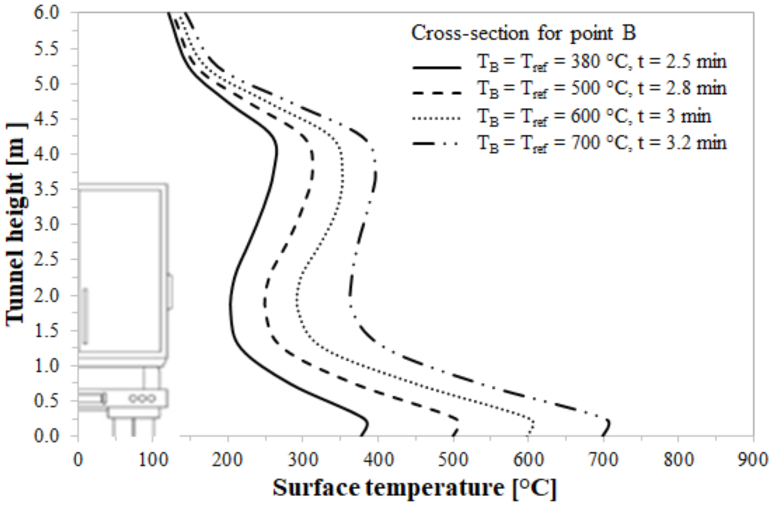

Fig. 3.19. Cross-section for point B. Concrete surface temperature profiles predicted along the right wall at the time when $T = T_{ref}$ as a function of the reference temperature.

Summing up, since the right wall is the closest concrete element to the burning vehicle (see Fig. 3.13), the highest concrete surface temperatures were predicted along it, which was also characterized by the fastest increase of the cited temperatures. These might be the reasons why: (i) the maximum spalling depth occurred along the right wall; (ii) spalling started earlier at point B located on the right wall than at point A placed beneath the ceiling; (iii) spalling affected the right wall throughout its height not only for the reference temperature of 380 °C as beneath the ceiling.

3.6.2.2. Longitudinal profiles

3.6.2.2.1. Ceiling

The results are referred to the longitudinal section passing through point A where the peak spalling depth beneath the ceiling was measured.

Fig. 3.20 shows the spalling depth profiles predicted beneath the ceiling as a function of the reference temperature.

From Fig. 3.20 it is possible to observe that the length of the tunnel affected by a spalling depth of at least 0.005 m (the *spalling length* for brevity) varied significantly with the reference temperature, reaching the highest value for T_{ref} = 380 °C and the lowest value for T_{ref} = 700 °C. In particular, the spalling affected the tunnel ceiling for a length of about 22.5 m, 19 m, 16 m, and 12.5 m for reference temperatures of 380 °C, 500 °C, 600 °C, and 700 °C, respectively. On this basis, the spalling length increased by about 44% passing from T_{ref} = 700 °C to T_{ref} = 380 °C.

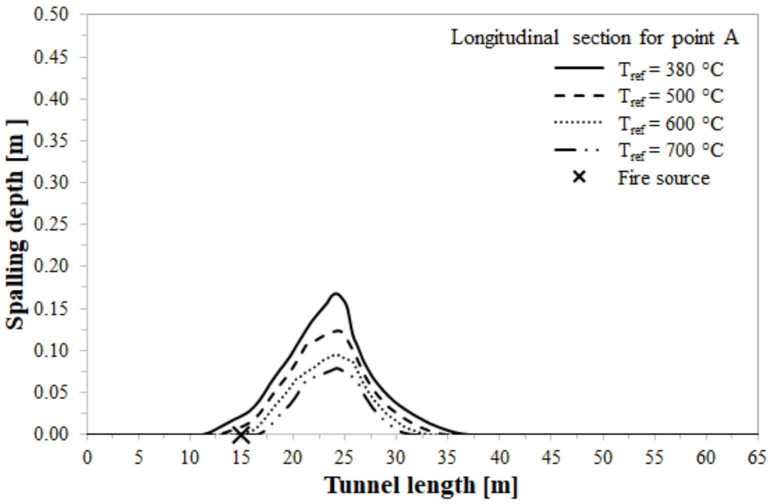

Fig. 3.20. Longitudinal section for point A. Spalling depth profiles predicted beneath the ceiling as a function of the reference temperature; t = 120 min.

From Fig. 3.20 one can also see that spalling affected more especially the ceiling portion downstream of the fire center. In fact, it extended up to about 20 m, 18 m, 16 m, and 12.5 m downstream from the center of the burning vehicle for reference temperatures of 380 °C, 500 °C, 600 °C, and 700 °C, respectively.

Fig. 3.21 shows the concrete surface temperature profile predicted beneath the ceiling in the absence of spalling.

From Fig. 3.21 it is possible to observe that the concrete surface temperature profile predicted beneath the ceiling in the absence of spalling is consistent with the spalling depth profiles reported in Fig. 3.20. Specifically, Fig. 3.21 shows that the highest concrete surface temperatures are reached downstream of the fire center. This might be due to the presence of longitudinal ventilation that pushes the hot gases towards the tunnel exit portal.

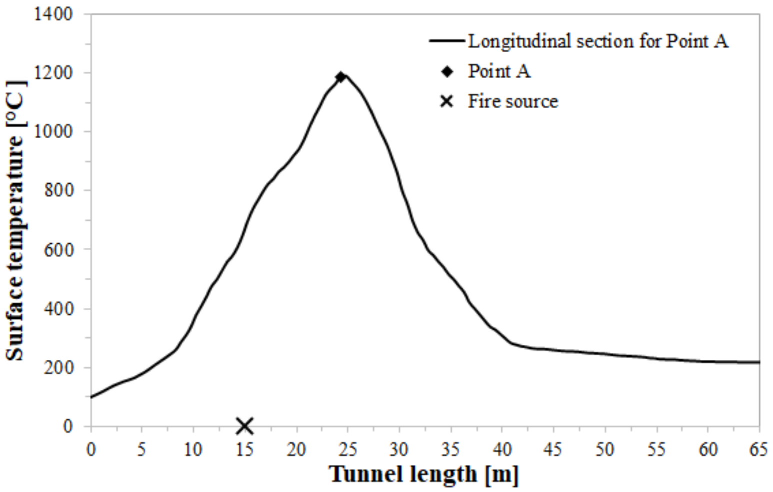

Fig. 3.21. Longitudinal section for point A. Concrete surface temperature profile predicted beneath the ceiling in absence of the spalling; t = 120 min.

Therefore, the fact that the highest concrete surface temperatures are measured downstream of the center of the burning vehicle might be the reason why the most severe fire-induced damage predicted beneath the ceiling is observed in this tunnel region.

The spalled concrete area predicted beneath the ceiling also changed considerably with the reference temperature, reaching the maximum value for T_{ref} = 380 °C and the minimum value for T_{ref} = 700 °C. In particular, it is about 304 m^2, 284 m^2, 259 m^2, and 176 m^2 for reference temperatures of 380 °C, 500 °C, 600 °C, and 700 °C, respectively. On this basis, the spalled concrete area increased by approximately 42% passing from T_{ref} = 700 °C to T_{ref} = 380 °C.

The corresponding spalling amount is about 8 m^3, 5 m^3, 3.2 m^3, and 2 m^3 for reference temperatures of 380 °C, 500 °C, 600 °C, and 700 °C, respectively. Therefore, it increased by about

75% passing from the highest reference temperature (T_{ref} = 700 °C) to the lowest one (T_{ref} = 380 °C).

3.6.2.2.2. Right wall

The results are related to the longitudinal section passing through point B where the maximum spalling depth along the right wall was measured.

Fig. 3.22 shows the spalling depth profiles predicted along the right wall as a function of the reference temperature.

From Fig. 3.22 one can see that also along the right wall the spalling length changed considerably with the reference temperature, reaching the maximum value for T_{ref} = 380 °C and the minimum value for T_{ref} = 700 °C. In this regard, the spalling affected the right wall for a length of about 14 m, 11.5 m, 10.5 m, and 9 m for reference temperatures of 380 °C, 500 °C, 600 °C, and 700 °C, respectively. As a result, the length of the tunnel portion affected by a spalling depth of at least 0.005 m increased by approximately 36% passing from T_{ref} = 700 °C to T_{ref} = 380 °C.

From Fig. 3.22 it is also possible to observe that spalling affected more especially the part of the right wall downstream of the fire center. In fact, it extended up to about 12 m, 10.5 m, 10.5 m, and 9 m downstream of the center of the burning vehicle for reference temperatures of 380 °C, 500 °C, 600 °C, and 700 °C, respectively.

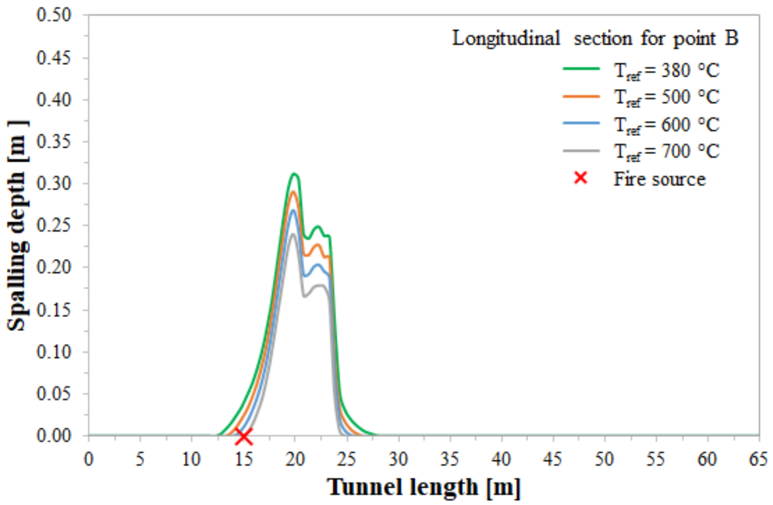

Fig. 3.22. Longitudinal section for point B. Spalling depth profiles predicted along the right wall as a function of the reference temperature; t = 120 min.

Fig. 3.23 shows the concrete surface temperature profile predicted along the right wall in the absence of spalling.

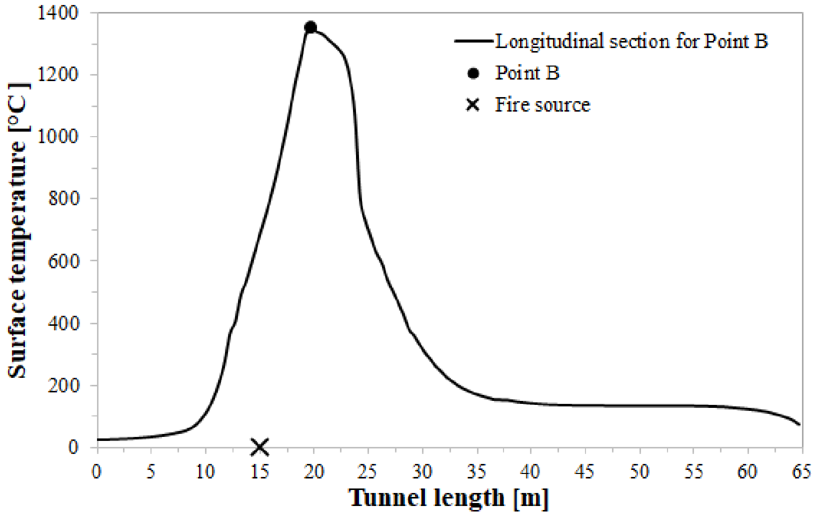

Fig. 3.23. Longitudinal section for point B. Concrete surface temperature profile predicted along the right wall in the absence of spalling; t = 120 min.

From Fig. 3.23 one can see that the concrete surface temperature profile predicted along the right wall in the absence of spalling is consistent with the spalling depth profiles reported in Fig. 3.22. In particular, Fig. 3.23 shows that the highest concrete surface temperatures are reached downstream of the center of the burning vehicle. This might still be due to the presence of longitudinal ventilation that pushes the hot gases towards the tunnel exit portal.

Therefore, the fact that the highest concrete surface temperatures are measured downstream of the fire center might be the reason why the greatest fire-induced damage predicted along the right wall is observed in this tunnel region.

The spalled concrete area predicted along the right wall also varied significantly with the reference temperature, reaching the highest value for T_{ref} = 380 °C and the lowest value for T_{ref} = 700 °C. Specifically, it is about 128.5 m^2, 115 m^2, 101 m^2, and 87.5 m^2 for reference temperatures of 380 °C, 500 °C, 600 °C, and 700 °C, respectively. Consequently, the spalled concrete area increased by approximately 32% passing from T_{ref} = 700 °C to T_{ref} = 380 °C.

The corresponding spalling amount is about 9.5 m^3, 8 m^3, 7 m^3, and 5.7 m^3 for reference temperatures of 380 °C, 500 °C, 600 °C, and 700 °C, respectively. On this basis, it increased by approximately 40% passing from the highest reference temperature (T_{ref} = 700 °C) to the lowest one (T_{ref} = 380 °C).

Further considerations might be made using the longitudinal ventilation velocity profiles along the tunnel length. For this aim, Fig. 3.24 shows the above-mentioned profiles passing through points A and B.

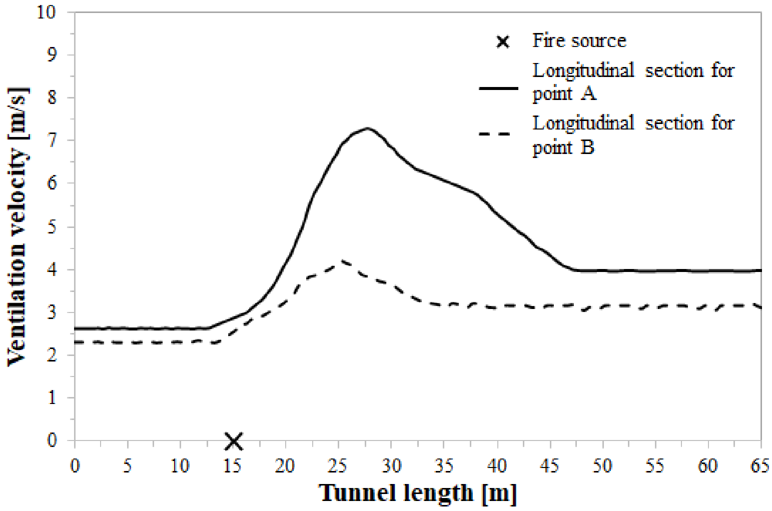

Fig. 3.24. Profiles passing through points A and B of the longitudinal ventilation velocity along the tunnel length.

From Fig. 3.24 it is possible to observe that the longitudinal ventilation velocities are higher downstream of the fire center, with maximum values measured beneath the ceiling. This means that hot gases are pushed downstream of the fire center by the longitudinal ventilation, reaching the longest distances beneath the ceiling. In the light of the above considerations and since the ventilation also tends to cool hot gases, the concrete surface temperatures were found to be on average higher beneath the ceiling (Fig. 3.21), but their maximum values were measured along the right wall in the region localized more or less close to the fire source (Fig. 3.23). Specifically, the fact that the concrete surface temperatures beneath the ceiling were found to be on average higher than along the right wall might be the reason why both the greatest spalling length and the maximum spalled concrete area were predicted beneath the ceiling. On the contrary, the fact that the highest concrete surface temperatures were measured on the right wall might explain why both the maximum spalling depth and the greatest spalling amount were observed along it.

It is also to be stressed that the highest values of the longitudinal ventilation velocity along the right wall are found close to the ceiling. This means, on the basis of the above considerations, that the maximum spalling length on the right wall is measured along a longitudinal section passing not through point B but through a point near the top of the wall. On the contrary, the maximum spalling length beneath the ceiling is measured for the longitudinal section passing right through point A.

It is also to be said that the fact that beneath the ceiling the longitudinal ventilation pushed the hot gases further downstream of the burning vehicle than along the right wall might be the reason why point A, where the maximum spalling depth was measured beneath the ceiling, is located at a longer distance (about 4.5 m) from the fire center than the corresponding point B along the right wall.

3.6.3. Comparison between the developed 3D CFD model and a heat transfer analysis

As mentioned above, the main difference between a conventional heat transfer analysis and the developed 3D CFD model is that the former does not consider spalling. As a result, the fire-induced damage obtained from a heat transfer analysis might be underestimated.

3.6.3.1. Ceiling

The results are always referred to point A where the peak spalling depth beneath the ceiling was measured.

Fig. 3.25 shows the temperature profiles within the thickness of the ceiling obtained from both a heat transfer analysis and the developed 3D CFD model.

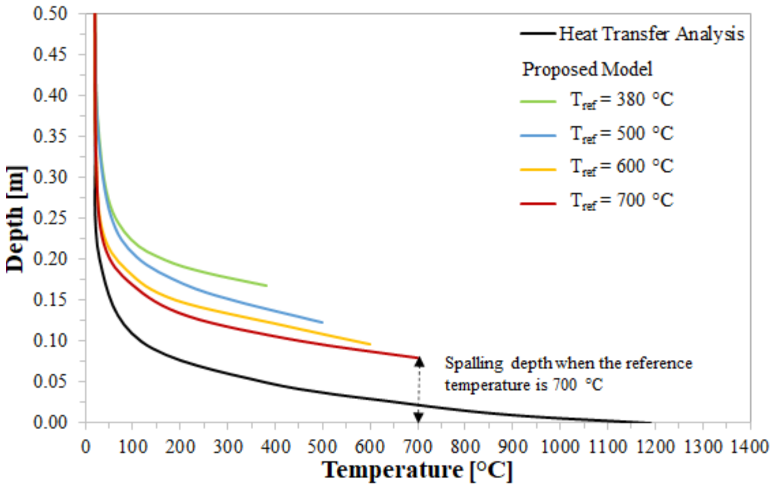

Fig. 3.25. Point A. Temperature profiles within the thickness of the ceiling obtained from both a heat transfer analysis and the developed 3D CFD model; t = 120 min.

From Fig. 3.25 one can see that the temperatures within the thickness of the ceiling obtained by performing a conventional heat transfer analysis are underestimated compared to those provided by the developed 3D CFD model. With a heat transfer analysis, in particular, temperatures above 380 °C (i.e., the minimum temperature above which spalling occurs in the developed 3D CFD model) are measured up to a depth of about 0.05 m from the heated surface. This means that spalling might at most affect the concrete up to this depth, which is much less than the maximum spalling depth measured using the proposed

3D CFD model (i.e., 0.168 m for T_{ref} = 380 °C, see Section 3.6.1). Therefore, as expected, conventional heat transfer analyses underestimate fire-induced damage compared to that measured using the developed 3D CFD model.

From Fig. 3.25 it is also possible to observe that the temperature within the concrete thickness decreases as the distance from the surface exposed to fire increases. Specifically, this temperature is close to the room temperature of 20 °C at a depth of about 0.3 m from the heated surface for all T_{ref} values.

It is to be stressed that not only the concrete but also the steel reinforcements can be seriously damaged by fire, more especially when spalling affects the concrete cover throughout its thickness (usually 0.05 m). In these circumstances, in fact, since the concrete cover no longer protects the steel reinforcement from fire, the steel rebars remain exposed to temperatures higher than the threshold value of 250 °C (*ITA, 2004*) and might, hence, suffer a significant reduction in both mechanical properties and elastic modulus. On this basis, it is very important to define the concrete area affected by a spalling depth of at least 0.05 m (i.e., the thickness of the concrete cover), as well as the time required to reach a spalling depth of 0.05 m.

The concrete area affected by a spalling depth of at least 0.05 m varied significantly with the reference temperature, reaching the highest value for T_{ref} = 380 °C and the lowest value for T_{ref} = 700 °C. Specifically, it is about 46 m^2, 31.5 m^2, 20 m^2, and 13.5 m^2 for reference temperatures of 380 °C, 500 °C, 600 °C, and 700 °C, respectively. Consequently, the concrete area affected by a spalling depth of at least 0.05 m increased by about 71% passing from T_{ref} = 700 °C to T_{ref} = 380 °C.

Similar results are obtained for the time required to reach a spalling depth of 0.05 m, which is about 38 min, 43 min, 49 min, and 57 min for reference temperatures of 380 °C, 500 °C, 600 °C, and 700 °C, respectively. On this basis, it increased by about 33% passing from the lowest reference temperature (T_{ref} = 380 °C) to the highest one (T_{ref} = 700 °C).

3.6.3.2. Right wall

The results are always related to point B at which the maximum spalling depth along the right wall was measured.

Fig. 3.26 shows the temperature profiles within the thickness of the right wall obtained from both a heat transfer analysis and the developed 3D CFD model.

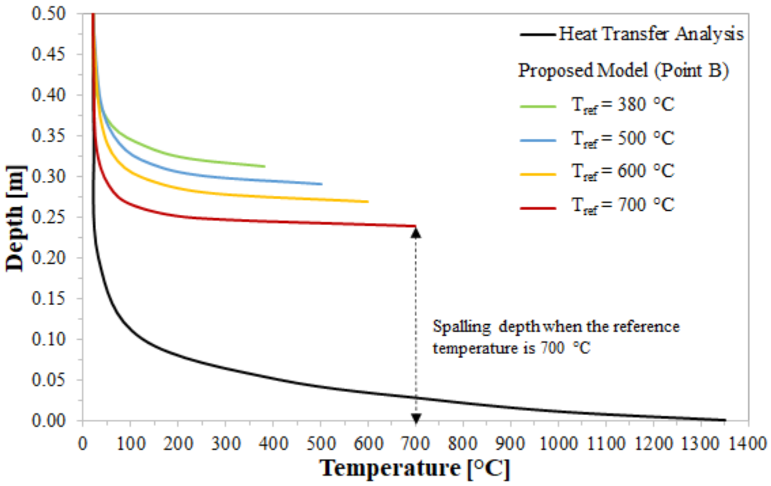

Fig. 3.26. Point B. Temperature profiles within the thickness of the right wall obtained from both a heat transfer analysis and the developed 3D CFD model; t = 120 min.

Fig. 3.26 confirms the results found beneath the ceiling, namely that a conventional heat transfer analysis underestimates fire-induced damage compared to that measured using the developed 3D CFD model. In fact, also along the right wall, with a heat transfer analysis, temperatures above 380 °C are measured up to a depth of about 0.06 m from the heated surface. As a result, the spalling might at most affect the concrete up to this depth, which is much less than the maximum spalling depth measured using the proposed 3D CFD model (i.e., 0.312 m for T_{ref} = 380 °C, see Section 3.6.1).

From Fig. 3.26 it is also possible to observe that the temperature within the concrete thickness decreases as the distance from the surface exposed to fire increases. In particular, this temperature is close to the ambient temperature of 20 °C at a depth of about 0.4 m from the heated surface for all T_{ref} values.

Also along the right wall, the concrete area affected by a spalling depth of at least 0.05 m changed considerably with the reference temperature, reaching the maximum value for T_{ref} = 380 °C and the minimum value for T_{ref} = 700 °C. Specifically, it is about 58 m^2, 52 m^2, 46 m^2, and 39 m^2 for reference temperatures of 380 °C, 500 °C, 600 °C, and 700 °C, respectively. As a result, the concrete area affected by a spalling depth of at least 0.05 m increased by approximately 33% passing from T_{ref} = 700 °C to T_{ref} = 380 °C.

Similar results are obtained for the time required to reach a spalling depth of 0.05 m, which is about 24 min, 26 min, 28 min, and 31 min for reference temperatures of 380 °C, 500 °C, 600 °C, and 700 °C, respectively. On this basis, it increased by about 23% passing from the lowest reference temperature (T_{ref} = 380 °C) to the highest one (T_{ref} = 700 °C).

Summing up, in the light of the above considerations, it is to be stressed that in order to reliably predict and evaluate the fire resistance of a tunnel subjected to a severe fire, it is appropriate to use a model such as the one proposed, namely a model that takes into account fire-induced damage. In fact, conventional heat transfer analyses underestimate spalling because they do not consider structural loss.

3.6.4. The influence of the reference temperature on the severity of spalling damage

A parametric analysis with respect to the reference temperature (i.e., 380 °C, 500 °C, 600 °C, and 700 °C) was also carried out in order to better evaluate the influence of this temperature on the severity of spalling damage. In this respect, the parametric analysis results are related to points A and B where the maximum spalling depths were measured beneath the ceiling and along the right wall, respectively.

Fig. 3.27 shows the influence of the reference temperature on certain variables such as the maximum spalling depth, the spalling start time, the spalling length, the spalled concrete area, the spalling amount, the concrete area affected by a spalling depth of at least 0.05 m, and the time required to reach a spalling depth of 0.05 m.

The results obtained from this parametric analysis showed that: (i) the maximum spalling depth decreases as the reference temperature increases according to an exponential law beneath the ceiling and a linear law along the right wall (Fig. 3.27a); (ii) the spalling start time (i.e., the time required to reach a spalling depth of 0.005 m) tends to increase exponentially as T_{ref} increases with reference to both the ceiling and the right wall (Fig. 3.27b); (iii) the spalling length (i.e., the length of the tunnel portion affected by a spalling depth of at least 0.005 m) decreases as the reference temperature increases following a linear law beneath the ceiling and an exponential law along the right wall (Fig. 3.27c); (iv) the spalled concrete area tends to decrease linearly as T_{ref} increases for both the ceiling and the right wall (Fig. 3.27d); (v) the spalling amount decreases as the reference temperature increases according to a logarithmic law beneath the ceiling and a linear law along the right wall (Fig. 3.27e); (vi) the concrete area affected by a spalling depth of at least 0.05 m decreases as the reference temperature increases following a logarithmic law beneath the ceiling and a linear law along the right wall (Fig. 3.27f); (vii) the time to reach a spalling depth of 0.05 m grows exponentially with T_{ref} on both the ceiling and the right wall (Fig. 3.27g).

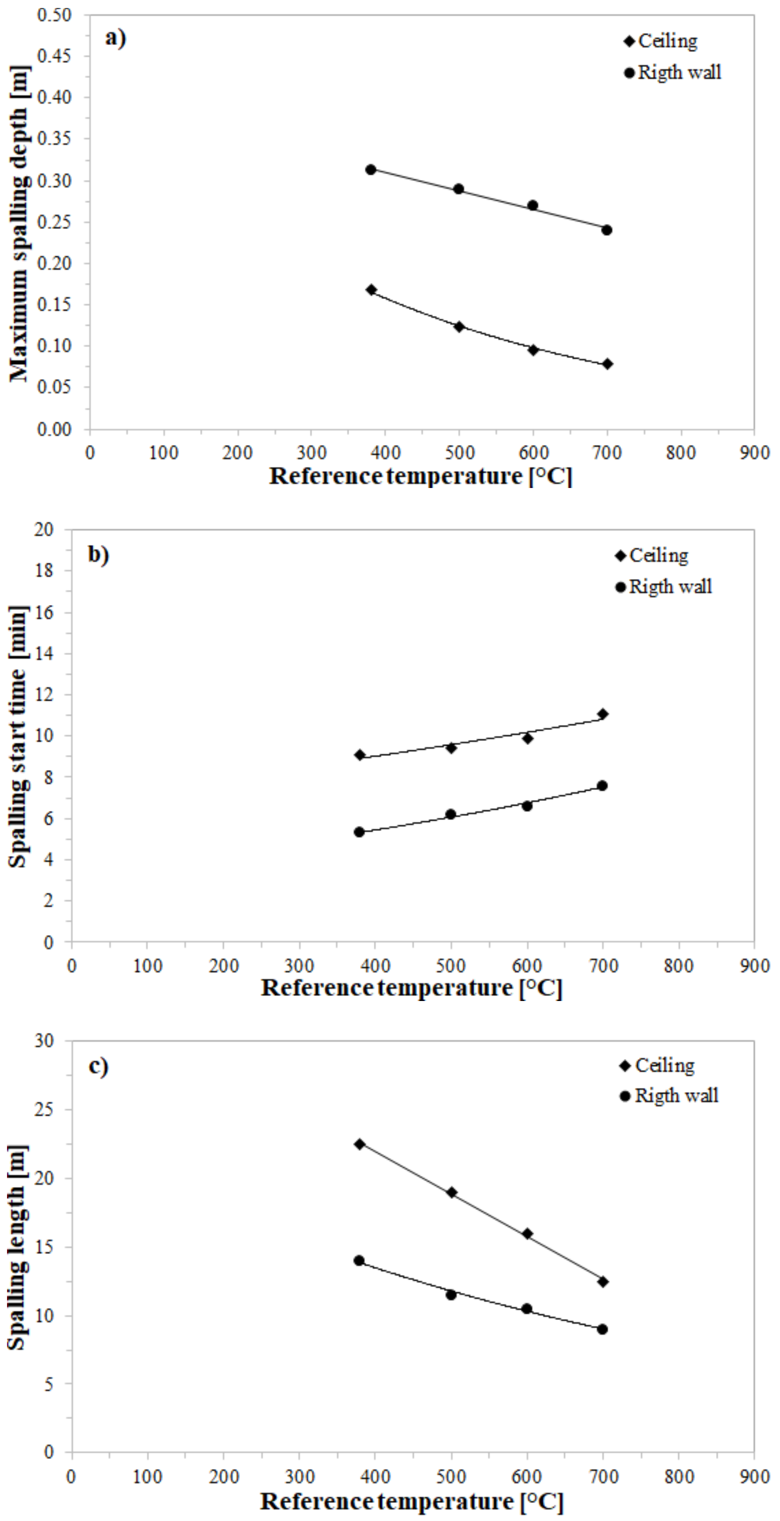
a)
Ceiling
Rigth wall
Maximum spalling depth [m]
0.00
0.05
0.10
0.15
0.20
0.25
0.30
0.35
0.40
0.45
0.50
Reference temperature [°C]
0
100
200
300
400
500
600
700
800
900
b)
Ceiling
Rigth wall
Spalling start time [min]
0
2
4
6
8
10
12
14
16
18
20
Reference temperature [°C]
0
100
200
300
400
500
600
700
800
900
c)
Ceiling
Rigth wall
Spalling length [m]
0
5
10
15
20
25
30
Reference temperature [°C]
0
100
200
300
400
500
600
700
800
900

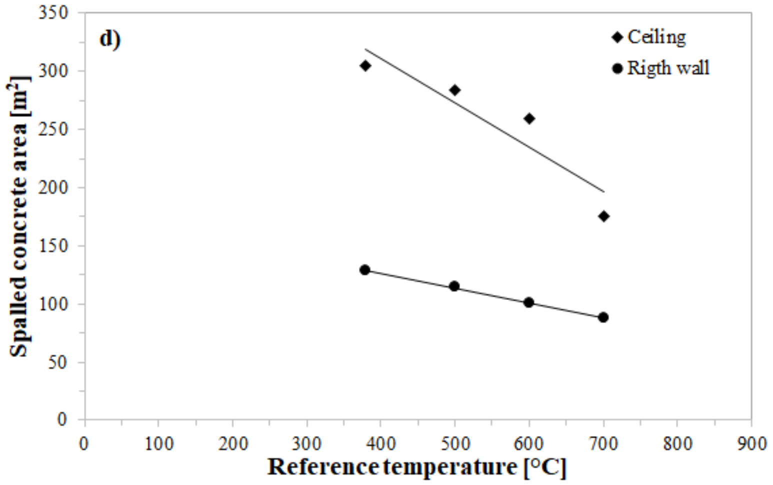
d)
Ceiling
Rigth wall
Spalled concrete area [m²]
0
50
100
150
200
250
300
350
0
100
200
300
400
500
600
700
800
900
Reference temperature [°C]

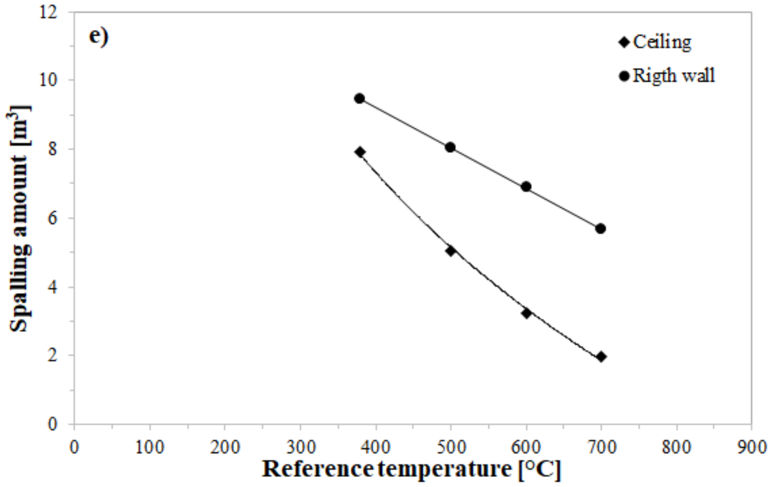
e)
Ceiling
Rigth wall
Spalling amount [m³]
0
2
4
6
8
10
12
0
100
200
300
400
500
600
700
800
900
Reference temperature [°C]

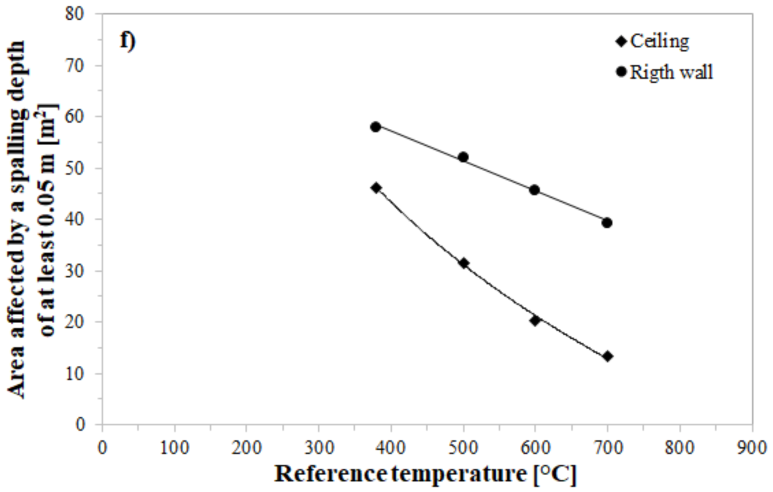
f)
Ceiling
Rigth wall
Area affected by a spalling depth of at least 0.05 m [m²]
0
10
20
30
40
50
60
70
80
0
100
200
300
400
500
600
700
800
900
Reference temperature [°C]

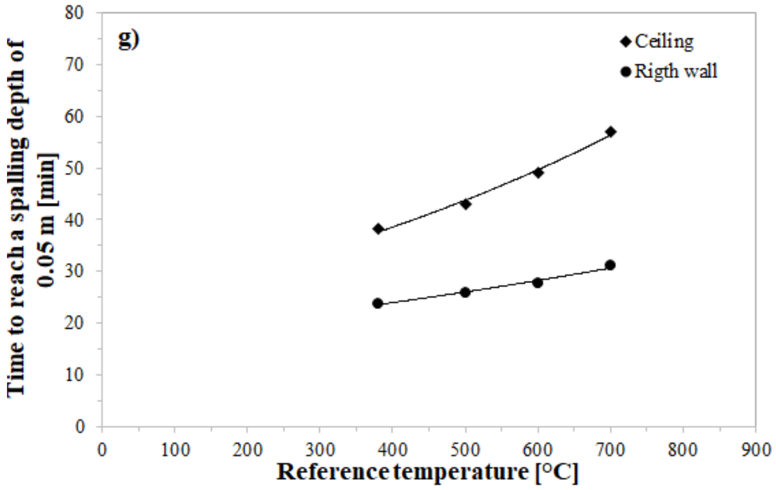

Fig. 3.27. Parametric analysis. Influence of the reference temperature on: a) maximum spalling depth; b) spalling start time; c) length of the tunnel portion affected by spalling; d) spalled concrete area; e) spalling amount; f) concrete area affected by a spalling depth of at least 0.05 m; g) time required to reach a spalling depth of 0.05 m; t = 120 min.

Table 3.1 shows the equations describing the relationships between the reference temperature (*X*) and all the above-mentioned variables (*Y*) for both the ceiling and the right wall, as well as the corresponding R^2.

From Table 3.1 it is possible to observe that all R^2 values are greater than 90%, except for the one associated with the spalled concrete area beneath the ceiling for which R^2 is 85.75%. In the light of these considerations, the author believes that the proposed fitted curves are able to well represent the influence of the reference temperature on the severity of spalling damage.

Table 3.1. Parametric analysis. Fitted curves and R^2 values.

Variable	Fitted curve		R^2	
	Ceiling	**Right wall**	**Ceiling**	**Right wall**
Maximum spalling depth [m]	$Y = 0.4082e^{-0.002X}$	$Y = -0.0002X + 0.3999$	0.997	0.9876
Spalling start time [min]	$Y = 7.0872e^{0.0006X}$	$Y = 3.5345e^{0.0011X}$	0.9024	0.9822
Spalling length [m]	$Y = -0.0311X + 34.44$	$Y = 23.056e^{-0.001X}$	0.9981	0.9893
Spalled concrete area [m^2]	$Y = -0.3813X + 463.84$	$Y = -0.1288X + 178.09$	0.8575	0.9981
Spalling amount [m^3]	$Y = -9.779ln(X) + 65.922$	$Y = -0.0118X + 13.95$	0.9975	0.9999
Area affected by a spalling depth of at least 0.05 m [m^2]	$Y = -54.48ln(X) + 369.8$	$Y = -0.0588X + 80.792$	0.9975	0.996
Time to reach a spalling depth of 0.05 m [min]	$Y = 23.304e^{0.0013X}$	$Y = 17.295e^{0.0008X}$	0.9914	0.9783

3.7. Conclusions

One of the scopes of this research was to develop a 3D CFD model able to evaluate fire-induced damage in a road tunnel. In this respect, the investigated fire scenario involved a HGV capable of developing a 100 MW fire. Specifically, the burning vehicle was located in the middle of the tunnel length and close to the right sidewalk. Given the position of the fire, the concrete elements most susceptible to spalling were the ceiling and the right wall. In addition, by performing several preliminary simulations, it was found that the tunnel portion most prone to spalling (i.e., characterized by concrete surface temperatures above 250 °C) had a length of 65 m, of which 15 m upstream and 50 m downstream of the fire center. It is also worth mentioning that the most severe fire-induced damage was found at the end of the simulation time (i.e., after 120 min of fire exposure). On this basis, the spalling damage, referred to the time t = 120 min from the fire start, was assessed with reference to the ceiling and the right wall of the investigated tunnel, of which only a 65 m long portion was considered.

In order to reach the fixed goal, the Fire Dynamics Simulator (FDS) code was used as a CFD simulation tool. In FDS, spalling can be modeled as an energy-consuming reaction. On this basis, in the developed 3D CFD model, spalling was assumed to be a consequence of the decomposition of calcium carbonate, which is an endothermic reaction that leads to the degradation of concrete. The main parameter for the application of the proposed 3D CFD model is the reference temperature, which was assumed to be equivalent to the critical temperature (i.e., the temperature above which spalling occurs). In addition, it is also to be stressed that the proposed 3D CFD model is able to capture changes in the thermal properties of concrete with temperature.

The first step of this study was to validate the developed 3D CFD model by comparing its results with those provided by a competing model present in the international literature. On the basis of this comparison (an error of no more than 5% was found), it was possible to state that the proposed 3D CFD model offered a realistic representation of fire-induced damage in a road tunnel.

Once the developed 3D CFD model was validated, the following conclusions can be drawn.

The results obtained from the proposed 3D CFD model showed, first of all, that the highest concrete surface temperatures were predicted along the right wall, which was also characterized by the fastest increase in the cited temperatures. These might be the reasons why: (i) the maximum spalling depth, and thus the greatest spalling amount, occurred along the right wall; (ii) the spalling started earlier on the right wall than beneath the ceiling; (iii) the spalling affected the right wall throughout its height not only for reference temperatures of 380 °C as beneath the ceiling. However, on the other hand, it is to be said that the concrete surface temperatures along the tunnel length were found to be on average higher beneath the ceiling than on the right wall. This might be the reason why both the spalling length and the spalled concrete area were found to be greatest beneath the ceiling. Generally speaking, the results also showed that the severity of fire-induced damage increased as the reference temperature decreased.

Finally, by comparing the results obtained from the developed 3D CFD model with those provided by a conventional heat transfer analysis that does not consider the structural loss, it was found that in order to reliably predict and evaluate the fire resistance of a tunnel subjected to a severe fire, it is appropriate to use a model such as the one proposed, namely a model that takes into account fire-induced damage. In fact, conventional heat transfer analyses, ignoring structural loss, underestimate spalling.

3.8. References

[58] André, L., Abanades, S., 2017. Evaluation and performances comparison of calcium, strontium and barium carbonates during calcination/carbonation reactions for solar thermochemical energy storage. Journal of Energy Storage 13, 193-205.

[59] Caliendo, C., Ciambelli, P., De Guglielmo, M.L., Meo, M.G., Russo, P., 2012. Numerical simulation of different HGV fire scenarios in curved bi-directional road tunnels and safety evaluation. Tunnelling and Underground Space Technology 31, 33–50.

[60] Caliendo, C., Ciambelli, P., De Guglielmo, M.L., Meo, M.G., Russo, P., 2013. Simulation of fire scenarios due to different vehicle types with and without traffic in a bi-directional road tunnel. Tunnelling and Underground Space Technology 37, 22–36.

[61] Caliendo, C., Ciambelli, P., De Guglielmo, M.L., Meo, M.G., Russo, P., 2018. Computational analysis of fire and people evacuation for different positions of burning vehicles in a road tunnel with emergency exits. Cogent Engineering 5, 1530834.

[62] Caliendo, C., Genovese, G., Russo, I., 2021a. Risk analysis of road tunnels: A computational fluid dynamic model for assessing the effects of natural ventilation. Applied Sciences 11, 32, doi:10.3390/app11010032.

[63] Caliendo, C., Russo, I., Genovese, G., 2021b. Risk analysis of one-way road tunnel tube used for bi-directional traffic under fire scenarios. Applied Sciences, 11, 3198, doi:10.3390/app11073198.

[64] Caliendo, C., Genovese, G., Russo, I., 2021c. A Numerical Study for Assessing the Risk Reduction Using an Emergency Vehicle Equipped with a Micronized Water System for Contrasting the

Fire Growth Phase in Road Tunnels. Applied Sciences 11, 5248, https://doi.org/10.3390/app11115248.

[65] Eurocode 2, 2004. Design of Concrete Structures, Part 1-2: General Rules - Structural Fire Design. Commission of European Communities, Brussels.

[66] FIT-European Thematic Network Fire in Tunnels, 2005. Design Fire Scenarios. Technical Report Part 1, A. Haack, STUVA.

[67] ITA-International Tunneling Association, 2004. Guidelines for Structural Fire Resistance for Road Tunnels. Working Group No. 6 Maintenance and Repair.

[68] McGrattan, K., Hostikka, S., Floyd, J., McDermott, R., Vanella, M., 2019a. Fire Dynamics Simulator: User's Guide. NIST, Special Publication 1019. Available online: https://pages.nist.gov/fds-smv/manuals.html (accessed on 13 March 2021).

[69] NFPA 502, 2011. Standard for Road Tunnels, Bridges, and Other Limited Access Highways. National Fire Protection Association. Technical Committee on Road Tunnel and Highway Fire Protection, American National Standards Institute, Quincy, MA.

[70] Phan, L.; Carino, N. Effects of Test Conditions and Mixture Proportions on Behavior of High-Strength Concrete Exposed to High Temperatures. *ACI Mater. J.* **2002**, *99*, 54-56.

[71] PIARC, 1999. Fire and Smoke Control in Road Tunnels. PIARC Technical Committee C5 Road Tunnel. <http://www.piarc.org>.

[72] PIARC, 2007. Systems and Equipment for Fire and Smoke Control in Road Tunnels. PIARC Technical Committee C5 Road Tunnel. <http://www.piarc.org>.

[73] Qiao, R., Shao, Z., Liu, F., Wei, W., 2019. Damage evolution and safety assessment of tunnel lining subjected to long-duration fire. Tunnelling and Underground Space Technology 83, 354-363.

[74] Rodriguez-Navarro, C., Ruiz-Agudo, E., Luque, A., Rodriguez-Navarro, A.B., Ortega-Huertas, M., 2009. Thermal decomposition of calcite: Mechanisms of formation and textural evolution of CaO nanocrystals. American Mineralogist 94 (4), 578-593.

[75] Sanders, J.P., Gallagher, P.K., 2002. Kinetic analyses using simultaneous TG/DSC measurements. Thermochimica Acta 388 (1-2), 115-128.

[76] Schrefler, B.A., Brunello, P., Gawin, D., Majorana, C.E., Pesavento, F., 2002. Concrete at high temperature with application to tunnel fire. Computational Mechanics 29, 43-51.

[77] SFPE, 1995. In: DiNenno, P.J., et al. (Eds.) The SFPE Handbook of Fire Protection Engineering, second ed. National Fire Protection Association, Quincy, USA.

[78] The Engineering ToolBox. Available online: https://www.engineeringtoolbox.com/ (accessed on 29 August 2021).

[79] Trník, A., Scheinherrová, L., Medveď, I., Černý, R., 2015. Simultaneous DSC and TG analysis of high-performance concrete containing natural zeolite as a supplementary cementitious material. Journal of Thermal Analysis and Calorimetry 121 (1), 67-73.

[80] Wang, X., Fleischmann, C., Spearpoint, M., 2016. Assessing the influence of fuel geometrical shape on fire dynamics simulator (FDS) predictions for a large-scale heavy goods vehicle tunnel fire experiment. Case Studies in Fire Safety 5, 34-41.

Chapter 4

Spalling prediction models

4.1. Introduction

The damage that spalling can cause to a concrete structure can make the calculations of fire safety design imprecise, leading the structure to significantly reduced safety levels in the event of a fire. Therefore, it is very important to develop a model that can realistically predict fire-induced damage. So far, however, the prediction of spalling during concrete heating has been more especially an inaccurate empirical exercise. In fact, the different attempts made in order to predict fire-induced damage by analytical methods have failed (*Khoury, 2000*).

In the light of the above considerations, the main scope of the present thesis is to develop, based on the 3D CFD model presented in the previous Chapter, certain predictive models, namely an analytical method, capable of estimating fire-induced damage as a function of both the geometric characteristics of the tunnel and the fire scenario.

Different assumptions are made, and several preliminary simulations are carried out in order to define the set of variables that mainly affect spalling. Subsequently, on the basis of the data obtained by performing 120 3D CFD simulations, predictive models capable of assessing the maximum spalling depth, the spalling start time, and the maximum length of the tunnel affected by spalling are developed with respect to both the ceiling and the right wall. Then, the predictive capabilities of the developed models are tested, and the relevant conclusions are drawn with reference to the practical use of these models by both road engineers and Tunnel Management Agencies (TMAs).

4.2. Statistical approach

As mentioned above, the main scope of this thesis is to develop models capable of predicting the maximum spalling depth, the spalling start time, and the maximum length of the tunnel affected by spalling as a function of both the tunnel geometry and the fire scenario. For this aim, the classical statistical approach was applied. In this regard, it is to be said that the LIMDEP statistical package (*Greene, 2007*) was used as a statistical simulation tool.

It is to be stressed that an alternative to the classical statistical approach might also be the Bayesian method, which allows to include prior information on parameter values in the estimation procedure to obtain a posterior estimate of values of the parameters and some functions thereof (for more details see *Caliendo et al., 2021*).

A statistical model is usually defined as a mathematical relationship between one or more dependent variables (*Y*) and other independent variables (*X*).

4.2.1. Dependent variables

In the present thesis, three different dependent variables are taken into account:

- Maximum spalling depth: Y_1;
- Time required to reach a spalling depth of 0.005 m (or the *spalling start time* for brevity): Y_2;
- Maximum length of the tunnel affected by a spalling depth of at least 0.005 m (or the *maximum spalling length* for brevity): Y_3.

The predictive models developed in this study are univariate Negative Binomial (NB) models with fixed parameters. This means that the dependent variable is one for each model and that it is distributed according to an NB distribution. In addition, the parameters of the model are assumed to be fixed, even though it was observed that correlated random-parameter models are statistically superior to the corresponding fixed-parameter models (for more details see *Caliendo et al., 2019; Astarita et al., 2020*). However, the last assumption is due to the fact that, in contrast to fixed-parameter models, correlated random-parameter models require a large dataset in order to provide accurate estimates.

In the light of the above considerations, the expected value of the i-th dependent variable (λ_i) is defined as follows:

$$(4.1)\ \lambda_i = \exp(\mathbf{X}^T \boldsymbol{\beta}_i) \quad i = 1, 2, \text{and } 3,$$

where $\boldsymbol{\beta}_i$ is the vector of fixed, even if unknown, coefficients of the i-th dependent variable and $\mathbf{X}$ is the k-dimensional vector containing the independent variables (X).

4.2.2. Independent variables

The severity of spalling damage might depend on numerous variables, among which the main ones are:

- Longitudinal ventilation (v);
- Maximum HRR (HRR_{max});
- Time to reach HRR_{max} (t_{max}) and fire duration;
- Tunnel cross-section area (A);
- Longitudinal slope (s);
- Location and dimensions of the burning vehicle;
- Reference (or critical) temperature;
- Moisture content of concrete.

It is to be said that each of these variables might potentially be an independent variable. In this study, however, the set of X variables was defined based on certain assumptions.

4.2.2.1. Assumptions

4.2.2.1.1. Longitudinal ventilation

The longitudinal ventilation (v) along the tunnel length is assumed to be on average 5 m/s if the tunnel is equipped with a mechanical ventilation system, while v = 0.5 m/s when the longitudinal ventilation within the tunnel is natural and is due to the piston effect of moving vehicles (see Section 3.2.2).

Therefore, the longitudinal ventilation is assumed to be an independent variable that can take two values: 5 m/s or 0.5 m/s.

4.2.2.1.2. Maximum HRR

Three distinct heavy vehicle fires are investigated: a bus and two different types of HGVs. Specifically, it is assumed that the bus is able to develop a 30 MW fire, while the HGVs are capable of developing 50 MW and 100 MW fires. In this respect, it is to be said that these fires are those with the highest probability of occurring in the event of a heavy vehicle fire (*ANAS, 2009*).

It is also to be stressed that since light vehicle fires lead to temperatures much lower than 380 °C (*Caliendo et al., 2013*), light vehicle fires are not expected to induce damage.

Therefore, the maximum HRR (HRR_{max}) is assumed to be an independent variable that can take three different values: 30 MW, 50 MW, and 100 MW.

4.2.2.1.3. Time to reach HRR_{max} and fire duration

The time to reach HRR_{max} is assumed to be 5 min from the fire start for each burning vehicle in order to simulate the worst-case fire scenario.

The fire duration, instead, is 60 min. In fact, within 60 min from the fire start, it is assumed that firefighters have started to extinguish the fire.

Therefore, the time to reach HRR_{max} and fire duration are not assumed to be independent variables.

Fig. 4.1 shows the different HRR curves over time.

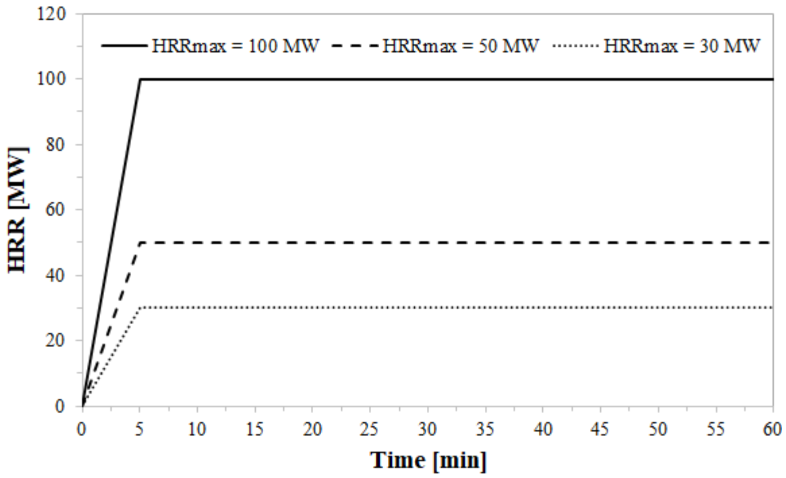

Fig. 4.1. The different HRR curves over time.

4.2.2.1.3. Tunnel cross-section area

The investigated tunnels have a rectangular cross-section of area A with a width of W and a height of H.

The tunnel width (W) is assumed to be 7 m, 10.5 m, and 14 m. Specifically, the width of 7 m corresponds to tunnels with only two lanes of 3.5 m each one, thus representing roughly the minimum width of a tunnel; while the width of 14 m is related to tunnels with three lanes, an emergency lane, two sidewalks, and two shoulders, thus representing more or less the maximum width of a tunnel. The width of 10.5 m, instead, corresponds to two-lane tunnels with two sidewalks and two shoulders (see Section 3.2.1).

The tunnel height (H) is assumed to be 5 m, 6 m, and 7 m. In particular, the height of 5 m represents roughly the minimum height of a tunnel (*PIARC, 2001*), while above a height of 7 m no serious damage is expected because the vertical distance between the ceiling and the upper surface of the fire source would exceed 3 m.

As a result, the tunnel cross-section area (i.e., A = W x H) is assumed to be an independent variable that can take different values as a function of the W and H values. In this respect, it is assumed that the tunnel width is: 7 m, 10.5 m, and 14 m, while the tunnel height is: 5 m, 6 m, and 7 m.

4.2.2.1.4. Longitudinal slope

The longitudinal slope (s) can influence the propagation of both hot gases and smoke within the tunnel, as well as the walking speed of escaping people. In fact, *Jiang et al. (2011)* found that the longitudinal slope had certain effects on the gas temperature beneath the tunnel ceiling, as well as that these effects were higher for negative slopes than for positive slopes. In this respect, it is also to be said that the longitudinal slope of a road tunnel is generally less than 4% (*PIARC, 2007*).

In the light of the above considerations, the longitudinal slope is assumed to be an independent variable that can take five different values: -4%, -2%, 0%, 2%, and 4%.

4.2.2.1.5. Location and dimensions of the burning vehicle

The burning vehicle consists of a bus and two different types of HGVs. Specifically, these vehicles, which are schematized as a rectangular block located at 0.4 m from the road pavement, are assumed to have the same dimensions (length x width x height): 12 x 2.5 x 3.2 m^3.

In addition, the fire source is assumed to be located close to the right sidewalk in the middle of the tunnel length in order to simulate the worst-case fire scenario (see Section 3.3).

Therefore, the location and dimensions of the burning vehicle are not assumed to be independent variables.

4.2.2.1.6. Reference (or critical) temperature

As mentioned above, the reference temperature is assumed to be equivalent to the critical temperature (i.e., the temperature above which spalling occurs).

The results found in Chapter 3 showed that fire-induced damage decreased passing from T_{ref} = 380 °C to T_{ref} = 700 °C. On this basis, the reference (or critical) temperature is assumed to be equal to 380 °C (*ITA, 2004*) in order to simulate the worst-case spalling scenario.

As a result, the reference temperature is not assumed to be an independent variable.

4.2.2.1.7. Moisture content of concrete

It is believed that high strength concretes, more especially those with a moisture content greater than 2-3% by weight of concrete, are most susceptible to spalling due to their low permeability compared to normal strength concretes (*Khoury, 2000*).

On this basis, the walls and ceiling of the investigated tunnel are assumed to be made of an HSC with a moisture content of 3% by weight of concrete in order to simulate the worst-case spalling scenario.

Therefore, the moisture content of concrete is not assumed to be an independent variable.

Summing up, the above-mentioned assumptions served to define the set of the independent variables, which includes:

- Longitudinal ventilation (v): 5 m/s and 0.5 m/s;
- Maximum HRR (HRR_{max}): 30 MW, 50 MW, and 100 MW;
- Tunnel cross-section area (i.e., A = W x H), namely:
  - Tunnel width (W): 7 m, 10.5 m, and 14 m;
  - Tunnel height (H): 5 m, 6 m, and 7 m;
- Longitudinal slope (s): -4%, -2%, 0%, 2%, and 4%.

However, there are many possible combinations among the values of these independent variables.

4.3. Preliminary simulations

Several preliminary simulations are carried out in order to attempt to reduce the set of the independent variables.

It is to be stressed that these simulations are based on the 3D CFD model presented in Chapter 3, except for the length of the tunnel portion most susceptible to spalling (i.e., characterized by concrete surface temperatures above T_{ref} = 380 °C) that was found to be 80 m in the event of a tunnel fire in the absence of the mechanical ventilation system (i.e., v = 0.5 m/s). On this basis, the above-mentioned simulations are related to a tunnel portion with a length of 80 m, of which 27 m upstream and 53 m downstream of the fire center.

It is also to be said that in the present thesis spalling is assumed to occur only where (and when) fire-induced damage affects the concrete for a depth of at least 0.005 m.

The results obtained from these simulations are expressed in terms of spalling depth profiles along the length of both the ceiling and the right wall after 60 min from the fire start.

Specifically, the cited profiles pass through the point where, in the different simulations, the maximum spalling depth, but not necessarily the maximum spalling length, is measured. For the sake of brevity, however, only the results relating to the ceiling are shown below, while those referring to the right wall are reported in Chapter 7. In this respect, it is to be stressed that these preliminary simulations only aim at identifying the independent variables that have the greatest influence on fire-induced damage; in fact, the validity of the results provided by the proposed 3D CFD model, as well as their interpretation, was discussed in Chapter 3.

In addition, a unique code was assigned to each simulation in order to facilitate its identification. These codes are of the type: HRR_{max}_WxH_v_s. For example, the identification code corresponding to the case of a 100 MW fire in a flat tunnel of 10.5 x 6 m^2 (width x height) equipped with a mechanical ventilation system is 100_10.5x6_5_0.

4.3.1. Longitudinal ventilation

The longitudinal ventilation is assumed to be on average 5 m/s if the tunnel is equipped with a mechanical ventilation system, while v = 0.5 m/s when the longitudinal ventilation within the tunnel is natural and is due to the piston effect of moving vehicles.

Fig. 4.2 shows the spalling depth profiles predicted beneath the ceiling as a function of the longitudinal ventilation.

From Fig. 4.2 it is possible to observe that the maximum spalling depth along the length of the ceiling varied significantly with the longitudinal ventilation, reaching the highest value for v = 0.5 m/s and the lowest value for v = 5 m/s. Specifically, the maximum spalling depth is about 0.028 m and 0.062 m for an average longitudinal ventilation of 5 m/s and 0.5 m/s, respectively. As a results, it increased by about 53% passing from v = 5 m/s to v = 0.5 m/s.

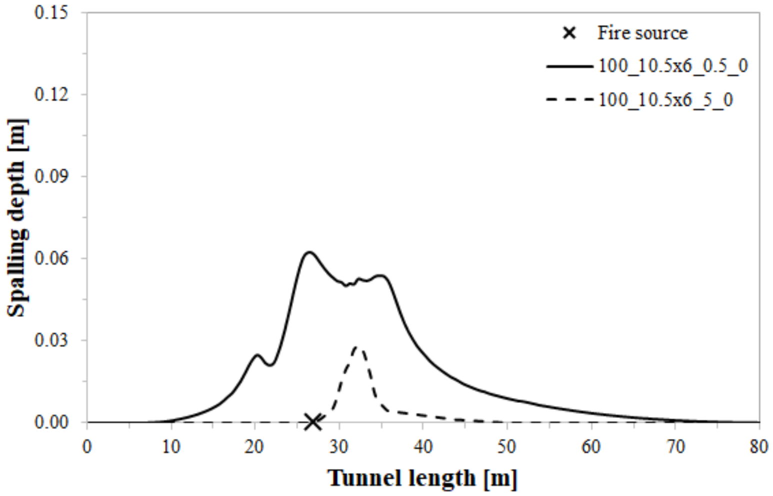

Fig. 4.2. Longitudinal sections. Spalling depth profiles predicted beneath the ceiling as a function of the longitudinal ventilation; t = 60 min.

From Fig. 4.2 one can also see that the length of the tunnel affected by a spalling depth of at least 0.005 m increased as the longitudinal ventilation decreased. In fact, it is about 6.5 m and 42 m for v = 5 m/s and v = 0.5 m/s, respectively. On this basis, the spalling length increased by approximately 85% by reducing the average longitudinal ventilation from 5 m/s to 0.5 m/s.

It is to be said that longitudinal ventilation tends to cool hot gases. This might be the reason why the most severe fire-induced damage was found for the lowest average longitudinal ventilation.

Therefore, these results confirmed that longitudinal ventilation significantly affects fire-induced damage. For this reason, it is assumed to be an independent variable that can take two values: 5 m/s and 0.5 m/s.

4.3.2. Maximum HRR

Three distinct heavy vehicle fires are investigated: a bus and two different types of HGVs. Specifically, it is assumed that the bus is able to develop a 30 MW fire, while the HGVs are capable of developing 50 MW and 100 MW fires.

4.3.2.1. With a mechanical ventilation system

Fig. 4.3 shows the spalling depth profiles predicted beneath the ceiling as a function of the maximum heat release rate when the tunnel is equipped with a mechanical ventilation system (i.e., $v = 5$ m/s).

From Fig. 4.3 it is possible to observe that the peak spalling depth along the length of the ceiling also changed considerably with the maximum heat release rate, reaching the highest value for HRR_{max} = 100 MW and the lowest value for HRR_{max} = 30 MW. In particular, the peak spalling depth is approximately 0.008, 0.015, and 0.028 m for 30 MW, 50 MW, and 100 MW fires, respectively. Consequently, it increased by about 71% passing from HRR_{max} = 30 MW to HRR_{max} = 100 MW.

From Fig. 4.3 one can also see that the length of the tunnel affected by a spalling depth of at least 0.005 m increased as the maximum heat release rate increased. In fact, it is approximately 1.5 m, 3 m, and 6.5 m for HRR_{max} = 30 MW, HRR_{max} = 50 MW, and HRR_{max} = 100 MW, respectively. As a result, the spalling length increased by about 77% by raising the maximum heat release rate from 30 MW to 100 MW.

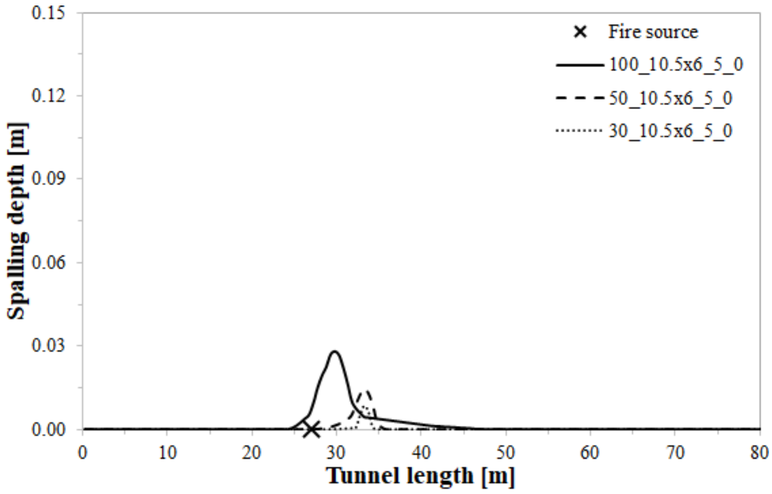

Fig. 4.3. Longitudinal sections. Spalling depth profiles predicted beneath the ceiling as a function of the maximum heat release rate; v = 5 m/s and t = 60 min.

4.3.2.2. Without a mechanical ventilation system

Fig. 4.4 shows the spalling depth profiles predicted beneath the ceiling as a function of the maximum heat release rate when the tunnel is not equipped with a mechanical ventilation system (i.e., v = 0.5 m/s).

From Fig. 4.4 one can see that the maximum spalling depth along the length of the ceiling varied significantly with the HRR_{max} also when the tunnel is not equipped with a mechanical ventilation system (i.e., v = 0.5 m/s), reaching the highest value for HRR_{max} = 100 MW and the lowest value for HRR_{max} = 30 MW. Specifically, the maximum spalling depth is about 0.022, 0.041, and 0.062 m for 30 MW, 50 MW, and 100 MW fires, respectively. As a result, it increased by approximately 65% passing from HRR_{max} = 30 MW to HRR_{max} = 100 MW.

At the same time, from Fig. 4.4 it is also possible to observe that the length of the tunnel affected by a spalling depth of at least 0.005 m increased significantly with the increase of the maximum heat release rate. In fact, it is about 10 m, 18.5 m, and 42 m for HRR_{max} = 30 MW, HRR_{max} = 50 MW, and HRR_{max} = 100 MW, respectively. On this basis, the spalling length increased by approximately 76% by raising HRR_{max} from 30 MW to 100 MW.

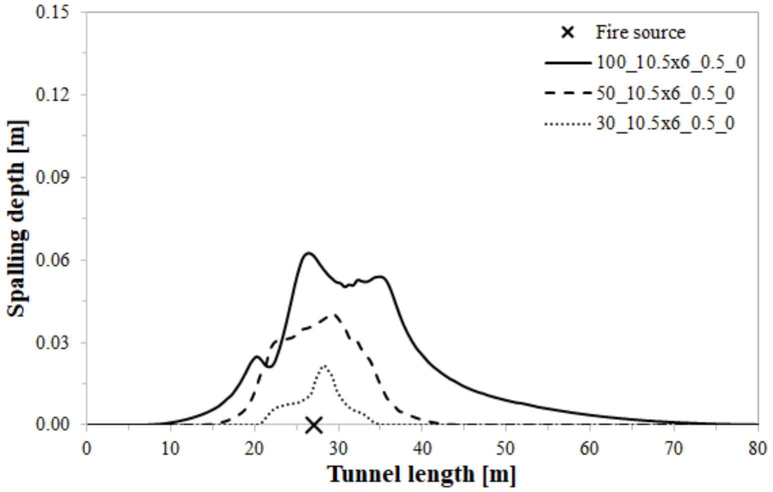

Fig. 4.4. Longitudinal sections. Spalling depth profiles predicted beneath the ceiling as a function of the maximum heat release rate; v = 0.5 m/s and t = 60 min.

Summing up, the findings showed that the most severe fire-induced damage was measured when the tunnel was not equipped with a mechanical ventilation system (i.e., v = 0.5 m/s). Specifically, it is to be stressed that the spalling depth was found to be much less than the typical thickness of the concrete cover (i.e., 0.05 m) for 30 MW fires both with and without a mechanical ventilation system. This means that it is not necessary to investigate HRRs smaller than 30 MW because they would produce negligible damage. At the same time, fires larger than 100 MW have a very low probability of occurrence.

Therefore, these results confirmed that, both with and without a mechanical ventilation system, the maximum heat release rate significantly affects fire-induced damage. In the light of the above considerations, HRR_{max} is assumed to be an independent variable that can take three different values: 30 MW, 50 MW, and 100 MW.

4.3.3. Tunnel cross-section area

4.3.3.1. Tunnel width

The tunnel width is assumed to be 7 m, 10.5 m, and 14 m in order to consider a vast range of tunnels. In fact, the range of tunnel widths 7-14 m includes from tunnels with only two lanes (i.e., 7 m wide) to three-lane tunnels with an emergency lane, two sidewalks, and two shoulders (i.e., 14 m wide).

4.3.3.1.1. With a mechanical ventilation system

Fig. 4.5 shows the spalling depth profiles predicted beneath the ceiling as a function of the tunnel width for the average longitudinal ventilation of 5 m/s.

From Fig. 4.5 it is possible to observe that the maximum spalling depth along the length of the ceiling was almost the same as the tunnel width varied, reaching the highest value for W = 14 m and the lowest value for W = 7 m. Specifically, the maximum spalling depth is about 0.027, 0.028, and 0.029 m for W = 7 m, W = 10.5 m, and W = 14 m, respectively. As a result, it increased by approximately 7% passing from W = 7 m to W = 14 m.

From Fig. 4.5 one can also see that the length of the tunnel affected by a spalling depth of at least 0.005 m increased as the tunnel width decreased. In fact, it is about 8 m, 6.5 m, and 6 m for W = 7 m, W = 10.5 m, and W = 14 m, respectively. On this basis, the spalling length increased by approximately 25% by reducing the tunnel width from 14 m to 7 m.

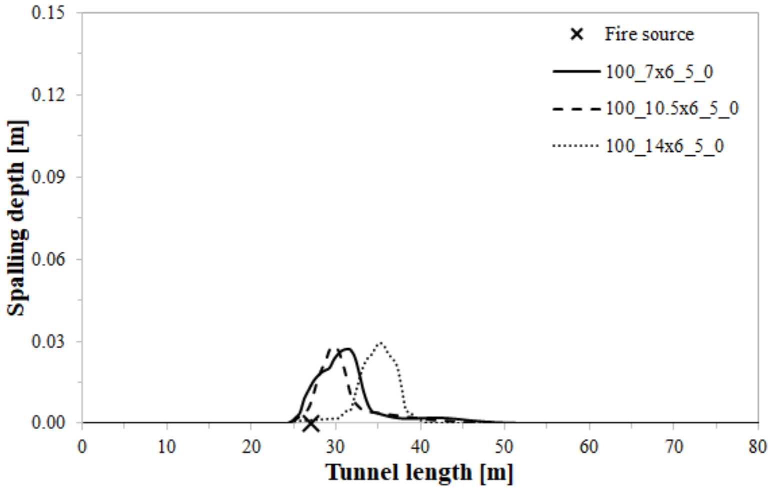

Fig. 4.5. Longitudinal sections. Spalling depth profiles predicted beneath the ceiling as a function of the tunnel width; v = 5 m/s and t = 60 min.

4.3.3.1.2. Without a mechanical ventilation system

Fig. 4.6 shows the spalling depth profiles predicted beneath the ceiling as a function of the tunnel width for the average longitudinal ventilation of 0.5 m/s.

From Fig. 4.6 one can see that the maximum spalling depth along the length of the ceiling did not vary considerably with the tunnel width also for the average longitudinal ventilation of 0.5 m/s, reaching the maximum value for W = 14 m and the minimum value for W = 7 m. In particular, the peak spalling depth is about 0.061, 0.062, and 0.067 m for W = 7 m, W = 10.5 m, and W = 14 m, respectively. As a result, it increased by approximately 9% passing from W = 7 m to W = 14 m.

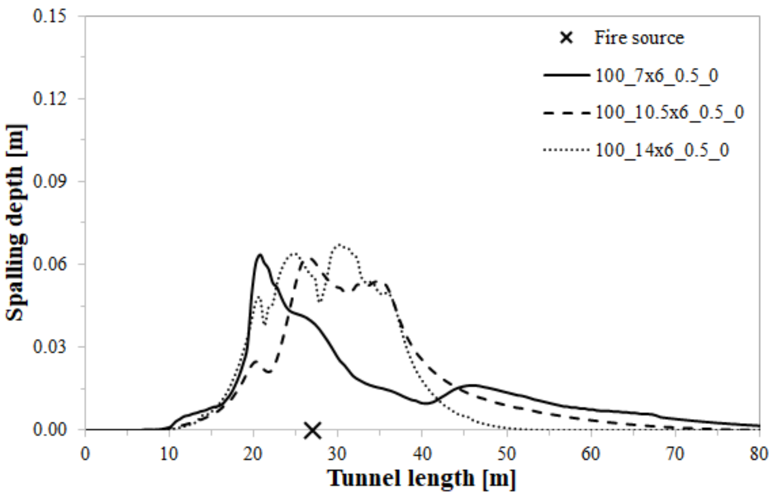

Fig. 4.6. Longitudinal sections. Spalling depth profiles predicted beneath the ceiling as a function of the tunnel width; v = 0.5 m/s and t = 60 min.

At the same time, from Fig. 4.6 it is also possible to observe that the length of the tunnel affected by a spalling depth of at least 0.005 m increased significantly with decreasing the tunnel width. In fact, it is approximately 56.5 m, 42 m, and 32 m for W = 7 m, W = 10.5 m, and W = 14 m, respectively. On this basis, the spalling length increased by about 43% by reducing the tunnel width from 14 m to 7 m.

Summing up, also with respect to the tunnel width, the findings showed that the most severe fire-induced damage was measured when the tunnel was not equipped with a mechanical ventilation system (i.e., v = 0.5 m/s).

Therefore, these results confirmed that, more especially in terms of the spalling length, the tunnel width has a certain impact on fire-induced damage. On this basis, the tunnel width is assumed to be an independent variable that can take three different values: 7 m, 10.5 m, and 14 m, so as to include from tunnels with only two lanes (i.e., 7 m wide) to three-lane tunnels with an emergency lane, two sidewalks, and two shoulders (i.e., 14 m wide).

4.3.3.2. Tunnel height

As mentioned above, the tunnel height is assumed to be 5 m, 6 m, and 7 m. Specifically, the height of 5 m corresponds more or less to the minimum height of a tunnel, while above a height of 7 m no severe spalling damage is expected due to the large vertical distance between the ceiling and the upper surface of the burning vehicle.

4.3.3.2.1. With a mechanical ventilation system

Fig. 4.7 shows the spalling depth profiles predicted beneath the ceiling as a function of the tunnel height for the average longitudinal ventilation of 5 m/s.

From Fig. 4.7 it is possible to observe that the maximum spalling depth along the length of the ceiling changed quite with the tunnel height, reaching the highest value for H = 5 m and the lowest value for H = 7 m. Specifically, the maximum spalling depth is about 0.030, 0.028, and 0.025 for H = 5 m, H = 6 m, and H = 7 m, respectively. As a result, it increased by approximately 17% by reducing the tunnel height from 7 m to 5 m.

From Fig. 4.7 one can also see that the length of the tunnel affected by a spalling depth of at least 0.005 m increased as the tunnel height decreased. In fact, it is approximately 7.5 m, 6.5 m, and 5.5 m for H = 5 m, H = 6 m, and H = 7 m, respectively. On this basis, the spalling length increased by about 27% passing from H = 7 m to H = 5 m.

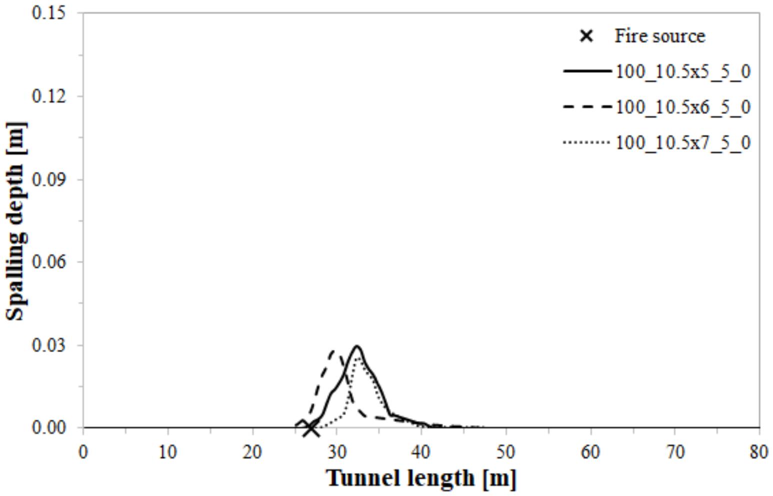

Fig. 4.7. Longitudinal sections. Spalling depth profiles predicted beneath the ceiling as a function of the tunnel height; v = 5 m/s and t = 60 min.

4.3.3.2.2. Without a mechanical ventilation system

Fig. 4.8 shows the spalling depth profiles predicted beneath the ceiling as a function of the tunnel height for the average longitudinal ventilation of 0.5 m/s.

From Fig. 4.8 one can see that the maximum spalling depth along the length of the ceiling did not vary significantly with the tunnel height also for the average longitudinal ventilation of 0.5 m/s, reaching the maximum value for H = 5 m and the minimum value for H = 7 m. Specifically, the peak spalling depth is about 0.063, 0.062, and 0.061 for H = 5 m, H = 6 m, and H = 7 m, respectively. Consequently, it only increased by approximately 3% by reducing the tunnel height from 7 m to 5 m.

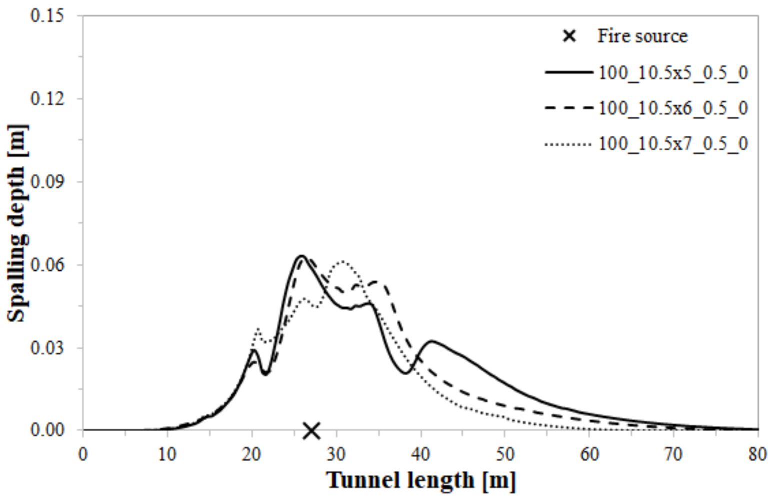

Fig. 4.8. Longitudinal sections. Spalling depth profiles predicted beneath the ceiling as a function of the tunnel height; v = 0.5 m/s and t = 60 min.

At the same time, from Fig. 4.8 it is also possible to observe that the length of the tunnel affected by a spalling depth of at least 0.005 m increased significantly with decreasing the tunnel height. In fact, it is about 47 m, 42 m, and 36 for H = 5 m, H = 6 m, and H = 7 m, respectively. On this basis, the spalling length increased by approximately 23% passing from H = 7 m to H = 5 m.

Summing up, also with respect to the tunnel height, the findings showed that the most severe fire-induced damage was measured for the average longitudinal ventilation of 0.5 m/s.

Therefore, these results confirmed that the tunnel height has a certain influence, more especially in terms of the spalling length, on fire-induced damage. On this basis, the tunnel height is assumed to be an independent variable that can take three different values: 5 m, 6 m, and 7 m.

4.3.4. Longitudinal slope

The longitudinal slope of the tunnel is assumed to be -4%, -2%, 0%, 2%, and 4% after making certain considerations.

4.3.4.1. With a mechanical ventilation system

Fig. 4.9 shows the spalling depth profiles predicted beneath the ceiling as a function of the longitudinal slope when the tunnel is equipped with a mechanical ventilation system (i.e., v = 5 m/s).

From Fig. 4.9 one can see that the maximum spalling depth along the length of the ceiling is almost the same as the longitudinal slope changes, reaching the highest value for s = -4% and the lowest value for s = 4%. In particular, the maximum spalling depth is approximately 0.0283, 0.0281, and 0.0278 for s = -4%, s = 0%, and s = 4%, respectively. As a result, it only increased by about 2% passing from s = 4% to s = -4%.

From Fig. 4.9 it is also possible to observe that even the length of the tunnel affected by a spalling depth of at least 0.005 m is almost the same as the longitudinal slope varies. In fact, it is about 6.5 m, 6.5 m, and 6 m for s = -4%, s = 0%, and s = 4%, respectively. On this basis, the spalling length only increased by approximately 7% passing from s = 4% to s = -4%.

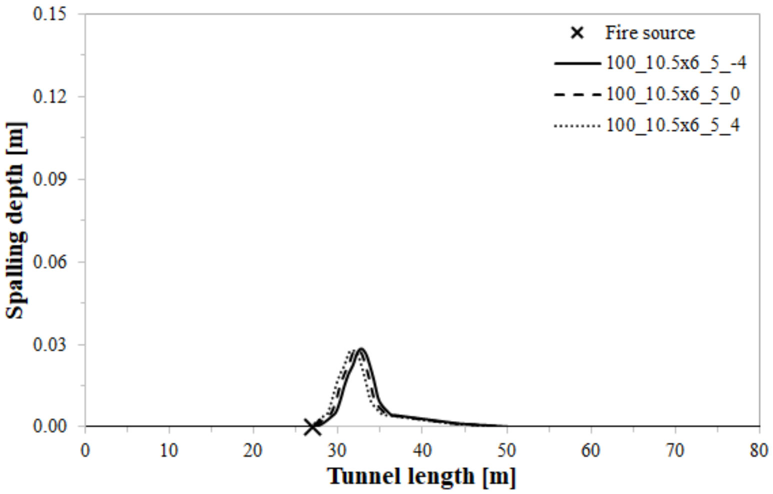

Fig. 4.9. Longitudinal sections. Spalling depth profiles predicted beneath the ceiling as a function of the longitudinal slope; v = 5 m/s and t = 60 min.

It is also to be stressed that the results related to both s = -2% and s = 2% were not reported here in order to make Fig. 4.9 clearer.

4.3.4.2. Without a mechanical ventilation system

Fig. 4.10 shows the spalling depth profiles predicted beneath the ceiling as a function of the longitudinal slope when the tunnel is not equipped with a mechanical ventilation system (i.e., v = 0.5 m/s).

From Fig. 4.10 one can see that the maximum spalling depth along the length of the ceiling did not vary significantly with the longitudinal slope also for the average longitudinal ventilation of 0.5 m/s. In fact, the maximum spalling depths are quite similar to each other for the different values of the longitudinal slope.

At the same time, also the length of the tunnel affected by a spalling depth of at least 0.005 m is almost the same as the longitudinal slope changes.

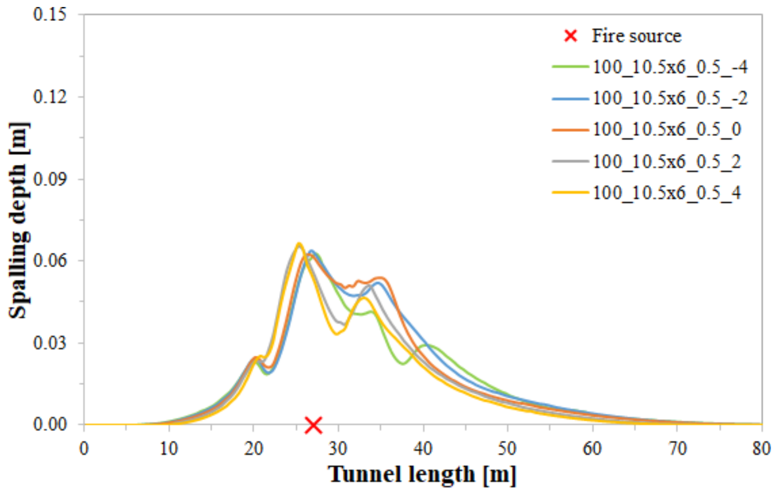

Fig. 4.10. Longitudinal sections. Spalling depth profiles predicted beneath the ceiling as a function of the longitudinal slope; v = 0.5 m/s and t = 60 min.

Summing up, the findings showed that fire-induced damage did not vary significatively with the longitudinal slope both with and without a mechanical ventilation system. However, while these variations were most evident for v = 0.5 m/s, they were completely negligible for v = 5 m/s.

In the light of the above considerations and taking into account the fact that the most severe fire-induced damage was observed for v = 0.5 m/s, the longitudinal slope is assumed to be an independent variable only when the average longitudinal velocity within the tunnel is 0.5 m/s. In other terms, it is assumed that the tunnel is always flat (i.e., s = 0%) for v = 5 m/s and has a longitudinal slope of -4%, -2%, 0%, 2%, and 4% when v = 0.5 m/s.

4.4. Dataset description

The previous results served to further reduce the set of independent variables, which in conclusion includes:

- Longitudinal ventilation (v): 5 m/s and 0.5 m/s;
- Maximum HRR (HRR_{max}): 30 MW, 50 MW, and 100 MW;
- Tunnel cross-section area (i.e., A = W x H), namely:
  - Tunnel width (W): 7 m, 10.5 m, and 14 m;
  - Tunnel height (H): 5 m, 6 m, and 7 m;
- Longitudinal slope (s):
  - s = 0% if v = 5 m/s;
  - s = -4%, -2%, 0%, 2%, and 4% if v = 0.5 m/s.

Among all possible combinations of the values that can take the above-mentioned independent variables, the predictive models developed in this thesis are based on data obtained by running 120 simulations.

4.4.1. Statistical analysis

4.4.1.1. Independent variables

The independent variable v is assumed to be a dummy variable: v = 1 if there is a mechanical ventilation system (i.e., the average longitudinal ventilation is 5 m/s), v = 0 otherwise. In this respect, the average longitudinal ventilation is assumed to be 5 m/s (i.e., v = 1) in 30 simulations, while it is 0.5 m/s (i.e., v = 0) in the remaining 90 simulations.

The maximum heat release rate is assumed to be 30 MW, 50 MW, and 100 MW. Each of these HRRs is launched in 40 simulations. It is to be stressed that the independent variable HRR_{max} is considered in the natural logarithm (*ln*) form.

The tunnel cross-section area (i.e., A = W x H) is assumed to be 35 m^2, 42 m^2, 49 m^2, 52.5 m^2, 63 m^2, 70 m^2, 73.5 m^2, 84 m^2, and 98 m^2, of which each one is run in about 13 simulations. It is to be said that also the independent variable A is considered in the natural logarithm (*ln*) form.

The longitudinal slope is assumed to be always 0% for v = 1, while it is -4%, -2%, 0%, 2%, and 4% when v = 0. On this basis, s = 0% is launched in 48 simulations, of which 30 for v = 1 and 18 for v = 0; the remaining values of s are run in 18 simulations each one. It is to be stressed that the longitudinal slope is expressed as a percentage in the proposed predictive models.

Table 4.1 shows the summary statistic of the maximum heat release rate (HRR_{max}), the tunnel cross-section area (A), and the longitudinal slope (s).

Table 4.1. Summary statistic of variables.

Statistic	*ln*HRR_{max} [MW]	*ln*A [m^2]	s [%]
Mean	3.9728	4.0924	0.0000
Mode	3.4012	3.5553	0.0000
Standard deviation	0.4955	0.3208	2.4598
Minimum	3.4012	3.5553	-4.0000
Maximum	4.6052	4.5850	4.0000

4.4.1.2. Data

The data used to develop the proposed predictive models are obtained by 120 simulations. Specifically, these data consist of the simulated values of the dependent variables (*Y*), namely:

- Maximum spalling depth: Y_1;
- Spalling start time: Y_2;
- Maximum spalling length: Y_3.

Table 4.2 shows the summary statistic of the simulated data both beneath the ceiling and along the right wall.

Table 4.2. Summary statistic of simulated data.

Statistic	Y_1 [cm]	Y_2 [min]	Y_3 [m]
Ceiling			
Mean	4.2009	10.5638	21.4877
Mode	1.5489	7.2500	0.0000
Standard deviation	2.0719	5.1918	15.8920
Minimum	0.5984	6.1333	0.0000
Maximum	7.9103	35.6500	62.0000
Right wall			
Mean	5.4470	10.2781	15.6985
Mode	1.8171	6.1000	11.0000
Standard deviation	3.1075	4.0955	8.5966
Minimum	1.3862	5.1667	3.0000
Maximum	13.1199	19.3500	39.0000
Total simulations		120	

4.5. Goodness-of-fit

The Normalized Root Mean Square Error (NRMSE) is applied in order to test the goodness-of-fit of the developed predictive models. The NRMSE is defined as follows (*Jiang et al., 2021*):

$$(4.2)\ \mathrm{NRMSE} = \left(\frac{\sqrt{\sum_{n=1}^{N} (S_n - M_n)^2}}{N} \times \frac{1}{\bar{M}} \right) \times 100,$$

where S_n is the n-th predicted value, M_n is the n-th simulated value, N = 120 is the total number of simulated values, and $\overline{M}$ is the mean of the simulated values.

The predictive capabilities, in terms of NRMSE, of the proposed models are evaluated according to Table 4.3 (*Jamieson et al., 1991; Jiang et al., 2021*). In general, models with small NRMSE values (i.e., NRMSE ≤ 20%) show *good* prediction capabilities.

Table 4.3. Predictive capabilities of a model in terms of Normalized Root Mean Square Error (NRMSE).

Prediction	Normalized Root Mean Square Error (NRMSE)
Excellent	NRMSE ≤ 10%
Good	10% < NRMSE ≤ 20%
Fair	20% < NRMSE ≤ 30%
Poor	NRMSE > 30%

4.6. Analysis and discussion of results

The main scope of this thesis is to develop predictive models, namely an analytical method, capable of estimating the maximum spalling depth, the spalling start time, and the maximum spalling length as a function of certain variables (i.e., v, HRR_{max}, A, and s) both beneath the ceiling and along the right wall, which are the concrete elements most susceptible to spalling due to their reduced distance from the burning vehicle.

It is worth remembering that in this thesis spalling is assumed to occur only where (and when) fire-induced damage affects the concrete for a depth of at least 0.005 m.

4.6.1. Ceiling

4.6.1.1. Maximum spalling depth

The predictive model developed in order to estimate the expected value of the maximum spalling depth beneath the ceiling (λ_{1c}) is:

(4.3) $\lambda_{1c} = e^{(-2.065\ +\ ln\mathrm{HRR}_{\mathrm{max}}*0.846\ +\ ln\mathrm{A}*0.014\ -\ \mathrm{v}*0.896\ +\ \mathrm{s}*0.007)}$,

where λ_{1c} is expressed in cm, $\mathrm{HRR}_{\mathrm{max}}$ is the maximum heat release rate [MW], A is the tunnel cross-section area [m^2], v is a dummy variable (v = 1 if there is a mechanical ventilation system, 0 otherwise), and s is the longitudinal slope of the tunnel [%].

The NRMSE found for this predictive model is about 17%, which means, according to Table 4.3, that it offers a *good* prediction. In this respect, Fig. 4.11 shows the relationship between the simulated and predicted values of the maximum spalling depth beneath the ceiling.

From Fig. 4.11 one can see that the simulated and predicted values of the maximum spalling depth beneath the ceiling are quite aligned along the bisector line. This confirms, also graphically, that the model proposed to predict λ_{1c} provides *good* results.

For example, with reference to the case of a 100 MW fire in a flat tunnel of 10.5 x 6 m^2 (width x height) equipped with a mechanical ventilation system (i.e., 100_10.5x6_5_0), the maximum simulated spalling depth was found to be 2.81 cm, while the predicted one was 2.7 cm. On this basis, the difference between the simulated and predicted values was about 4% for the investigated case.

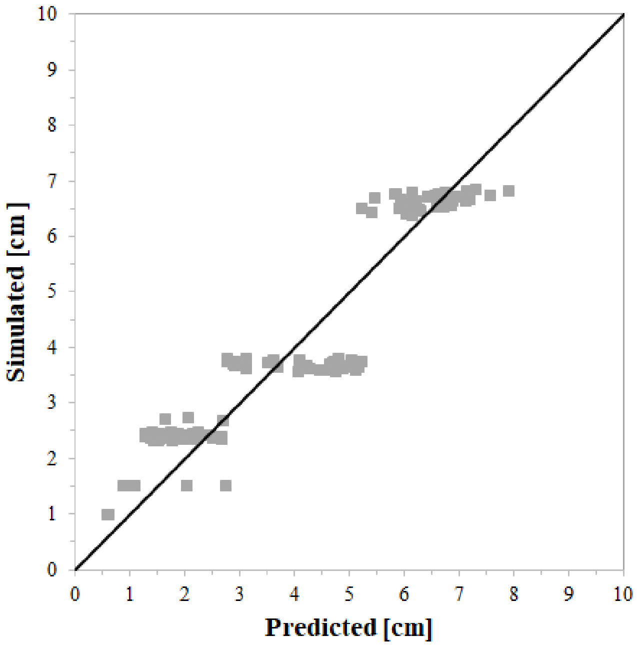

Fig. 4.11. Relationship between the simulated and predicted values of the maximum spalling depth beneath the ceiling.

4.6.1.2. Spalling start time

The predictive model proposed in order to assess the expected value of the spalling start time beneath the ceiling (λ_{2c}) is:

(4.4) $\lambda_{2c} = e^{(4.854 - \mathit{ln}\mathrm{HRR}_{\mathrm{max}} * 0.781 \,+\, \mathit{ln}\mathrm{A} * 0.134 + \,\mathrm{v} * 0.643 \,+\, \mathrm{s} * 0.00007)}$,

where λ_{2c} is expressed in min, $\mathrm{HRR}_{\mathrm{max}}$ is the maximum heat release rate [MW], A is the tunnel cross-section area [m^2], v is a dummy variable (v = 1 if there is a mechanical ventilation system, 0 otherwise), and s is the longitudinal slope of the tunnel [%].

The NRMSE found for this predictive model is about 19%, which means, according to Table 4.3, that it still provides a *good* prediction. In this regard, Fig. 4.12 reports the relationship between the simulated and predicted values of the spalling start time beneath the ceiling.

From Fig. 4.12 it is possible to observe that the simulated and predicted values of the spalling start time beneath the ceiling are fairly aligned along the bisector line. This confirms, also graphically, that the model developed to predict λ_{2c} offers *good* findings.

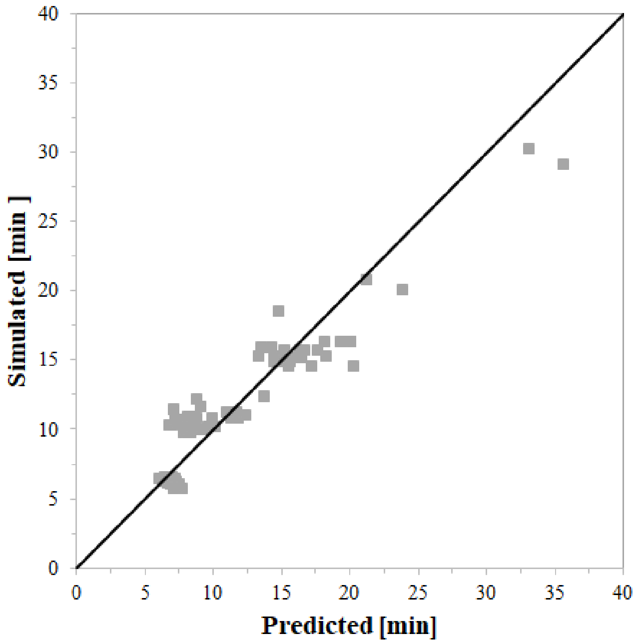

Fig. 4.12. Relationship between the simulated and predicted values of the spalling start time beneath the ceiling.

For example, with reference to the case of a 100 MW fire in a flat tunnel of 10.5 x 6 m^2 (width x height) equipped with a mechanical ventilation system (i.e., 100_10.5x6_5_0), the simulated spalling start time was found to be 9.1 min, while the predicted one was 11.6 min. As a result, the difference between the simulated and predicted values was about 20% for the investigated case.

4.6.1.3. Maximum spalling length

The predictive model developed in order to estimate the expected value of the maximum spalling length beneath the ceiling (λ_{3c}) is:

$$(4.5)\ \lambda_{3c} = e^{(1.324\ +\ ln\mathrm{HRR}_{\mathrm{max}}*1.239-\ ln\mathrm{A}*0.795\ -\ \mathrm{v}*1.959-\ \mathrm{s}*0.025)},$$

where λ_{3c} is expressed in m, $\mathrm{HRR}_{\mathrm{max}}$ is the maximum heat release rate [MW], A is the tunnel cross-section area [m^2], v is a dummy variable (v = 1 if there is a mechanical ventilation system, 0 otherwise), and s is the longitudinal slope of the tunnel [%].

The NRMSE found for this predictive model is about 9%, which means, according to Table 4.3, that it offers an *excellent* prediction. In this respect, Fig. 4.13 shows the relationship between the simulated and predicted values of the maximum spalling length beneath the ceiling.

From Fig. 4.13 one can see that the simulated and predicted values of the maximum spalling length beneath the ceiling are very well aligned along the bisector line. This confirms, also graphically, that the model proposed to predict λ_{3c} provides *excellent* results.

For example, with reference to the case of a 100 MW fire in a flat tunnel of 10.5 x 6 m^2 (width x height) equipped with a mechanical ventilation system (i.e., 100_10.5x6_5_0), the maximum simulated spalling length was found to be 6.5 m, while the predicted one was 6 m. On this basis, the difference between the simulated and predicted values was about 8% for the investigated case.

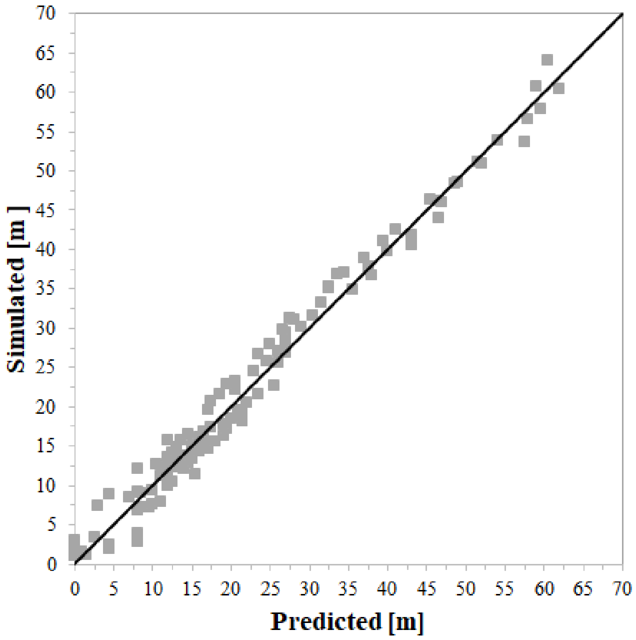

Fig. 4.13. Relationship between the simulated and predicted values of the maximum spalling length beneath the ceiling.

Summing up, the predictive models developed in order to estimate the expected value of the maximum spalling depth and the spalling start time beneath the ceiling provided *good* predictions, which become *excellent* with reference to the maximum spalling length.

4.6.2. Right wall

4.6.2.1. Maximum spalling depth

The predictive model developed in order to estimate the expected value of the maximum spalling depth along the right wall (λ_{1w}) is:

$$(4.6)\ \lambda_{1w} = e^{(-4.15\ +\ ln\mathrm{HRR}_{\mathrm{max}}*1.105\ +\ ln\mathrm{A}*0.311\ +\ \mathrm{v}*0.182\ +\ \mathrm{s}*0.008)},$$

where λ_{1w} is expressed in cm, $\mathrm{HRR_{max}}$ is the maximum heat release rate [MW], A is the tunnel cross-section area [m^2], v is a dummy variable (v = 1 if there is a mechanical ventilation system, 0 otherwise), and s is the longitudinal slope of the tunnel [%].

The NRMSE found for this predictive model is about 16%, which means, according to Table 4.3, that it offers a *good* prediction. In this respect, Fig. 4.14 shows the relationship between the simulated and predicted values of the maximum spalling depth along the right wall.

From Fig. 4.14 one can see that the simulated and predicted values of the maximum spalling depth on the right wall are quite aligned along the bisector line. This confirms, also graphically, that the model proposed to predict λ_{1w} provides *good* results.

For example, with reference to the case of a 100 MW fire in a flat tunnel of 10.5 x 6 m^2 (width x height) equipped with a mechanical ventilation system (i.e., 100_10.5x6_5_0), the maximum simulated spalling depth was found to be 11.87 cm, while the predicted one was 11.12 cm. On this basis, the difference between the simulated and predicted values was about 6% for the investigated case.

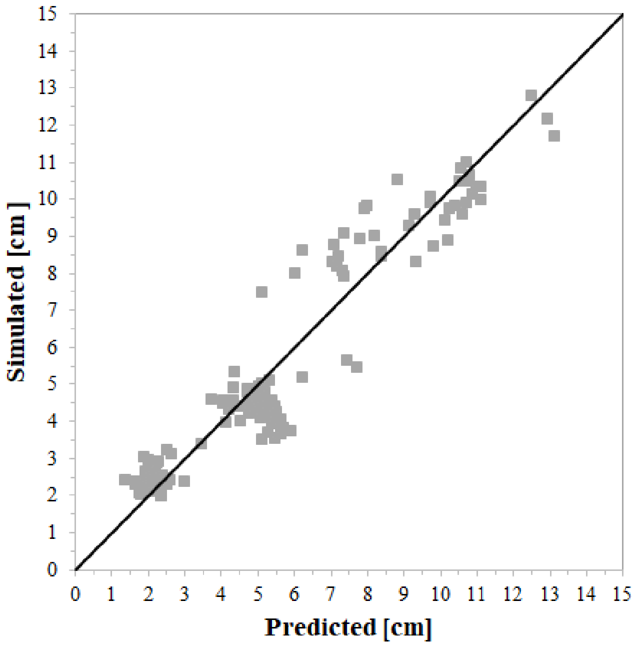

Fig. 4.14. Relationship between the simulated and predicted values of the maximum spalling depth along the right wall.

4.6.2.2. Spalling start time

The predictive model proposed in order to assess the expected value of the spalling start time along the right wall (λ_{2w}) is:

(4.7) $\lambda_{2w} = e^{(6.158 - \ln HRR_{max}*0.710 - \ln A*0.249 - v*0.137 - s*0.002)}$,

where λ_{2w} is expressed in min, HRR_{max} is the maximum heat release rate [MW], A is the tunnel cross-section area [m^2], v is a dummy variable (v = 1 if there is a mechanical ventilation system, 0 otherwise), and s is the longitudinal slope of the tunnel [%].

The NRMSE found for this predictive model is about 10%, which means, according to Table 4.3, that it provides an *excellent* prediction. In this regard, Fig. 4.15 reports the relationship between the simulated and predicted values of the spalling start time along the right wall.

From Fig. 4.15 it is possible to observe that the simulated and predicted values of the spalling start time on the right wall are well aligned along the bisector line. This confirms, also graphically, that the model developed to predict λ_{2w} offers *excellent* findings.

For example, with reference to the case of a 100 MW fire in a flat tunnel of 10.5 x 6 m^2 (width x height) equipped with a mechanical ventilation system (i.e., 100_10.5x6_5_0), the simulated spalling start time was found to be 5.3 min, while the predicted one was 5.6 min. As a result, the difference between the simulated and predicted values was about 5% for the investigated case.

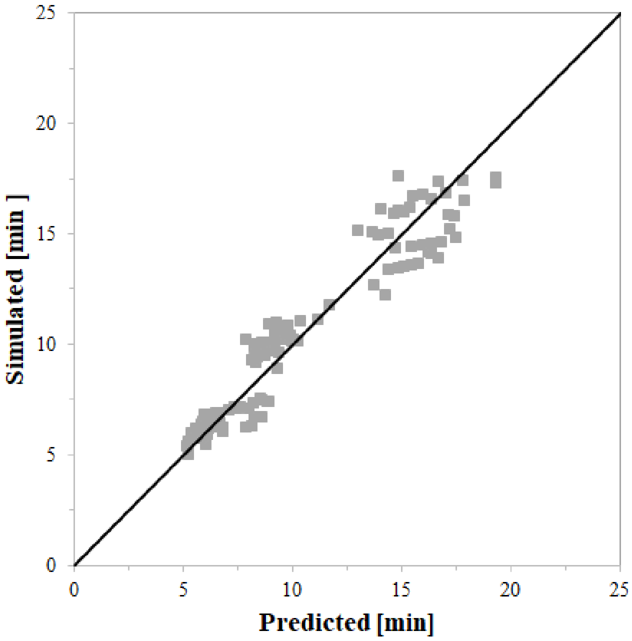

Fig. 4.15. Relationship between the simulated and predicted values of the spalling start time along the right wall.

4.6.2.3. Maximum spalling length

The predictive model developed in order to estimate the expected value of the maximum spalling length along the right wall (λ_{3w}) is:

$$(4.8)\ \lambda_{3w} = e^{(1.085\ +\ ln\mathrm{HRR_{max}}*1.008\ -\ ln\mathrm{A}*0.533\ -\ \mathrm{v}*0.819\ -\ \mathrm{s}*0.022)},$$

where λ_{3w} is expressed in m, $\mathrm{HRR_{max}}$ is the maximum heat release rate [MW], A is the tunnel cross-section area [m^2], v is a dummy variable (v = 1 if there is a mechanical ventilation system, 0 otherwise), and s is the longitudinal slope of the tunnel [%].

The NRMSE found for this predictive model is about 10%, which means, according to Table 4.3, that it offers an *excellent* prediction. In this respect, Fig. 4.16 shows the relationship between the simulated and predicted values of the maximum spalling length along the right wall.

From Fig. 4.16 one can see that the simulated and predicted values of the maximum spalling length on the right wall are very well aligned along the bisector line. This confirms, also graphically, that the model proposed to predict λ_{3w} provides *excellent* results.

For example, with reference to the case of a 100 MW fire in a flat tunnel of 10.5 x 6 m^2 (width x height) equipped with a mechanical ventilation system (i.e., 100_10.5x6_5_0), the maximum simulated spalling length was found to be 14 m, while the predicted one was 14.9 m. On this basis, the difference between the simulated and predicted values was about 6% for the investigated case.

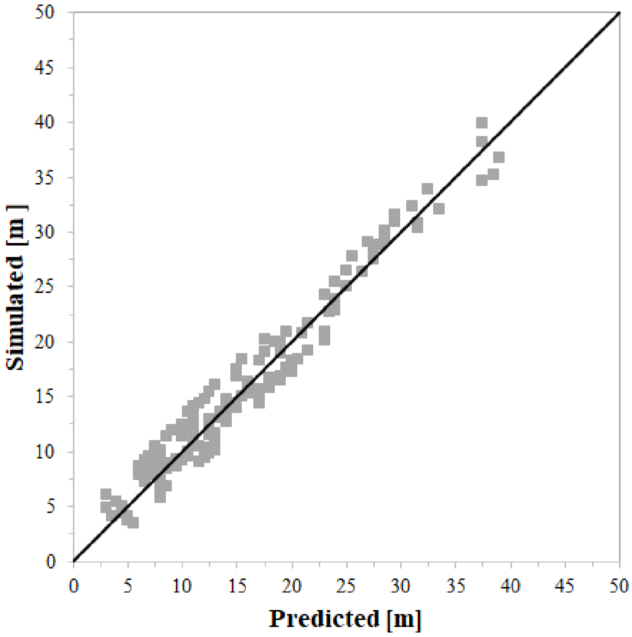

Fig. 4.16. Relationship between the simulated and predicted values of the maximum spalling length along the right wall.

Summing up, the predictive models proposed in order to assess the expected value of the spalling start time and the maximum spalling length along the right wall provided *excellent* predictions, which become *good* with reference to the maximum spalling depth.

4.7. Conclusions

This research was prevalently motivated by the need to develop certain predictive models, namely an analytical method, capable of evaluating the maximum spalling depth, the spalling start time, and the maximum spalling length both beneath the ceiling and along the right wall, which, given the position of the burning vehicle, were the concrete elements more susceptible to spalling. In particular, these predictive models, based on the proposed 3D CFD model, were developed on the basis of some assumptions and preliminary simulations aimed at identifying the set of the independent variables that most affect fire-induced damage. In this respect, the longitudinal ventilation (i.e., v = 5 m/s and 0.5 m/s), the maximum heat release rate (i.e., HRR_{max} = 30 MW, 50 MW, and 100 MW), the tunnel width (i.e., W = 7 m, 10.5 m, and 14 m), the tunnel height (i.e., H = 5 m, 6 m, and 7 m), and the longitudinal slope (i.e., s = 0% for v = 5 m/s, while s = -4%, -2%, 0%, 2%, and 4% when v = 0.5 m/s) were found to be the variables with the greatest impact on spalling. As a result, they were assumed to be the independent variables of the proposed predictive models.

The data used in order to set up the developed analytical method were obtained by running 120 simulations, which were some of all possible combinations of the values that could take the cited independent variables.

Finally, the Normalized Root Mean Square Error (NRMSE) was applied in order to test the goodness-of-fit of the developed predictive models.

On the basis of the aforementioned considerations, it is possible to draw the following conclusions.

With reference to the ceiling, the proposed predictive models provided *good* predictions for both the maximum spalling depth and the spalling start time, which became *excellent* for the maximum spalling length. In this regard, the NRMSE was found to be about 17%, 19%, and 9% for the maximum spalling depth, the spalling start time, and the maximum spalling length, respectively.

With reference to the right wall, instead, the developed predictive models offered *good* predictions for the maximum spalling depth, which became *excellent* for both the spalling start time and the maximum spalling length. In this regard, the NRMSE was found to be about 16%, 10%, and 10% for the maximum spalling depth, the spalling start time, and the maximum spalling length, respectively.

Therefore, the author is confident that the proposed analytical method represents an important advancement of knowledge, given the lacuna, in the field of tunnel fire safety engineering. In fact, the results obtainable from these predictive models would be useful not only to the international scientific community but also to both road engineers and Tunnel Management Agencies (TMAs) to estimate how fire-induced damage varies with longitudinal ventilation, maximum heat release rate, tunnel cross-section area, and longitudinal slope.

4.8. References

[81] ANAS, 2009. Linee Guida per la Progettazione Della Sicurezza nelle Gallerie Stradali Secondo la Normativa Vigente. Circolare n°179431/2009. Available online: https://www.stradeanas.it/sites/default/files/pdf/Linee_guida_sicurezza_gallerie_2009.pdf (accessed on 13 October 2021).

[82] Astarita, V., Caliendo, C., Giofrè, V.P., Russo, I., 2020. Surrogate safety measures from traffic simulation: Validation of safety indicators with intersection traffic crash data. Sustainability 12, 4974, doi:10.3390/su12176974.

[83] Caliendo, C., Ciambelli, P., De Guglielmo, M.L., Meo, M.G., Russo, P., 2013. Simulation of fire scenarios due to different vehicle types with and without traffic in a bi-directional road tunnel. Tunnelling and Underground Space Technology 37, 22–36.

[84] Caliendo, C., De Guglielmo, M.L., Russo, I., 2019. Analysis of crash frequency in motorway tunnels based on a correlated random-parameters approach. Tunnelling and Underground Space Technology 85, 243-251.

[85] Caliendo, C., Guida, M., Postiglione, F., Russo, I., 2021. A Bayesian bivariate hierarchical model with correlated parameters for the analysis of road crashes in Italian tunnels. Statistical Methods and Applications, doi:10.1007/s10260-021-00567-5. Available online: https://link.springer.com/article/10.1007/s10260-021-00567-5 (accessed on 11 October 2021).

[86] Greene, W., 2007. LIMDEP Version 9.0. Econometric Software Inc., Plainview, NY.

[87] ITA-International Tunneling Association, 2004. Guidelines for Structural Fire Resistance for Road Tunnels. Working Group No. 6 Maintenance and Repair.

[88] Jamieson, P.D., Porter, J.R., Wilson, D.R., 1991. A test of the computer simulation model ARC-WHEAT1 on wheat crops grown in New Zealand. Field Crops Research 27, 337-350.

[89] Jiang, X.P., Chen, R.Y., Xu, Z.S., Yang, X.L., 2011. Experiment Research on Smoke Temperature Properties Lower Ceiling along Tunnel at Different Longitudinal Ventilation Velocities and Tunnel Slopes. Geotechnical Special Publication 221, 105-112, doi: 10.1061/47632(411)14.

[90] Jiang, R., He, W., He, L., Yang, J.Y., Qian, B., Zhou, W., He, P., 2021. Modeling adaptation strategies to reduce adverse impacts of climate change on maize cropping system in Northeast China. Scientific Reports 11, 810, https://doi.org/10.1038/s41598-020-79988-3.

[91] Khoury, G.A., 2000. Effect of fire on concrete and concrete structures. Progress in Structural Engineering and Materials 2 (4), 429-447.

[92] PIARC, 2001. Maintained headroom. Available online: https://tunnels.piarc.org/sites/tunnels/files/public/wysiwyg/import/Chapters%20PIARC%20reports/2001%2005.11.B%20Chap%207%20EN.pdf (accessed on 13 October 2021).

[93] PIARC, 2007. Systems and Equipment for Fire and Smoke Control in Road Tunnels. PIARC Technical Committee C5 Road Tunnel. <http://www.piarc.org>.

Chapter 5

Passive fire protection systems

5.1. Introduction

As the name suggests, Passive Fire Protection (PFP) systems remain inactive in the tunnel until a fire occurs. The main scope of PFP systems in the event of a tunnel fire is to try to contain the fire and/or slow down its spread in order to keep the temperature of the concrete elements below the critical temperature, thus preventing spalling.

The PFP systems used in this work in order to mitigate spalling consist of some of the most widely applied coatings for tunnel fire protection worldwide. The potential of each of these coatings is assessed using the 3D CFD model presented in Chapter 3. Then, based on the criterion of the ratio between thermal performance and application thickness, appropriate comparisons are made between the results found for the different coatings used.

5.2. Assumptions

Coatings used in order to prevent or mitigate spalling are applied to the walls and ceiling on their side exposed to fire. In this regard, the thermal performance of these coatings is evaluated using the developed 3D CFD model, considering the tunnel and the fire scenario described in Chapter 3.

Coatings are assumed to be capable of preventing spalling when the following two conditions are satisfied (*ITA, 2004*):

- The temperature at the interface between concrete and coating is lower than 380 °C;
- The temperature of the steel reinforcement is lower than 250 °C.

Moreover, it is assumed that the adhesion conditions between concrete and coating are always guaranteed. In this respect, it is to be said that the adhesion capacity of a coating to the support is one of the most investigated factors during fire resistance tests of PFP systems. This means that it is carefully verified before the product is made available on the market.

Finally, it is to be stressed that the properties of PFP systems are assumed to be constant with temperature.

5.3. Coatings description

The passive fire protection systems used in the present thesis are among the most widely applied for the fire protection of tunnels and their efficiency is recognized worldwide.

In order to prevent spalling, the following types of coatings are used:

- Cement-based mortars;

- Panels;
- Intumescent paint.

These thermal-insulation materials are chosen among the others available on the market because they can be applied in thin layers. In this regard, it is to be said that the linings lead to an increase in the load acting on the structure due to their weight, as well as a reduction in the internal volume of the tunnel. These problems arise more especially in the case of existing tunnels that need to be adapted to the current directives on tunnel safety design.

In the present thesis, in the light of the above considerations, the cement-based mortars and panels are applied in a 3 cm layer on both the walls and the ceiling, while the intumescent paint forms a 1.5 mm thick film on the same concrete elements.

5.3.1. Cement-based mortars

Three different types of cement-based mortars are used:

- Fire Barrier 135;
- Fendolite M II;
- PST System.

In this study, each of these coatings is applied in a 3 cm layer on both the walls and the ceiling of the investigated tunnel.

5.3.1.1. Fire Barrier 135

Fire Barrier 135 is a cement-based mortar designed to provide fire protection for different types of structures, including tunnels. This product can be applied with spray equipment when mixed with water; in addition, its high adhesion capacity leads to a very low wastage of material during spray applications (*CETU, 2010*).

The fire resistance of Fire Barrier 135 was tested against the ISO-834 (peak temperature of 1050 °C and 1160 °C after 2 hours and 4 hours from the test start, respectively), RWS, and HC_{mod} fire curves (see 1.1.1.2).

Fire Barrier 135 is characterized by the following properties (*CETU, 2010*), which are assumed to be temperature-independent:

- Thermal conductivity (λ) is 0.187 W/(mK);
- Specific heat (c) is 0.95 kJ/(kgK);
- Emissivity (ε) is 0.9;
- Density (ρ) is 1550 kg/m^3.

5.3.1.2. Fendolite M II

Fendolite M II is a mortar based on Portland cement and vermiculite. It is a low-density sprayed product, suitable for resisting rapid temperature variations. Fendolite M II can be used in many types of structures, including tunnels (*CETU, 2010*).

The fire resistance of Fendolite M II was tested using the RWS and HC_{mod} fire curves.

Fendolite M II is characterized by the following properties (*CETU, 2010*), which are assumed to be constant with temperature:

- Thermal conductivity is 0.19 W/(mK);
- Specific heat is 0.97 kJ/(kgK);
- Emissivity is 0.9;

- Density is 755 kg/m^3.

5.3.1.3. PST System

PST system includes an insulating coat and a hardening agent. The former is cement-based, while the hardening agent involves steel particles. This coating can be applied with spray equipment to different types of structures, including tunnels (*CETU, 2010*).

The fire retardancy of the PST system is based on two overlapping phenomena:

- The insulating effect is due to the reduced thermal conductivity of the coating, which is stable above 1300 °C and does not release toxic fumes.
- The hardener vitrifies from 800 °C and provides a stable shield above 1400 °C that reflects much of the thermal radiation.

The fire resistance of this coating was tested using the RWS fire curve.

PST system is characterized by the following properties (*CETU, 2010*), which are assumed to be temperature-independent:

- Thermal conductivity is 0.14 W/(mK);
- Specific heat is 1.05 kJ/(kgK);
- Emissivity is 0.9;
- Density is 800 kg/m^3.

5.3.2. Panels

5.3.2.1. Promatect H

Promatect H is a cement-based calcium silicate insulation panel. It is also commonly used for structures such as tunnels.

The fire resistance of this coating was tested against the RWS fire curve.

Promatect H is characterized by the following properties (*Li and Ingason, 2018*), which are assumed to be constant with temperature:

- Thermal conductivity is 0.19 W/(mK);
- Specific heat is 1.13 kJ/(kgK);
- Emissivity is 0.9;
- Density is 870 kg/m^3.

In the present study, these panels are applied in a 3 cm layer on both the walls and the ceiling of the investigated tunnel.

5.3.3. Intumescent paint

Intumescent paints are usually applied to protect steel structures from fire; however, in the last years, they have also been more and more used for concrete structures. In contrast to other types of coatings, an intumescent paint can be applied in very thin films (i.e., on the order of a few millimeters), which, when heated, can expand up to one hundred times its initial thickness, forming a carbonaceous char layer that protects concrete from high temperatures. In this study, therefore, the intumescent paint is applied in a 1.5 mm layer on both the walls and the ceiling of the investigated tunnel.

Different parameters must be set in the FDS code in order to describe the swelling reaction of the intumescent paint. The list of these parameters is reported below and the value of each of them is taken from *Gillet et al. (2019)*:

- Carbonization temperature (θ_{car}) is 280 °C;
- Thermal conductivity is 0.08 W/(mK) if $T \geq \theta_{car}$; otherwise, it is 0.12 W/(mK);
- Specific heat is 1 kJ/(kgK) if $T \geq \theta_{car}$; otherwise, it is 1.9 kJ/(kgK);
- Initial density is 1000 kg/m^3;
- Final density (ρ_f) is 50 kg/m^3;
- Emissivity is 0.9;
- Initial thickness (d) is 1.5 mm;
- Pre-exponential factor (A_{pre}) is 2×10^{12} 1/s;
- Activation energy (E) is 1.5×10^5 is J/mol;
- Heat of reaction (H_{rea}) is 500 kJ/kg.

Table 5.1 summarizes the properties of each coating used in this study in order to prevent or mitigate fire-induced damage. It is to be stressed that some of the parameters shown in Table 5.1 are only defined with respect to the intumescent paint because they describe the swelling process of this coating.

Table 5.1. Coatings properties.

Coatings	**λ** [W/(mK)]	**c** [kJ/(kgK)]	**ρ** [kg/m^3]	**ε** [-]	**d** [mm]	**ρ_f** [kg/m^3]	**θ_{car}** [°C]	**A_{pre}** [1/s]	**E** [J/mol]	**H_{rea}** [kJ/kg]
Cement-based mortar										
Fire Barrier 135	0.187	0.95	1550	0.9	30	-	-	-	-	-
Fendolite M II	0.190	0.97	775	0.9	30	-	-	-	-	-
PST System	0.140	1.05	800	0.9	30	-	-	-	-	-
Panel										
Promatect H	0.190	1.13	870	0.9	30	-	-	-	-	-
Intumescent paint	0.12 if $T < \theta_{car}$ 0.08 if $T \geq \theta_{car}$	1.9 if $T < \theta_{car}$ 1.0 if $T \geq \theta_{car}$	1000	0.9	1.5	50	280	2×10^{12}	1.5×10^{5}	500

5.4. Analysis and discussion of results

In order to prevent fire-induced damage, certain coatings such as cement-based mortars (i.e., Fire Barrier 135, Fendolite M II, and PST System), panels (i.e., Promatect H), and an intumescent paint are used. The first two are applied in a 3 cm layer on both the walls and the ceiling, while the intumescent paint forms a 1.5 mm thick film on the same concrete elements.

As mentioned in Chapter 3, the concrete elements most susceptible to spalling are the ceiling and the right wall, which, given the position of the burning vehicle, are closer to the fire source than the left wall.

In the light of the above considerations, the following results concern the evaluation of the effectiveness of the above coatings, applied to both the ceiling and the right wall, to prevent spalling. In addition, these results refer to a time t = 120 min from the fire start.

5.4.1. Ceiling

The results are always referred to point A where the peak spalling depth beneath the ceiling was measured.

First of all, it is to be said that the intumescent paint, due to the high temperatures, expanded up to about 26 mm after a fire exposure time of 120 min. Specifically, the swelling of this intumescent paint started when the coating surface temperature reached approximately 310 °C, namely after 3.7 min from the fire start. On this basis, it is to be stressed that the thermal performance of the investigated coatings is directly comparable to each other because all PFP systems used in this work have a thickness of about 0.03 m after 120 min of fire exposure.

Fig. 5.1 shows the temperature profiles within the thickness of the ceiling as a function of the coating type.

From Fig. 5.1 it is possible to observe that each PFP system is able to prevent fire-induced damage. In fact, Fig. 5.1 shows that the temperature at the interface (i.e., depth = 0) between concrete and coating is below 380 °C with reference to all PFP systems. The temperature of the steel reinforcement, which is usually located at a depth of 0.05 m from the aforementioned interface surface, is also lower than the corresponding threshold value of 250 °C for all coatings.

From Fig. 5.1 one can also see that Fire Barrier 135, Fendolite M II, and Promatect H offered similar thermal performance to each other. In this regard, the temperature at the interface between concrete and coating is about 250-280 °C, while the temperature of steel rebars (depth = 0.05 m) is approximately 100 °C. However, better thermal performance is obtained using PST system, probably due to its lower thermal conductivity. Using PST system, in fact, the temperature at the interface between concrete and coating is about 202 °C, while the steel reinforcement temperature is approximately 87 °C. In this respect, it is to be said that the thermal performance provided by the intumescent paint is very similar to those obtained using PST system, even though the former is applied with a much lower thickness.

Therefore, based on the criterion of the ratio between thermal performance and application thickness, the best insulation-material used in this study was the intumescent paint.

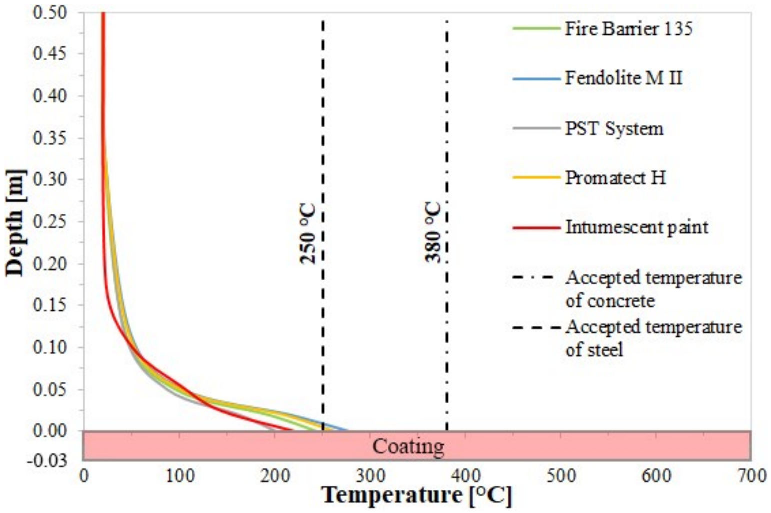

Fig. 5.1. Point A. Temperature profiles within the thickness of the ceiling as a function of the coating type; t = 120 min.

5.4.2. Right wall

The results are always related to point B where the maximum spalling depth along the right wall was measured.

Fig. 5.2 shows the temperature profiles within the thickness of the right wall as a function of the coating type.

Along the right wall, the intumescent paint, due to the high temperatures, expanded up to approximately 27 mm after a fire exposure time of 120 min. In particular, the swelling of this intumescent paint started when the coating surface temperature reached about 310 °C, namely after 2.3 min from the fire start. As a result, the thermal performance of all coatings is directly comparable to each other also along the right wall.

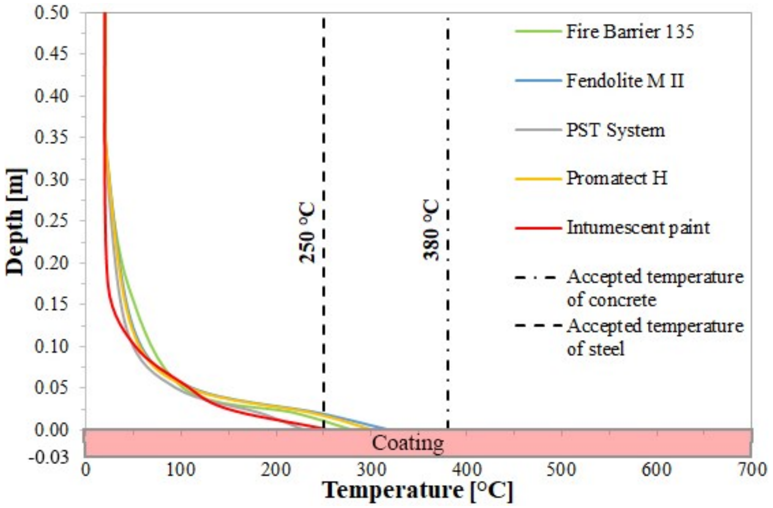

Fig. 5.2. Point B. Temperature profiles within the thickness of the right wall as a function of the coating type; t = 120 min.

From Fig. 5.2 it is possible to observe that each PFP system is able to prevent fire-induced damage also along the right wall. In fact, Fig. 5.2 shows that the temperature at the interface (i.e., depth = 0) between concrete and coating is below 380 °C for all PFP systems. The temperature of the steel reinforcement, which is generally located at a depth of 0.05 m from the above-mentioned interface surface, is also below the corresponding threshold value of 250 °C with reference to all coatings.

From Fig. 5.2 one can also see that Fire Barrier 135, Fendolite M II, and Promatect H offered similar thermal performance to each other also along the right wall. In this respect, the temperature at the interface between concrete and coating is about 280-320 °C, while the temperature of steel rebars (depth = 0.05 m) is approximately 110 °C. However, better thermal performance is still obtained using PST system, probably due to its lower thermal conductivity. Using PST system, in fact, the temperature at the interface between concrete and coating is about 230 °C, while the steel reinforcement temperature is approximately 94 °C. In this regard, it is to be stressed that the thermal performance provided by the intumescent paint is very similar to those obtained by using PST system, even though the former is applied with a much lower thickness.

Therefore, based on the criterion of the ratio between thermal performance and application thickness, the best insulation-material used in this study was the intumescent paint also along the right wall.

It is to be stressed that the fact that the swelling of the intumescent paint was found to be higher along the right wall than beneath the ceiling might be due to the fastest rise in temperatures on the right wall (see Section 3.6.2.1). On this basis, in fact, the temperature at which the swelling starts (i.e., 310 °C) was reached first along the right wall.

5.5. Conclusions

In order to prevent fire-induced damage, certain coating such as cement-based mortars (i.e., Fire Barrier 135, Fendolite M II, and PST System), panels (i.e., Promatect H), and an intumescent paint were used. The first two were applied in a 3 cm layer on both the walls and the ceiling, while the intumescent paint formed a 1.5 mm thick film on the same concrete elements.

The thermal performance of these coatings was evaluated using the developed 3D CFD model, considering the tunnel and the fire scenario described in Chapter 3.

On the basis of the aforementioned considerations, it is possible to draw the following conclusions.

The results showed that the intumescent paint, due to the high temperatures, expanded up to about 26 mm beneath the ceiling and 27 mm along the right wall after a fire exposure time of 120 min. However, the temperature at which the swelling of the intumescent paint started, which was found to be about 310 °C with respect to both concrete elements, was reached quicker along the right wall (i.e., after 2.3 min from the fire start) than beneath the ceiling (i.e., after 3.7 min of fire exposure) probably due to the fastest rise in temperatures measured on the right wall.

All coatings used in this study were able to prevent fire-induced damage both beneath the ceiling and along the right wall. In fact, the temperature at the interface between concrete and coating was always found to be lower than the threshold value for concrete (i.e., 380 °C). The temperature of the steel reinforcement was also below the corresponding threshold value of 250 °C with reference to all coatings.

With reference to both the ceiling and the right wall, Fire Barrier 135, Fendolite M II, and Promatect H offered similar thermal performance to each other. However, better thermal performance was found using PST system and intumescent paint, even though the latter was applied with a much lower thickness.

Therefore, based on the criterion of the ratio between thermal performance and application thickness, the best insulation-material used in this study was the intumescent paint with reference to both the ceiling and the right wall.

5.6. References

[94] CETU-Centre d'etudes des tunnels, 2010. Sprayable mortars for fire protection. Available online: http://www.cetu.developpement-durable.gouv.fr/sprayable-mortars-for-fire-protection-a518.html (accessed on 9 October 2021).

[95] Gillet, M., Perez, L., Autrique, L., 2019. A model based predictive tool for fire safety intumescent coatings design. Fire Safety Journal, 102908.

[96] ITA-International Tunneling Association, 2004. Guidelines for Structural Fire Resistance for Road Tunnels. Working Group No. 6 Maintenance and Repair.

[97] Li, Y.Z, Ingason, H., 2018. Model scale tunnel fire tests on maximum ceiling gas temperature for structural protection. Research Institutes of Sweden, Rapport 2018:58.

Chapter 6

Conclusions

In the light of the background and state of the art, there were at least four main reasons for justifying the research carried out in this thesis.

The first was motivated by the need to develop a new 3D CFD model capable of reproducing the development of a fire in a road tunnel and evaluating the consequent spalling of the concrete elements.

The second was to better investigate the influence of the critical temperature (i.e., the temperature at which spalling might occur) on the severity of fire-induced damage.

The third, which was the main scope of the present thesis, was to develop, based on the above-mentioned 3D CFD model, certain predictive models, namely an analytical method, able to assess fire-induced damage as a function of both the tunnel geometry and the fire scenario.

The fourth was to use 3D CFD modeling for examining and comparing the thermo-insulation performance of certain coatings applied in order to prevent spalling damage.

On this basis, the main conclusions are summarized:

- Since the results obtained from the proposed 3D CFD model had a good level of conformity (an error of no more than 5%) with those provided by a competitive model present in the international literature, it appears reasonable to state that the developed 3D CFD model offers a realistic representation of fire-induced damage in a road tunnel.
- Based on the above-mentioned 3D CFD model, certain predictive models, namely an analytical method, were developed in order to estimate the maximum spalling depth, the spalling start time, and the maximum spalling length as a function of the variables that most affect fire-induced damage, which were found to be the longitudinal ventilation, the maximum heat release rate, the tunnel cross-section area, and the longitudinal slope. According to the values found for the Normalized Root Mean Square Error (NRMSE), which was used in order to test the goodness-of-fit of these predictive models, the proposed analytical method provided a good to excellent prediction of fire-induced damage. Therefore, the author is confident that the developed predictive models represent an important advancement of knowledge, given the lacuna, in the field of tunnel fire safety engineering. In fact, the results obtainable from these predictive

models would be useful not only to the international scientific community but also to both road engineers and Tunnel Management Agencies (TMAs) to estimate how fire-induced damage varies with longitudinal ventilation, maximum heat release rate, tunnel cross-section area, and longitudinal slope. However, it is to be stressed that these predictive models were set up using only data provided by 3D CFD simulations. On this basis, the developed analytical method should be consolidated with the results obtainable from experimental tests carried out both in the laboratory and in situ. This might represent an important development of the presented research.

- Finally, all the investigated coatings (i.e., cement-based mortars, panels, and an intumescent paint) were able to prevent spalling, thus reducing the risk of structural collapse. Specifically, based on the criterion of the ratio between thermal performance and application thickness, the best insulation-material used in this study was the intumescent paint. In the field of passive fire protection systems, which include both coatings and concrete design, future research could focus on the study of fire-resistant concretes, namely concretes designed to resist fire.

Chapter 7

Appendix A

In this Chapter are reported the spalling depth profiles along the length of the right wall obtained from the preliminary simulations performed in Section 4.3.

7.1. Longitudinal ventilation

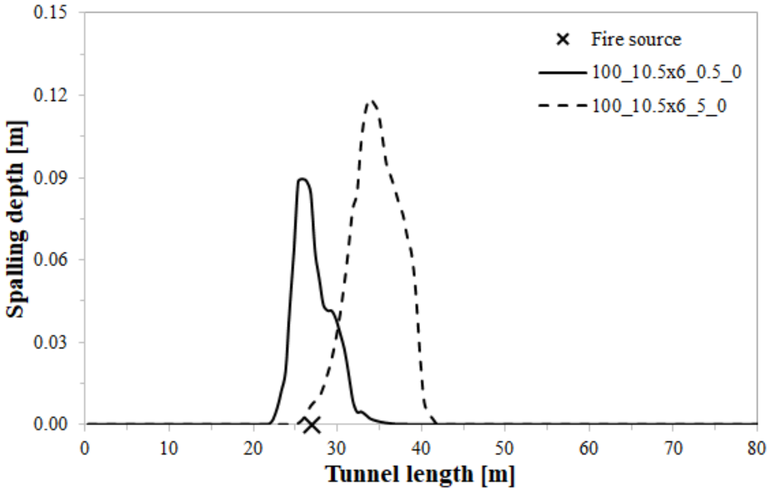

Fig. 7.1. Longitudinal section. Spalling depth profiles predicted along the right wall as a function of the longitudinal ventilation; t = 60 min.

7.2. Maximum HRR

7.2.1. With a mechanical ventilation system

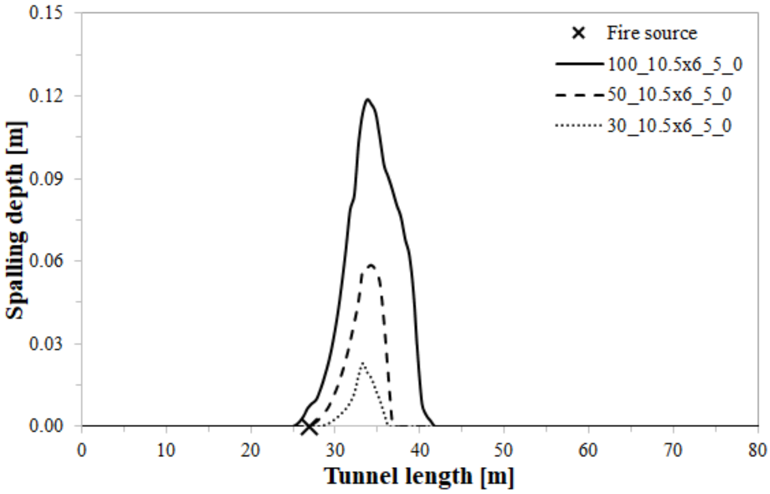

Fig. 7.2. Longitudinal section. Spalling depth profiles predicted along the right wall as a function of the maximum heat release rate; v = 5 m/s and t = 60 min.

7.2.2. Without a mechanical ventilation system

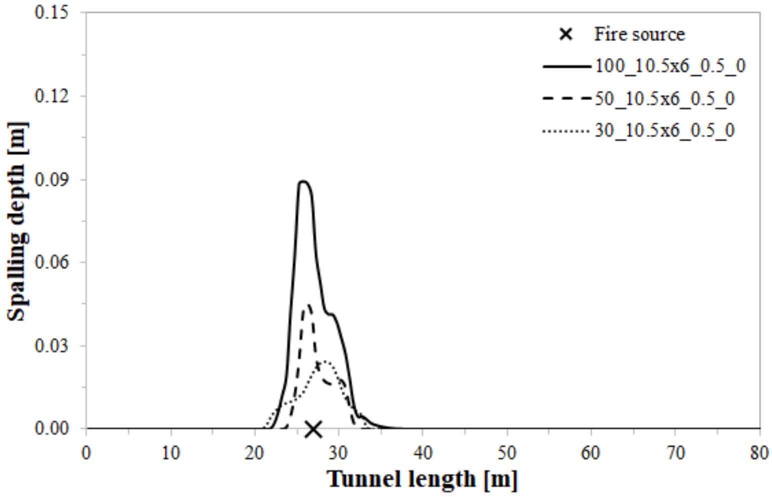

Fig. 7.3. Longitudinal section. Spalling depth profiles predicted along the right wall as a function of the maximum heat release rate; v = 0.5 m/s and t = 60 min.

7.3. Tunnel cross-section area

7.3.1. Tunnel width

7.3.1.1. With a mechanical ventilation system

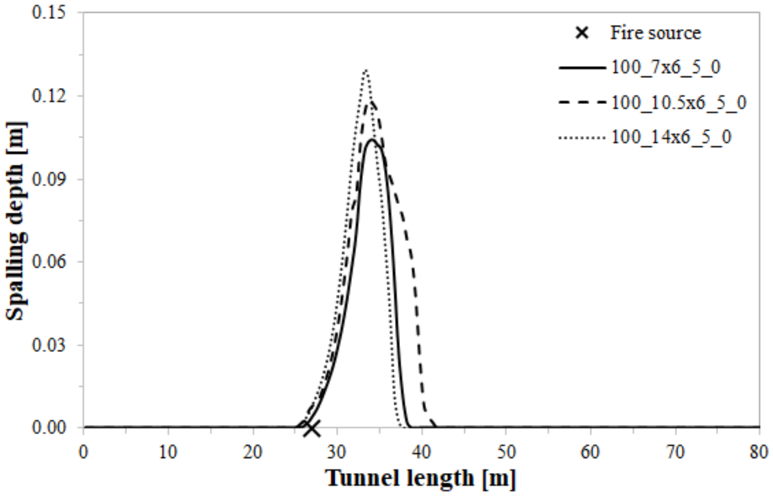

Fig. 7.4. Longitudinal section. Spalling depth profiles predicted along the right wall as a function of the tunnel width; v = 5 m/s and t = 60 min.

7.3.1.2. Without a mechanical ventilation system

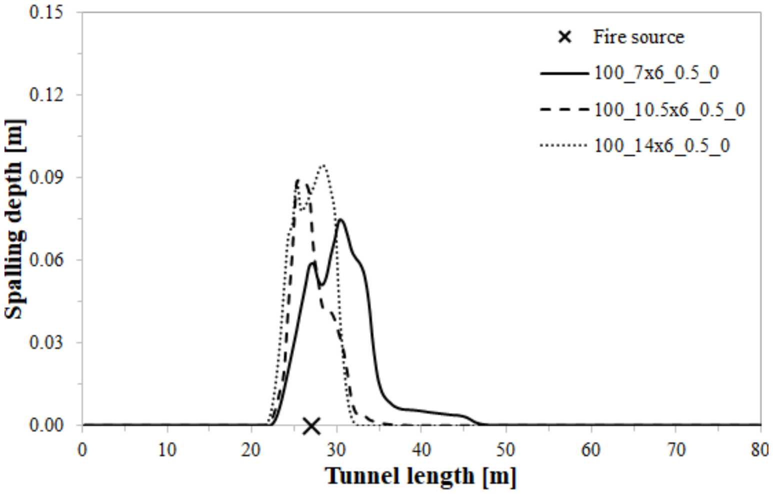

Fig. 7.5. Longitudinal section. Spalling depth profiles predicted along the right wall as a function of the tunnel width; v = 0.5 m/s and t = 60 min.

7.3.2. Tunnel height

7.3.2.1. With a mechanical ventilation system

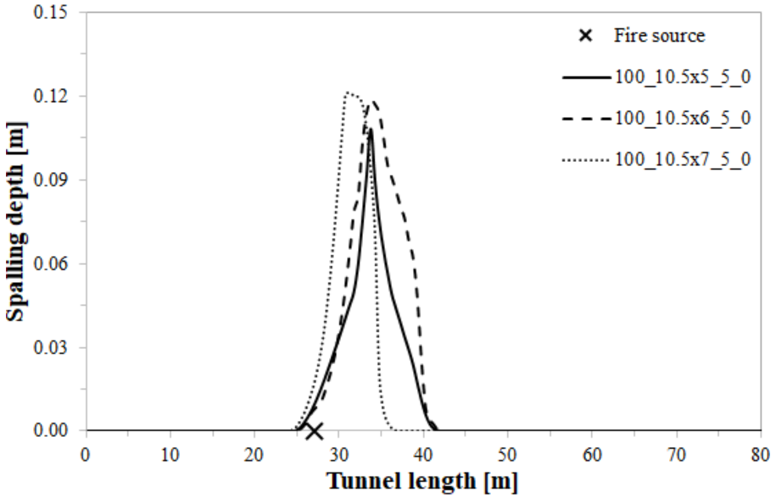

Fig. 7.6. Longitudinal section. Spalling depth profiles predicted along the right wall as a function of the tunnel height; v = 5 m/s and t = 60 min.

7.3.2.2. Without a mechanical ventilation system

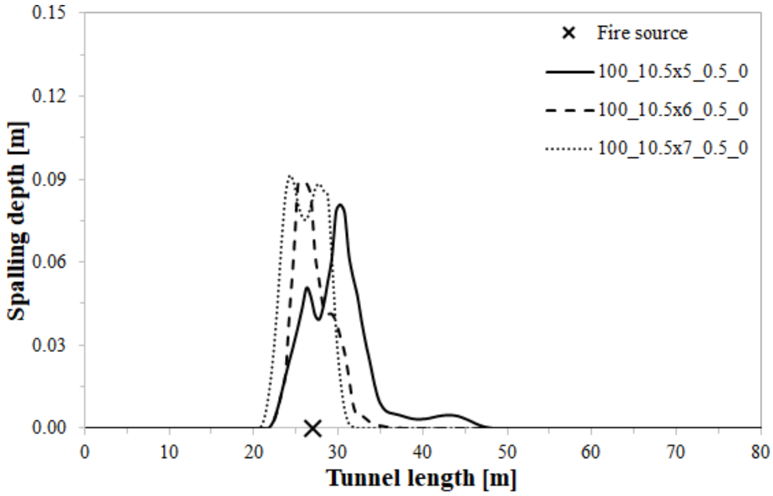

Fig. 7.7. Longitudinal section. Spalling depth profiles predicted along the right wall as a function of the tunnel height; v = 0.5 m/s and t = 60 min.

7.4. Longitudinal slope

7.4.1. With a mechanical ventilation system

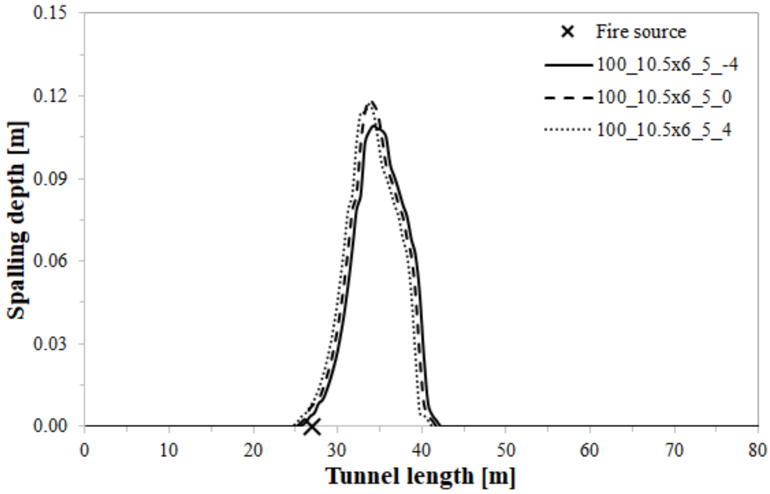

Fig. 7.8. Longitudinal section. Spalling depth profiles predicted along the right wall as a function of the longitudinal slope; v = 5 m/s and t = 60 min.

7.4.2. Without a mechanical ventilation system

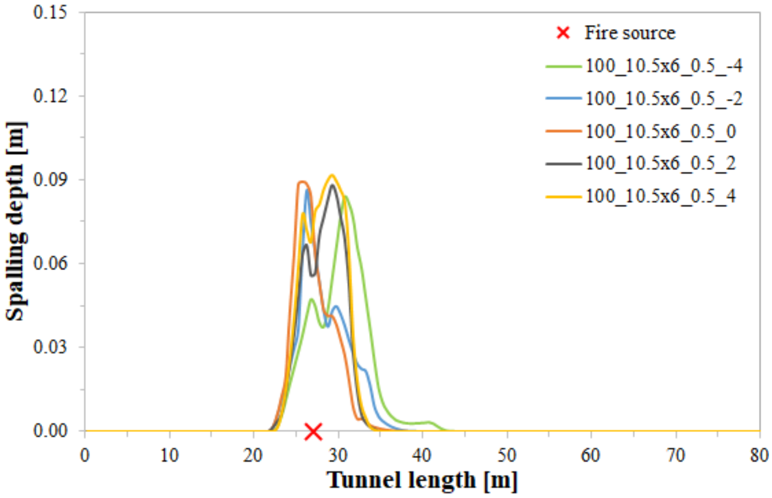

Fig. 7.9. Longitudinal section. Spalling depth profiles predicted along the right wall as a function of the longitudinal slope; v = 0.5 m/s and t = 60 min.

Nomenclature

Symbol	Unit	Description
A	m^2	Tunnel cross-section area
AADT		Annual Average Daily Traffic
c	kJ/(kgK)	Specific heat
CO		Carbon Monoxide
d	mm	Initial thickness of coatings
DNS		Direction Numerical Simulation
E	J/mol	Activation energy
FEM		Finite Element Method
FVM		Finite Volume Method
g	m/s^2	Gravity acceleration
h	m	Distance from the road pavement
H	m	Tunnel height
HC		HydroCarbon fire curve
HGV		Heavy Good Vehicle
HSC		High Strength Concrete
HRR	MW	Heat Release Rate
HRRPUA	MW/m^2	Heat Release Rate per Unit Area
LES		Large Eddy Simulation
ln		Natural logarithm
LPG		Liquefied Petroleum Gas
NB		Negative Binomial
NRMSE		Normalized Root Mean Square Error
NSC		Normal Strength Concrete
Q	W	HRR
Q_ENTH	kW	Enthalpy flow
Q_TOT	kW	Total heat flow
PFP		Passive Fire Protection
RTE		Radiation Transport Equation
RWS		Rijkswaterstaat Curve
s	%	Longitudinal slope

v	m/s	Longitudinal ventilation
VLES		Very Large Eddy Simulation
t	min	Time
T	°C	Temperature
TGA		ThermoGravimetric Analysis
UHSC		Ultra-High Strength Concrete
w	m	Distance from the right wall
W	m	Tunnel width
X		Independet variable
Y		Dependet variable

Greek Symbol

ε		Emissivity
θ	°C	Temperature of concrete
λ	W/(mK)	Thermal conductivity
ρ	Kg/m^3	Initial density

Sup and subscripts

A_{pre}	1/s	Pre-exponential factor
c_p	J/(kgK)	Specific heat of the air
D^*	m	Characteristic length scale
δ_x	m	Nominal size grid
H_{rea}	kJ/kg	Heat of reaction
HC_{mod}		Modified HC fire curve
HRR_{max}	MW	Maximum HRR
θ_{car}	°C	Carbonization temperature
λ_i		Expected value of the i-th Y
λ_{ic}		λ_i related to the ceiling
λ_{iw}		λ_i related to the right wall
ρ_∞	kg/m^3	Air density
ρ_f	Kg/m^3	Final density
t_{max}	min	Time to reach HRR_{max}
T_A	°C	Temperature at point A
T_B	°C	Temperature at point B
T_∞	K	Ambient temperature
T_{ref}	°C	Reference temperature